

**SPATIOTEMPORAL ANALYSIS OF CARDIAC DISEASE USING  
MURINE FOUR-DIMENSIONAL ULTRASOUND**

by

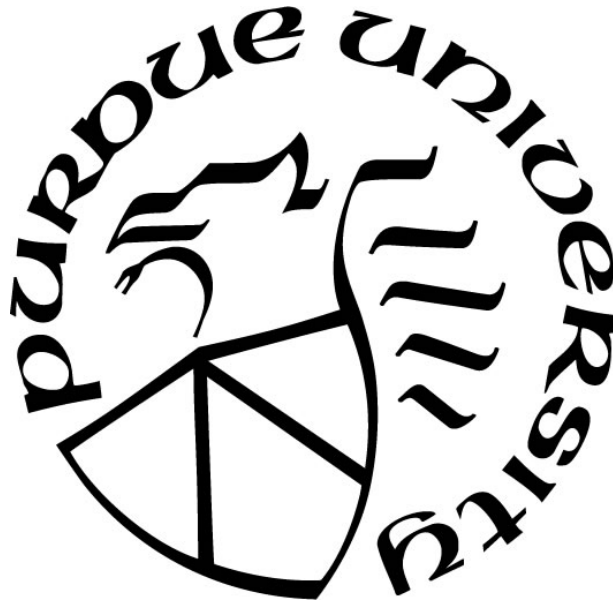
**Frederick William Damen**

**A Dissertation**

*Submitted to the Faculty of Purdue University*

*In Partial Fulfillment of the Requirements for the degree of*

**Doctor of Philosophy**



Weldon School of Biomedical Engineering

West Lafayette, Indiana

May 2021

**THE PURDUE UNIVERSITY GRADUATE SCHOOL  
STATEMENT OF COMMITTEE APPROVAL**

**Dr. Craig J. Goergen, Chair**

Weldon School of Biomedical Engineering

**Dr. Adrian Buganza Tepole**

School of Mechanical Engineering

**Dr. Jessica M. Ellis**

Department of Physiology, East Carolina University

**Dr. Joseph Rispoli**

Weldon School of Biomedical Engineering

**Approved by:**

Dr. Andrew O. Brightman

*Dedicated to my mom and dad, Hyon-Sook and Fred Damen,  
for instilling in me the importance of hard work, dedication, kindness, and humility.*

## ACKNOWLEDGMENTS

First and foremost, I would like to express my deepest gratitude to my advisor Dr. Craig J. Goergen. Over the past eight years, he has nurtured my scientific curiosity, motivated me to be both creative and practical in my research efforts, and been an ideal role model for how to be a successful scientist. I can confidently say that I could not have chosen a better mentor for my doctoral training.

I also am grateful to the other members of his lab, the CardioVascular Research Imaging Laboratory, who have not only been a source of inspiration and constructive criticism, but also friendship and constant support. They have all helped me to become a better person in their own way, and I cannot wait to see what they are all able to accomplish in the future.

I would like to extend my sincere thank you to the other members of my PhD committee and all the collaborators I have had the pleasure to work with over the years. Drs. Adrian Buganza Tepole, Jessica Ellis, and Joseph Rispoli have each provided invaluable feedback on the direction of my research, as well as guidance toward my overarching professional development. In regards to the work discussed in Chapter 3, alongside Dr. Jessica Ellis, I've greatly enjoyed working with Dr. Andrea Pereyra in studying the *Cpt2<sup>M-/-</sup>* mouse model. In regards to the work discussed in Chapter 4, Dr. Mauro Costa, Dr. Milena Furtado, Dr. Raghav Pandey, and Dorothy Ahlf Wheatcraft have all been wonderful to collaborate with in our investigation of the *Nkx2-5<sup>183P/+</sup>* mice. I also want to recognize the amazing support I've had over the years from FUJIFILM VisualSonics Inc. members Bret Hawkins, Dr. Kristiina Aasa, Stephen Buttars, Andrew Needles, Greg Nesbitt, Mandi Da Silva, Kathy Volpe, Dr. Sarah Burris, Melissa Yin, and Dr. Holly Lay.

Helping me stay grounded throughout my PhD training, I will be forever grateful for my friends and family. Drs. Arvin Soepriatna and Gurneet Sangha were not only two of the best labmates that anyone could ask for, but they've also become two of my closest friends. (Soon to be) Dr. Brett Meyers has also been an amazing friend over the years, pushing me scientifically and being a sounding board for many aspects of life. An undergraduate member of our lab, Daniel Gramling, has not only helped me become a better mentor and learn the importance of trust, but I am glad to say has also become a good friend. The culmination of this work would also not be possible without the love and support of my family; in particular my mom and dad, Hyon-Sook and Fred Damen, and my brothers, Jonathan and Nicholas, who have helped shape me into the person I am today.

Finally, I would like to extend my great appreciation my past scientific mentors, Drs. Xiaohong “Joe” Zhou, Xiaoping Hu, and Longchuan Li, for without their guidance and trust in me, I would not be where I am today. I would also like to thank my funding sources from the NIH T32 Diabetes Training Grant and F30 Fellowship for their financial support during my MD/PhD training.

## PREFACE

As of the time of submission, two chapters of this dissertation (Chapters 2 and 5) have been published in peer-reviewed journals, noted at the start of those chapters. Additionally, two chapters of this dissertation (Chapters 3 and 4) will have been submitted for publication in peer-reviewed journals, similarly noted at the start of those chapters. Minor edits to the formatting and wording have been made in these chapters to produce a cohesive piece of writing. The organization of this dissertation begins with a brief introduction on the scope of cardiomyopathies, mouse models thereof, and various imaging techniques available to study murine cardiac function (Chapter 1). We then detail the preliminary work done to validate the recently developed high-frequency four-dimensional ultrasound (4DUS) imaging technique (Chapter 2). Chapters 3 and 4 outline subsequent applications of 4DUS to two models of hypertrophic cardiomyopathy, namely *Cpt2*<sup>M/-</sup> (Chapter 3) and *Nkx2-5*<sup>183P/+</sup> (Chapter 4) for their genetic targets, as well as propose novel 4DUS analysis endpoints to better characterize cardiac function. We then describe the development and relative performance of three machine learning algorithms that can be applied to automatically predict the location of left ventricular boundaries based on 4DUS-derived images (Chapter 5). Finally, we conclude by reflecting on the scientific contribution of this dissertation and potential future directions of this work (Chapter 6). For a comprehensive list of authored journal articles and their scientific impact, please refer to PUBLICATIONS on page 122.

# TABLE OF CONTENTS

|                                                                   |    |
|-------------------------------------------------------------------|----|
| TABLE OF CONTENTS.....                                            | 7  |
| LIST OF TABLES.....                                               | 10 |
| LIST OF FIGURES .....                                             | 11 |
| ABBREVIATIONS .....                                               | 17 |
| ABSTRACT.....                                                     | 18 |
| INTRODUCTION .....                                                | 19 |
| 1. BACKGROUND.....                                                | 21 |
| 1.1 Mechanisms and Animal Models.....                             | 22 |
| 1.1.1 Dilated Cardiomyopathy .....                                | 22 |
| 1.1.2 Hypertrophic Cardiomyopathy.....                            | 23 |
| 1.1.3 Ischemic Cardiomyopathy.....                                | 26 |
| 1.2 <i>In Vivo</i> Assessment of Myocardial Kinematics.....       | 28 |
| 1.2.1 Conventional Imaging Techniques.....                        | 28 |
| 1.2.2 Direct MRI Measurement of Myocardial Kinematics.....        | 29 |
| 1.2.3 High-Frequency Ultrasound.....                              | 31 |
| 2. PRELIMINARY 4DUS VALIDATION .....                              | 33 |
| 2.1 Abstract.....                                                 | 33 |
| 2.2 Introduction .....                                            | 33 |
| 2.3 Methodology.....                                              | 35 |
| 2.3.1 Murine Models .....                                         | 35 |
| 2.3.2 Magnetic Resonance Imaging (MRI).....                       | 36 |
| 2.3.3 High-Frequency Ultrasound: 4DUS and Short-Axis M-Mode ..... | 36 |
| 2.3.4 Anesthesia and Physiological Monitoring.....                | 37 |
| 2.3.5 Cardiac Function Assessment .....                           | 39 |
| 2.3.6 Histology .....                                             | 40 |
| 2.3.7 Statistical Analysis .....                                  | 40 |
| 2.4 Results .....                                                 | 41 |
| 2.5 Discussion and Conclusion.....                                | 45 |

|                                                                                                                         |    |
|-------------------------------------------------------------------------------------------------------------------------|----|
| 3. REGIONAL KINEMATIC ANALYSIS OF DISEASE PROGRESSION IN CPT2 <sup>M/-</sup> MODEL OF HYPERTROPHIC CARDIOMYOPATHY ..... | 47 |
| 3.1 Abstract.....                                                                                                       | 47 |
| 3.2 New & Noteworthy .....                                                                                              | 48 |
| 3.3 Introduction .....                                                                                                  | 48 |
| 3.4 Methods .....                                                                                                       | 49 |
| 3.4.1 Animal Models and Study Timeline. ....                                                                            | 49 |
| 3.4.2 Ultrasound Imaging.....                                                                                           | 50 |
| 3.4.3 Boundary Definition and Kinematics Analysis.....                                                                  | 51 |
| 3.4.4 Derivation of Regional Cardiac Strain. ....                                                                       | 52 |
| 3.4.5 Hybrid Strain Index.....                                                                                          | 53 |
| 3.4.6 Longitudinal Metric Analysis.....                                                                                 | 54 |
| 3.4.7 Receiver Operating Characteristic Analysis .....                                                                  | 54 |
| 3.4.8 Statistics .....                                                                                                  | 54 |
| 3.5 Results .....                                                                                                       | 55 |
| 3.5.1 Global Function and LV Morphometry .....                                                                          | 55 |
| 3.5.2 Regional Circumferential Strain.....                                                                              | 58 |
| 3.5.3 Regional Longitudinal Strain .....                                                                                | 60 |
| 3.5.4 Hybrid Strain Index.....                                                                                          | 62 |
| 3.6 Discussion.....                                                                                                     | 64 |
| 3.6.1 Limitations .....                                                                                                 | 66 |
| 3.7 Conclusion.....                                                                                                     | 66 |
| 4. SPATIOTEMPORAL STRAIN MAPS OF DISEASE PROGRESSION IN NKX2-5 MODEL OF HYPERTROPHIC CARDIOMYOPATHY .....               | 67 |
| 4.1 Introduction .....                                                                                                  | 67 |
| 4.2 Methods .....                                                                                                       | 68 |
| 4.2.1 Animal Models.....                                                                                                | 68 |
| 4.2.2 Ultrasound Acquisition .....                                                                                      | 69 |
| 4.2.3 Boundary Definition and Kinematics Analysis.....                                                                  | 69 |
| 4.2.4 Spatiotemporal Strain Mapping .....                                                                               | 71 |
| 4.2.5 Cross-Sectional and Longitudinal Assessments.....                                                                 | 72 |

|         |                                                                 |     |
|---------|-----------------------------------------------------------------|-----|
| 4.2.6   | Statistics .....                                                | 73  |
| 4.3     | Results and Discussion .....                                    | 74  |
| 4.3.1   | Global Function and Regional Strain .....                       | 74  |
| 4.3.2   | Spatiotemporal Strain Mapping .....                             | 76  |
| 4.4     | Conclusions .....                                               | 78  |
| 5.      | MACHINE LEARNING APPLICATIONS TO 4DUS KINEMATICS ANALYSIS ..... | 79  |
| 5.1     | Abstract.....                                                   | 79  |
| 5.2     | Introduction .....                                              | 80  |
| 5.3     | Materials and Methods .....                                     | 81  |
| 5.3.1   | Ultrasound Data.....                                            | 81  |
| 5.3.2   | 4DUS Analysis and Contour Structure .....                       | 82  |
| 5.3.3   | Machine Learning Algorithms .....                               | 83  |
| 5.3.3.1 | Prediction Objective .....                                      | 83  |
| 5.3.3.2 | Modeling Approach .....                                         | 84  |
| 5.3.3.3 | Model Variants .....                                            | 84  |
| 5.3.4   | Measuring Model Performance.....                                | 85  |
| 5.3.5   | Description of Metrics Derived from LV Mesh.....                | 85  |
| 5.4     | Results and Discussion .....                                    | 86  |
| 5.4.1   | Model Fitting Results .....                                     | 86  |
| 5.4.2   | Performance of Predication-Based Metrics.....                   | 89  |
| 5.4.3   | Limitations .....                                               | 90  |
| 5.4.4   | Future Applications .....                                       | 91  |
| 5.5     | Conclusions .....                                               | 92  |
| 6.      | CONTRIBUTIONS TO SCIENTIFIC KNOWLEDGE.....                      | 94  |
| 6.1     | Overview and Impact of Research Findings .....                  | 94  |
| 6.2     | Directions for Future Research.....                             | 95  |
|         | APPENDIX A. SUPPLEMENTAL DATA TO CHAPTER 3 .....                | 97  |
|         | APPENDIX B. SUPPLEMENTAL DATA TO CHAPTER 4 .....                | 100 |
|         | APPENDIX C. SUPPLEMENTAL DATA TO CHAPTER 5 .....                | 103 |
|         | REFERENCES .....                                                | 104 |
|         | PUBLICATIONS.....                                               | 122 |

## LIST OF TABLES

Table 1. Average values for all measured and calculated metrics for (A) wild-type and (B) *Cpt2<sup>M-/-</sup>* cohorts. Two-way ANOVA analysis with Tukey post-hoc comparisons were performed on the shown data. Significant within-group differences are designated with \* for SAX MM versus MRI values and + for SAX MM versus 4DUS values, as well as one, two, or three symbols for significance levels of  $p < 0.05$ ,  $p < 0.01$ , and  $p = 0.001$ , respectively. No significant differences were found between the 4DUS and MRI values for any metrics. .... 42

Table 2. Measurements of metric trends through aging. For each cohort, medians [interquartile ranges] are provided for control and *Cpt2<sup>M-/-</sup>* mice, along with p-values from Mann-Whitney tests, ratio of interquartile ranges (IQR) in *Cpt2<sup>M-/-</sup>* and control trends, area under curve (AUC) values, and the 95% confidence interval (CI) intersection locations. Metrics where 95% confidence intervals overlapped for the entire age range of the study were noted with “---”, and metrics where 95% confidence intervals did not overlap are noted with “DNO”..... 56

Table 3. Numerical comparison of model performance for both endocardial and epicardial boundaries. With each model, mean test-set MSE with associated standard deviations and  $R^2$  values are displayed. Additionally, the percentage of significant t-tests when the given row’s model’s test set MSE is smaller than that of the model indicated in the column is also provided. .... 87

Supplemental Table 1. Measurements of strain rate trends through aging. For each cohort, medians [interquartile ranges] are provided for control and *Cpt2<sup>M-/-</sup>* mice, along with p-values from Mann-Whitney tests, ratio of interquartile ranges (IQR) in *Cpt2<sup>M-/-</sup>* and control trends, area under curve (AUC) values, and the 95% confidence interval (CI) intersection locations. Metrics where 95% confidence intervals overlapped for the entire age range of the study were noted with “---”, and metrics where 95% confidence intervals did not overlap are noted with “DNO”..... 97

Supplemental Table 2. Global and regional cardiac function metrics derived from wild-type and *Nkx2-5<sup>183P/+</sup>* 4DUS data, compared at 8, 12, and 16 weeks old. Summary values for each cohort and imaging time-point are shown as mean (standard deviation). Comparisons were performed using a two-way repeated measures ANOVA with post-hoc Bonferroni's multiple comparisons test;  $p < 0.05$  was considered statistically significant and corresponding values were highlighted in red. For each region from which either circumferential or longitudinal strain information was analyzed, peak strain, systolic strain rate, early-diastolic strain rate, and late-diastolic strain rate was reported. .... 100

Supplemental Table 3. Results of serial paired t-tests with Bonferroni-Dunn’s multiple comparisons corrections on metrics derived using each of the three proposed machine learning models, compared to ground-truth values..... 103

## LIST OF FIGURES

|                                                                                                                                                                                                                                                                                                                                                                                                                                                                                                                                                                                                                                                                                                                                                                                                                                                                                                                                                                                                                                                                                                                                                                                                                                                                                                                 |    |
|-----------------------------------------------------------------------------------------------------------------------------------------------------------------------------------------------------------------------------------------------------------------------------------------------------------------------------------------------------------------------------------------------------------------------------------------------------------------------------------------------------------------------------------------------------------------------------------------------------------------------------------------------------------------------------------------------------------------------------------------------------------------------------------------------------------------------------------------------------------------------------------------------------------------------------------------------------------------------------------------------------------------------------------------------------------------------------------------------------------------------------------------------------------------------------------------------------------------------------------------------------------------------------------------------------------------|----|
| Figure 1. Recent clinical characterizations of primary cardiomyopathies. Highlighted in red and shown visually on the right are the three forms to be reviewed. Although ischemic cardiomyopathies are not included in the most recent clinical definitions, it has been included in the past and will be discussed in this review. Adapted from Maron et al. [31], Wilde et al. [35], and Thygesen et al. [36].                                                                                                                                                                                                                                                                                                                                                                                                                                                                                                                                                                                                                                                                                                                                                                                                                                                                                                | 21 |
| Figure 2. Diagrammatic representations of the various genetic and surgical targets to induce various models of cardiomyopathy. The color of each box indicates the form of cardiomyopathy modeled (i.e. blue for DCM, red for HCM, and green for ICM). Adapted from Bezzina et al. [58] and Patten et al. [5].                                                                                                                                                                                                                                                                                                                                                                                                                                                                                                                                                                                                                                                                                                                                                                                                                                                                                                                                                                                                  | 24 |
| Figure 3. Western blot (top) in 8-week-old $Nkx^{PD/-}$ hearts demonstrate a loss in proteins involved in cellular energy handling, and suggest (bottom) a potential metabolic reprogramming.                                                                                                                                                                                                                                                                                                                                                                                                                                                                                                                                                                                                                                                                                                                                                                                                                                                                                                                                                                                                                                                                                                                   | 26 |
| Figure 4. Representative steps in the myocardial infarction surgery performed in our lab. The duration by which the left coronary artery is occluded differentiates the two models we will employ for this proposed research.                                                                                                                                                                                                                                                                                                                                                                                                                                                                                                                                                                                                                                                                                                                                                                                                                                                                                                                                                                                                                                                                                   | 27 |
| Figure 5. Representative images of three MR strain quantification techniques: (A) tagging, (B) DENSE, and (C) TPM. Corresponding pulse sequences, magnitude images at peak-systole, and peak-systolic displacement (tagging and dense) and velocity (TPM) maps are shown in line together. Figure adapted from Hankiewicz et al. [121], Gilson et al. [123], and Herold et al. [124].                                                                                                                                                                                                                                                                                                                                                                                                                                                                                                                                                                                                                                                                                                                                                                                                                                                                                                                           | 30 |
| Figure 6. Representative displays of the imaging modalities used on a representative mouse: (top) short-axis MM (SAX MM), (mid) 4D ultrasound (4DUS), and (bottom) bright-blood gradient echo MRI. The SAX MM row shows the prescribed cursor for sampling (dashed yellow line) along with corresponding M-Mode data time-synced to ECG signals. The 4DUS and MRI rows both show long-axis (left), short-axis (center), and four-chamber (right) views at corresponding slice locations.                                                                                                                                                                                                                                                                                                                                                                                                                                                                                                                                                                                                                                                                                                                                                                                                                        | 35 |
| Figure 7. Overview of masking and slice analysis. Example (A) short-axis 4DUS slice with outlines of endocardial (blue) and epicardial (green) borders drawn. Adjacent short-axis border definitions are pieced together to create a volumetric mask, as shown in (B) with an example mask (blue) of the left ventricle in a long-axis view. The epicardial border (green) was included in (B) as well for reference. In order to identify the sensitivity of total mask volume to interpolated borders across skipped slices, (C; top) a complete masking (i.e. every slice across the volume was manually outlined) had equally sized subsets of slices deleted, (C; middle/bottom) which were subsequently filled using cubic spline interpolation. A slice thickness of 0.0762 mm was used to calculate physical gap sizes. At each gap size, the set of remaining slices – excluding the most proximal and distal slices – were serially shifted to identify variability based on gap positioning. Total volumes were calculated for each paradigm as the sum of all cross-sectional areas. Percent differences in volume from the complete masking across all gap paradigms are shown for a representative (D; left) wild-type, (D; middle) early stage disease, and (D; right) late stage disease mouse. | 38 |

Figure 8. Scatter dot plots with mean and standard deviation bars comparing measurement differences between each pair of imaging methods. In each plot, the left blue column represents the 4DUS - MRI values, the green center column represents the SAX MM - 4DUS values, and the red right column represents the SAX MM - MRI values. The plots of (A) ejection fraction, (B) stroke volume, and (C) left ventricle mass each represent metrics derived from volume estimates made at (D) end-diastole and (E) peak-systole, commonly used to evaluate left ventricular function. One-way ANOVA analysis identified statistical significance between methods as designated by \* ( $p < 0.05$ ) and \*\* ( $p < 0.01$ ) respectively..... 43

Figure 9. Representative Masson’s Trichrome histology of the various disease stages imaged, with magnifications at (A) 4x (scale bar = 1.0mm), (B) 10x (scale bar = 200  $\mu$ m), and (C) 40x (scale bar = 100  $\mu$ m). The first row shows a representative non-mutated mouse (n = 5) in which wild-type cardiomyocyte size and density is observed. The second row shows an early stage of hypertrophy (n = 3) where enlarged cardiomyocytes are observed without any noticeable necrosis. The third row shows a late stage of hypertrophy (n = 2) in which enlarged cardiomyocytes and cell necrosis with less stain uptake are both observed..... 44

Figure 10. Characterization plots of the wild-type, early stage disease, and late stage disease mice derived from the 4DUS based metrics. The top three plots of EF versus SV for (A) SAX MM, (B) MRI, (C) 4DUS illustrate the relative spread of cardiac function metrics across the study animals. Distributions are more closely matched for the MRI and 4DUS techniques. This agreement in metric distributions is also observed for the structural metrics EDV versus LVM (D-F). The characteristics expected for the *Cpt2<sup>M-/-</sup>* model are highlighted in these plots showing relative clusters depending on health status..... 45

Figure 11. *Cpt2<sup>M-/-</sup>* induced hypertrophy compared to control. Representative control (top) and *Cpt2<sup>M-/-</sup>* (bottom) mouse hearts at 15 weeks of age visualized with A) three orthogonal views from four-dimensional ultrasound (4DUS) data at end-diastole, B) gross anatomical sections post-fixation, and C) H&E and Masson’s Trichrome histology from selected box regions. Ultrasound and gross section scale bar = 2mm. Histology scale bar = 100 $\mu$ m. Ultrasound image planes are designated as short-axis (SAX), long-axis (LAX), and coronal; orientation is designated with labels for the posterior (P), inferior (I), and left (L) sides of the heart. .... 50

Figure 12. Schematic for standardized 4DUS analysis procedure. The outlined steps include: A) reorientation of data to defined axes, B) tracking z-axis position (posz) of the left-ventricular base and apex across relative time (t) in the cardiac cycle, C) defining and tracking local wall motion (posZ,  $\theta$ , E) at a grid of endo- (E=0) and epi-cardial (E=x) points equally spaced across four short-axis slices (Z) and six rotations ( $\theta$ ) around the left ventricle, and D) quantification of regional kinematics from which strain metrics are calculated. Meshes in section D) are oriented such that the viewer is looking at the septal wall (top) or the free-wall (bottom), at 10% increments throughout a representative cardiac cycle. Red-axes denote the same central “z-axis” that the data is oriented to in the first step..... 52

Figure 13. Global function and morphometric quantification of hypertrophy driven dysfunction through aging. Global function and anatomy metrics derived from endo- and epi-cardial surfaces at both end-diastole and peak-systole are investigated, including A) stroke volume (SV), B) ejection fraction (EF), D) end-diastolic volume (EDV), E) left-ventricular mass (LVM), and F) wall thickness (LVWT). On each scatter plot of longitudinally collected measurements, data from control mice are shown in blue and *Cpt2<sup>M/-</sup>* mice are shown in red. Points from the same mouse are shown connected, and linear regression performed on across each cohort are visualized with thick dashed lines. To assess the earliest age in which metrics from a *Cpt2<sup>M/-</sup>* mouse might deviate from the control population, the cumulative linear regression lines with 95% confidence intervals C) for ejection fraction were plotted and the age at which the confidence intervals no-longer overlap was identified (i.e., 7.11 weeks for EF). Additionally, dot plots are shown for each metric comparing slopes derived from mouse-specific linear regression, with horizontal lines designating median and interquartile ranges. Markers above each comparison plot indicate significance levels from non-parametric Mann-Whitney tests ( $***p < 0.001$ )..... 57

Figure 14. Regional circumferential strain measurements. Schematic (A) of where across the left ventricle circumferential strain was measured, and how peak strain ( $E\theta\theta$ ), systolic strain rate ( $\Delta E\theta\theta, \text{sys.}$ ), early diastolic strain rate ( $\Delta E\theta\theta, \text{early dia.}$ ), and late diastolic strain rate ( $\Delta E\theta\theta, \text{late dia.}$ ) were defined on a representative strain curve. Longitudinally measured peak circumferential strain (B) are shown for the base, mid-ventricle (Mid-LV), and apical slices, with data from control mice shown in blue and *Cpt2<sup>M/-</sup>* mice shown in red. Points from the same mouse are shown connected, and linear regression performed on across each cohort are visualized with thick dashed lines. Comparison plots of strain trends from each mouse and region are shown (bottom), with horizontal lines designating median and interquartile ranges. Significance markers above each comparison plot indicate p-value level from non-parametric Mann-Whitney tests ( $***p < 0.001$ ;  $**p < 0.01$ ). Additionally, example plots of longitudinal measurements, and trend comparisons, are provided (C) for systolic (sys.), early diastolic (early dia.), and late diastolic (late dia.) strain rates at the base of the heart..... 59

Figure 15. Regional longitudinal strain measurements. Schematic (A) localizing the area from which the left ventricle longitudinal strain ( $ELL$ ) was measured. Peak longitudinal strain measured across time (B) are shown for rotations around the central z-axis corresponding to the posterior septum (Post. Sep.), posterior, posterior free-wall (Post. FW), anterior free-wall (Ant. FW), anterior, and anterior septum (Ant. Sep.) regions of the heart. Data from control mice shown in blue and *Cpt2<sup>M/-</sup>* mice shown in red. Points from the same mouse are shown connected, and linear regression performed on across each cohort are visualized with thick dashed lines. Comparison plots (C) of strain trends from each mouse and region are shown (bottom), with horizontal lines designating median and interquartile ranges. Significance markers above each comparison plot indicate p-value level from non-parametric Mann-Whitney tests ( $***p < 0.001$ ). ..... 61

Figure 16. Hybrid Strain Index (HSI). Scatter plot (A) of the basal peak circumferential strain ( $E\theta\theta$ ) value against posterior peak longitudinal strain ( $ELL$ ) value for each 4DUS dataset, with data from control mice shown in blue and  $Cpt2^{M-/-}$  mice shown in red, visualizes the relationship between the two components incorporated into the HSI metric. Similar to those shown for circumferential and longitudinal strain, HSI measurements across time (B) are overlaid with cumulative linear regression results as thick dashed lines, as well as a comparison plot of HSI trends for individual mice. Significance markers indicate  $p$ -value level from non-parametric Mann-Whitney tests ( $***p < 0.001$ ). Demonstrating of the use of HSI in better characterizing disease progression, a scatter plot (C) of AUC values from ROC analysis against the ratio of trend standard deviations is provided, with HSI (green) providing the maximum area-under-curve (AUC) value alongside ejection fraction (EF; orange), yet with a lower interquartile range (IQR) ratio. Other shown metrics include: left-ventricular mass (LVM), peak circumferential strain at the base (CSB), and peak longitudinal strain at the posterior wall (LSP), anterior septum (LSAS), and posterior septum (LSPS). Metric utility is further explored by plotting 95% confidence interval intersections against age-independent metric AUC values (D), demonstrating with a higher AUC and earlier intersection that HSI could also be a more sensitive diagnostic marker of disease than ejection fraction. .... 63

Figure 17. Schematic for standardized 4DUS analysis procedure. The outlined steps include: A) reorientation of data to defined axes, B) tracking z-axis position ( $posz$ ) of the left-ventricular base and apex across relative time ( $t$ ) in the cardiac cycle, C) defining and tracking local wall motion ( $posZ, \theta$ , E) at a grid of endocardial ( $E=o$ ) and epicardial ( $E=x$ ) points equally spaced across four short-axis slices ( $Z$ ) and six rotations ( $\theta$ ) around the left ventricle, and D) quantification and plotting of regional kinematics as circumferential and longitudinal spatiotemporal strain maps. Red axes denote the same central “z-axis” that the data is oriented to in the first step. .... 70

Figure 18. Visualization of pixelwise cross-sectional and aging based trend analysis, demonstrated using (A) circumferential spatiotemporal strain maps. Dotted black lines highlight both the time within the cardiac cycle ( $t$ ) and location across the left-ventricle ( $z$ ) for which data are isolated for analysis, stratified by both cohort and age. Cross-sectional analysis is performed by calculating (B) area under the curve (AUC) values from receiver operating characteristics (ROC) curves. Aging based trend analysis is performed with (C) linear regression through data from 8, 12, and 16 weeks old, displayed as percent strain per month. .... 73

Figure 19. Comparisons of global function, morphometry, and regional circumferential strain. Global function (i.e., end-diastolic volume, stroke volume, and ejection fraction) and morphometry (i.e., left-ventricular mass) measurements (A) are shown for both control (blue) and  $Nkx2-5^{183/+}$  (red) mice, with significance markers for cross-sectional comparisons. Peak circumferential strain  $E\theta\theta$  measurements (B) are shown for the base, mid-ventricle (Mid-LV), and apical slices, with comparable statistical comparison markers. Significance markers above each comparison plot indicate  $p$ -value level from two-way ANOVA with post-hoc Bonferroni's multiple comparisons test ( $**p < 0.01$ ;  $*p < 0.05$ ). Additionally, a scatter plot of peak  $E\theta\theta$  at the base versus apical regions (C) with data from weeks 8, 12, and 16 shown with increasing levels of transparency, demonstrate the shift in the base to apical region relationship throughout aging in each cohort. 75

Figure 20. Colormaps of circumferential strain profiles averaged at each time-point for both wild-type and Nkx cohorts. Plots as shown with relative short-axis slice locations on the y-axis and normalized time from R-peak through a cardiac cycle on the x-axis (bottom right diagram). For each time-point (first three columns), pixelwise z-scores are computed for the Nkx cohort against the wild-type cohort distribution; averaged z-score colormaps are then displayed above (bottom row). Additionally, using linear regression, the pixel-wise slope across time (last column) is computed for each cohort (last column), normalized to a per-month basis..... 76

Figure 21. Colormaps of regional longitudinal strain profiles averaged at each time-point for both wild-type and Nkx cohorts. Plots as shown with relative rotations around kinematic axis on the y-axis and normalized time from R-peak through a cardiac cycle on the x-axis (bottom right diagram). For each time-point (first three columns), pixelwise z-scores are computed for the Nkx cohort against the wild-type cohort distribution; averaged z-score colormaps are then displayed above (bottom row). Additionally, using linear regression, the pixel-wise slope across time (last column) is computed for each cohort (last column), normalized to a per-month basis. .... 77

Figure 22. Schematic for post-acquisition analysis on left-ventricular 4DUS data, including: (A) spatial reorientation to align with a central z-axis (i.e., inferior (-z) to superior (+z)), (B) tracking of apex and base locations, and (C) definition of boundary points on the endo- and epi-cardial boundaries (Eq. 14), excluding papillary muscles, to be tracked across the cardiac cycle. .... 83

Figure 23. Heatmap representations of median mean-squared-error (left) and associated R values (right) following 100 Monte Carlo simulations of the 6:1:1 testing paradigm, stratified by theta, b, and z. Predictions are based on models (A) 1 (i.e., individual z slices), (B) 2 (i.e., combined z slices), and (C) 3 (i.e., assisted). Specifically here, model 3 was assisted by incorporating t=0 radius values taken from the endocardial anterior mid-ventricle position (i.e., z=0.5, theta=90 deg). ... 88

Figure 24. Example predictions on a series of anterior free-wall test set data, based on the implemented 6:1:1 Monte Carlo cross-validation. Raw predictions for 17 separate mice are shown overlaid onto the ground-truth data for unassisted (model 2) predictions at both the (A) endocardial and (D) epicardial borders, as well as for the (B/E) assisted (model 3) predictions. Squared error plots at each temporal sample for the (C) endocardial and (F) epicardial positions demonstrate the potential lower errors resulting from the assisted approach. .... 89

Figure 25. Example short-axis ultrasound image at the base of the heart demonstrating the location of sternum shadow artifacts (yellow) and mitral valve attachments to the left ventricular myocardium (red). Points most commonly affected are color-coded and displayed on a corresponding long-axis schematic..... 91

Supplemental Figure 1. Measurements of systolic (sys.; left column), early diastolic (early dia.; middle column), and late diastolic (late dia.; right column) circumferential strain rates, derived from the base, mid-ventricle (Mid-LV), and apical regions of the left ventricle. Data from control mice shown in blue and Cpt2M<sup>-/-</sup> mice shown in red. Points from the same mouse are shown connected, and linear regression performed on across each cohort are visualized with thick dashed lines. Comparison plots of strain rate trends from each mouse and region are shown (bottom), with horizontal lines designating median and interquartile ranges. Significance markers above each comparison plot indicate p-value level from non-parametric Mann-Whitney tests (\*\*\*p < 0.001; \*\*p < 0.01). .... 98

Supplemental Figure 2. Measurements of systolic (sys.; left column), early diastolic (early dia.; middle column), and late diastolic (late dia.; right column) longitudinal strain rates, derived from the posterior septum (Post. Sep.), posterior (Post.), posterior free-wall (Post. FW), anterior free-wall (Ant. FW), anterior (Ant.), and anterior septum (Ant. Sep.) regions of the heart. Data from control mice shown in blue and *Cpt2<sup>M-/-</sup>* mice shown in red. Points from the same mouse are shown connected, and linear regression performed on across each cohort are visualized with thick dashed lines. Comparison plots of strain rate trends from each mouse and region are shown (bottom), with horizontal lines designating median and interquartile ranges. Significance markers above each comparison plot indicate p-value level from non-parametric Mann-Whitney tests (\*\* $p < 0.001$ ; \*\* $p < 0.01$ ; \* $p < 0.05$ )..... 99

Supplemental Figure 3. Spatiotemporal circumferential strain maps derived from each 4DUS dataset, grouped by cohort (i.e., wild-type (left column) and *Nkx2-5<sup>I83P/+</sup>* (right column)). Within each column, each row contains strain maps from the same mouse at 8, 12, and 16 weeks old, respectively. .... 101

Supplemental Figure 4. Spatiotemporal longitudinal strain maps derived from each 4DUS dataset, grouped by cohort (i.e., wild-type (left column) and *Nkx2-5<sup>I83P/+</sup>* (right column)). Within each column, each row contains strain maps from the same mouse at 8, 12, and 16 weeks old, respectively. .... 102

## ABBREVIATIONS

|        |                                             |
|--------|---------------------------------------------|
| 2D     | Two-Dimensional                             |
| 3D     | Three-Dimensional                           |
| 4D     | Four-Dimensional                            |
| 4DUS   | Four-Dimensional Ultrasound                 |
| MRI    | Magnetic Resonance Imaging                  |
| AHA    | American Heart Association                  |
| SAX-MM | Short-Axis Motion-Mode                      |
| FLASH  | Fast Low-Angle Shot                         |
| CPT2   | Carnitine Palmitoyltransferase 2            |
| LV     | Left Ventricle                              |
| EDV    | End-Diastolic Volume                        |
| PSV    | Peak-Systolic Volume                        |
| SV     | Stroke Volume                               |
| EF     | Ejection Fraction                           |
| LVM    | Left Ventricular Mass                       |
| LVWT   | Left Ventricular Wall Thickness             |
| DCM    | Dilated Cardiomyopathy                      |
| ICM    | Ischemic Cardiomyopathy                     |
| HCM    | Hypertrophic Cardiomyopathy                 |
| MI     | Myocardial Infarction                       |
| CAD    | Coronary Artery Disease                     |
| TAC    | Transverse Aortic Constriction              |
| LCA    | Left Coronary Artery                        |
| DENSE  | Displacement ENcoding with Simulated Echoes |
| TPM    | Tissue Phase Mapping                        |
| UTE    | Ultra-short TE                              |

## ABSTRACT

Cardiac disease remains the number one cause of all mortality in the United States, prompting a continued effort to understand the various factors that exacerbate heart disease. To this end, murine models of cardiac disease have served a crucial role by allowing researchers to systematically manipulate disease-linked factors and longitudinally track changes in cardiovascular function. Routine assessment of heart function in these mice is often conducted using high-frequency ultrasound; however, cardiac function metrics drawn from conventional ultrasound imaging heavily relies on measurements obtained from a representative slice of the heart and idealized geometries of the left ventricle. While high-field cine-MRI can circumvent these limitations with volumetric imaging, our group has recently developed and validated a high frequency four-dimensional ultrasound (4DUS) technique that provides higher spatiotemporal resolution, comparable accuracy in cardiac metrics, and relatively faster acquisitions compared to cine-MRI. We have also developed standardized analysis methods for left-ventricular 4DUS data, encapsulated in a custom interactive software toolbox. Our software helps users measure regionally-specific myocardial kinematics, interpolates a four-dimensional mesh of the endo- and epi-cardial boundaries, and then quantifies various myocardial strain metrics. We have applied these tools to study disease progression in two murine models of pathological cardiac hypertrophy (i.e. *Cpt2*<sup>M-/-</sup> and *Nkx2-5*<sup>183P/+</sup>). Backed by our demonstrated findings, we aim to provide researchers studying cardiac disease a more comprehensive approach to characterizing their chosen models, and increase the scientific reach of cardiovascular research at large.

## INTRODUCTION

The heart is arguably one of the most critical organs of the human body as it drives the distribution of nutrients, signaling factors, and heat throughout the entire body. Any form of cardiac dysfunction can thus compromise an individual's quality-of-life; severe cases leading to organ failure and death. According to the 2021 American Heart Association (AHA) annual report, heart disease remains the number one cause of death in the United States [1]. Projections estimate a 46% increase in incidence (i.e. more than 8 million individuals 18+ years old) and a 127% increase in total heart failure costs (i.e. to \$69.7 billion) by 2030 [2], highlighting both physical and fiscal needs for improved treatment. Epidemiologic studies into the underlying causes of heart failure have revealed a vast array of contributing factors, from both physiological (e.g., genetics, diabetes, metabolic syndrome, high blood pressure) and lifestyle (e.g., smoking, poor nutrition, physical inactivity) origins [1]. These identified risk factors have helped healthcare professionals and researchers alike target their therapies, with the unified goal of improving patients' quality-of-life. Reducing the overall prevalence of heart failure should in turn reduce the associated fiscal burden on our healthcare system. While some preventative measures such as strict dieting, anti-hypertensive medications, and statins have demonstrated widespread success, there remains a gap in proper solutions outside transplantation for patients with genetic factors or irreversible damage (i.e. myocardial infarction) leading to heart failure [3, 4]. To bridge this knowledge gap, murine models provide a framework to systematically study how these genetic factors and irreversible damage can exacerbate disease phenotypes [5-9].

Complementary to the use of murine models as a foundation for developing cardiac disease therapies, *in vivo* imaging technology has proven crucial to disease diagnosis, monitoring of disease progression, and evaluation of treatment efficacy. Echocardiography in particular has proven its value in the clinic for assessing cardiac function, routinely used after any sign of cardiac distress for initial assessment and subsequent follow-ups [10, 11]. It seems natural then that ultrasound technology has been adapted for studying preclinical models of cardiac disease, utilizing novel probe designs that produce high-frequency ultrasound waves (~40MHz vs ~6MHz for adult humans) [12]. Similar to clinical echo, global metrics such as left-ventricle (LV) ejection fraction (EF), stroke volume (SV), end-diastolic volume (EDV), and LV mass (LVM) have so far been the standard in literature for reporting murine cardiac function [13-15]. Nevertheless, it must

be considered that these measurements suffer from the same limitations as clinical echo; they rely heavily on the use of idealized LV geometries, as ultrasound is traditionally a planar modality [16-18]. While recent advancements in multi-array transducers for clinical ultrasound have overcome this limitation, employing simultaneous acquisition of three-dimensional information under the probe head [19-22], this hardware has yet to be adapted for researchers studying cardiac disease in small animal models. Outside of ultrasound technology, high-field cine-MRI is capable of providing this volumetric information – often considered the gold-standard in these regards – yet still has notable limitations in system expense and acquisition duration [23-28].

Aiming to fill this gap in preclinical ultrasound, we have developed a technique to collect four-dimensional ultrasound (4DUS) data, using the same linear-probe hardware currently available to preclinical researchers. Preliminary validation work focused on global metrics of cardiac function (i.e. EF, SV, etc.) has demonstrated that 4DUS can provide higher spatiotemporal resolution, comparable accuracy in cardiac metrics, and relatively faster acquisitions compared to cine-MRI [29, 30]. Motivated by these preliminary findings, we further worked to establish a standalone analysis software from which left-ventricular dynamics can comprehensively quantified and robustly compared across cohorts of data. The developed 4DUS tools should provide researchers studying cardiac disease a more streamlined approach to comprehensively characterize cardiac function within their chosen disease models, and subsequently increase the scientific reach of the cardiovascular research community at large.

# 1. BACKGROUND

Cardiomyopathies are a set of cardiac diseases that alter the structure and function of the musculature of the heart. These can be induced by either genetic or acquired mechanisms, or a mixture of thereof, and these mechanisms are the subject of widespread research efforts aiming to identify better therapeutic avenues [31]. The most recent clinical classifications are listed in Figure 1, alongside illustrations of the three common forms that will be the focus of this review. Dilated cardiomyopathy (DCM) is clinically characterized by a dilated left ventricle and systolic dysfunction, and is the most common form of cardiomyopathy found among children <18 years old (annual incidence 0.57 per 100,000 overall) [32, 33]. Symptoms include shortness of breath, palpitations, peripheral edema, and fatigue, which are most likely consequences of impaired systolic function [34].

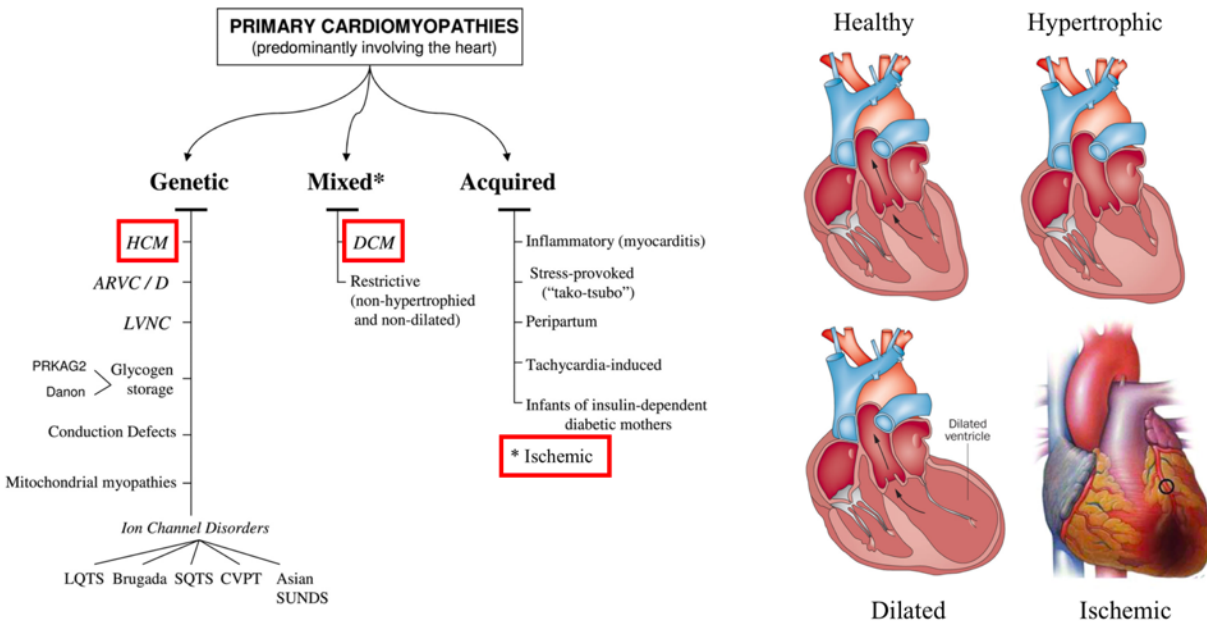


Figure 1. Recent clinical characterizations of primary cardiomyopathies. Highlighted in red and shown visually on the right are the three forms to be reviewed. Although ischemic cardiomyopathies are not included in the most recent clinical definitions, it has been included in the past and will be discussed in this review. Adapted from Maron et al. [31], Wilde et al. [35], and Thygesen et al. [36].

Hypertrophic cardiomyopathy (HCM) manifests as an enlarged left ventricular myocardium and progressive diastolic failure, and is the most common form of acquired cardiomyopathy (prevalence approximately 1 of 500 individuals) [33, 37]. While symptoms mimic that of DCM, HCM can also often progress asymptotically and has led to a phenomena of sudden cardiac death in young athletes [38]. Finally, ischemic cardiomyopathy (ICM) involves hypoxia-induced injury to the myocardium (i.e. myocardial infarction (MI)) predominantly marked by fibrotic remodeling, diminished contractile function at the ischemic site, and progressive chamber dilation. Symptoms commonly include angina, shortness of breath, and fatigue, which can occur either in acute (i.e. coronary embolism) or chronic (i.e. atherosclerosis) settings [36, 39]. In fact, ICM has been the leading cause of death amongst all cardiovascular diseases, accounting for 42.1% in the 2021 AHA report [1]. Ongoing debates still exist over characterizing ICM solely under coronary artery disease (CAD) [31, 40]; however, here we will keep ICM as the overarching descriptor.

## 1.1 Mechanisms and Animal Models

### 1.1.1 Dilated Cardiomyopathy

Dilated cardiomyopathy (DCM) is defined as a complex of an enlarged left- and/or right-ventricular chamber, progressive systolic contractile failure, and often thinning of the myocardial wall [34]. Most clinical presentations of DCM are observed alongside heart failure [40], in which weakened cardiac muscles inadequately circulate enough blood to meet the body's demands [34]. Since heart failure is a late stage diagnosis, it is not always clear whether DCM is the *de novo* cause or a secondary consequence to another stress-adaption process. Acknowledging this uncertainty, DCM research using murine models have primarily focused on understanding the *de novo* mechanisms, where DCM is not preceded by another process prior to heart failure (e.g. hypertrophy or ischemia) [41].

Transgenic DCM models have identified several genes within the sarcomeric–cytoskeletal–extracellular matrix network that induce hallmarks of clinical DCM [41, 42] (Figure 2). These genes encode structural proteins integral to the backbone architecture of cardiomyocytes and ensure stability during sarcomere contraction. Here we will highlight: muscle LIM protein (MLP) [43], Cypher [44, 45], dystrophin/utrophin [46-50],  $\alpha$ -actin [51], and laminin A/C [52]. MLP and Cypher are both proteins within the z-line of cardiac sarcomeres, serving as a branch

point for actin filaments by means of  $\alpha$ -actinin links. While mutations in these anchoring proteins inherently compromise sarcomere rigidity, research suggests that the z-line unit also acts as a mechanical stretch sensor [53] and can exacerbate systolic dysfunction by initiating signaling cascades [43-45]. Dystrophin and utrophin are components of the complex that stabilizes the cardiomyocyte cytoskeleton against the extracellular matrix. The *mdx*<sup>-/-</sup> mouse line contains a nonsense mutation in the dystrophin gene and compromises the alignment of adjacent contractile units. Interestingly, in order to mimic hallmarks of clinical DCM, utrophin must also be knocked-out in these *mdx* mice [46-49]. This suggests utrophin may substitute for dystrophin in *mdx*<sup>-/-</sup> mice, a notable difference from clinical dystrophin-linked DCM. The  $\alpha$ -actin protein is a primary building block for the actin-myosin contraction complex. Mutations in the murine cardiac  $\alpha$ -actin gene (mActin-Tg) lead to decreased myofilament Ca<sup>2+</sup> sensitivity (i.e. weakened cardiomyocyte contractions), p53 driven cardiomyocyte apoptosis, and subsequent DCM [51]. Finally, despite not directly interacting with the force generating units of cardiomyocytes, laminin proteins stabilize the nuclear membrane and prevent nuclear-stress induction of apoptotic pathways [34]. Mice with *lmna*<sup>-/-</sup> gene deletions are subject to changes in nuclear morphology, apoptosis of cardiomyocytes, and conduction abnormalities associated with severe DCM [52]. Similar to clinical presentations of DCM, each of these models have suffered from issues of early lethality. Nevertheless, observed trends in the literature show gradual improvement in animal lifespans, potentially a consequence of recent advancements in transgenic techniques.

### 1.1.2 Hypertrophic Cardiomyopathy

In contrast to DCM and its strong association with heart failure, cardiac hypertrophy is often a non-pathogenic adaptation to cardiovascular stress such as exercise, where contractile units are temporarily recruited to meet increased cardiac demand. However, when those stressors exist for prolonged durations or cardiomyocyte adaptation is compromised, progression to hypertrophic cardiomyopathy (HCM) can occur [34]. Hypertrophy of the myocardium can either occur eccentrically (i.e. new sarcomeres added in-series) or concentrically (i.e. new sarcomeres added in-parallel), depending on volume- or pressure-overloading, respectively [54]. HCM is defined by asymmetric hypertrophy of the right- and/or left-ventricle, normal or reduced left-ventricular volume, and myocardial remodeling that often includes fibrosis [31, 40, 55]. If left untreated, HCM can gradually progress to DCM and heart failure. Research into HCM using murine models has

thus focused on systematically studying this transition to pathological hypertrophy, identifying predominant genetic factors, and developing preventative strategies [5, 56, 57].

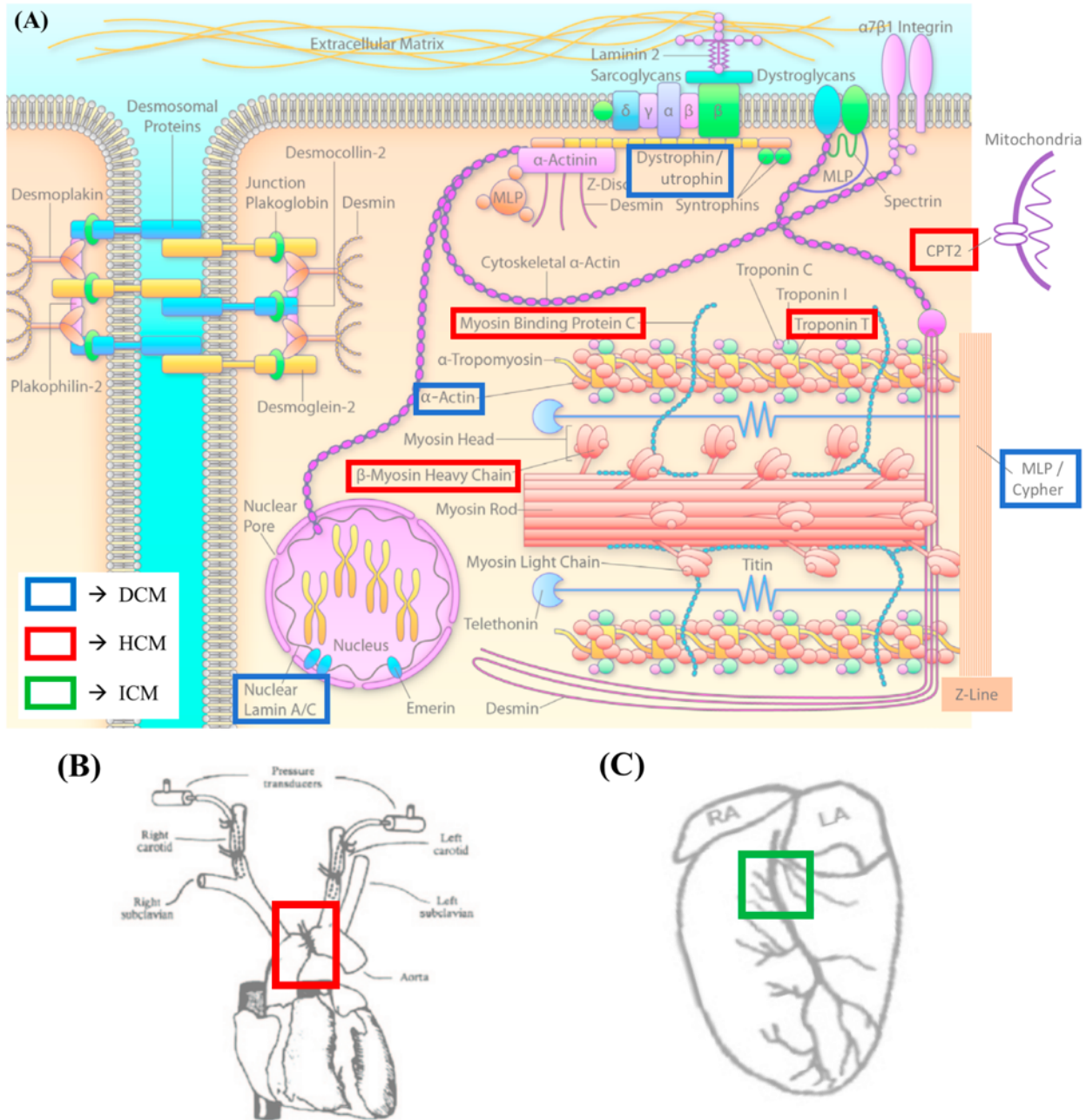


Figure 2. Diagrammatic representations of the various genetic and surgical targets to induce various models of cardiomyopathy. The color of each box indicates the form of cardiomyopathy modeled (i.e. blue for DCM, red for HCM, and green for ICM). Adapted from Bezzina et al. [58] and Patten et al. [5].

One of the most widely used techniques to induce and study cardiac hypertrophy in mice is transverse aortic constriction (TAC; Figure 2). This procedure involves surgically placing a suture around the aortic arch of an anesthetized mouse, between the innominate and left carotid arteries, to constrict the aorta and pressure-overload the left ventricle (i.e. increased afterload) [59-61]. The induced drop in cardiac function is then re-established, often within one week, by physiologic hypertrophic adaptation. As the TAC mice continue to age, the energy demands of the additional contractile units cannot be sustained and subsequent heart failure ensues [62, 63].

This procedure has been used to shed light onto several pathways involved in the remodeling process. Excessive  $\text{Ca}^{2+}$  from the sarcoplasmic reticulum [64] and deficiencies in proliferator-activated receptor (PPAR- $\gamma$ ) [65] both show to exacerbate HCM. In contrast, angiotensin II receptor inhibitors have been shown to mitigate HCM progression [66]. Still, several limitations are of note. First and foremost, TAC is a difficult and invasive procedure, requiring a skilled surgeon before acceptable survival rates are achieved. Second, hypertrophic responses to TAC seem to depend on parentage in certain wild-type strains [67, 68], potentially driven by inherent mouse-strain cardiac variability [69]. Finally, unintended complications such as internalization of the band into aortic wall can lead to further variability in the hypertrophic response [70]. While the TAC model can be a useful tool to study the progression of pressure-overload derived hypertrophy, careful attention to mouse strain and surgical technique should be employed.

Complimentary transgenic mouse studies have identified several genes that can be targeted to model inherited forms of HCM (Figure 2). In contrast to DCM, these HCM associated genes encode the sarcomere itself. Mice with heterozygous mutations of Myosin binding protein C (*mybp-c*<sup>+/-</sup>) and  $\alpha$ -myosin heavy chain ( *$\alpha$ -mhc*<sup>+/-</sup>) each demonstrate hallmarks of familial HCM [6, 71-74]. The *mybp-c*<sup>+/-</sup> and  *$\alpha$ -mhc*<sup>+/-</sup> genes encode sarcomere proteins involved in the  $\text{Ca}^{2+}$  sensitive power-stroke of cardiomyocytes, thus mutations impair contractility and promote a hypertrophic response. While both models naturally develop left-ventricular hypertrophy, interestingly only the  $\alpha$ MHC develops significantly impaired cardiac function [6]. Other sarcomere protein encoding genes have been explored such as cardiac Troponin T (cTnT) [75, 76]; however, their mild to absent hypertrophy phenotypes have further illustrated the multi-factorial nature of HCM.

Two novel murine models that genetically manipulate cellular bioenergetics to induce a HCM phenotype will be the primary focus of this thesis work. The NK2 homeobox 5 (*Nkx2-5<sup>183P/+</sup>*) model was developed by Dr. Mauro Costa and the Carnitine Palmitoyltransferase 2 (*Cpt2<sup>M-/-</sup>*) model was developed by Dr. Jessica Ellis, and both models are based on familial genetic mutations. The NKX2-5 gene is a cardiac transcription factor [77] and faithfully reproduces the hallmarks of HCM in mice [78]. Preliminary work with these mice have also revealed novel symptoms of the disease, including an early decrease in mitochondrial density and cellular respiration, compensated by increased fatty acid oxidative dependence (Figure 3). Mutations in the CPT2 gene cause a loss of an obligate enzyme in mitochondrial long-chain fatty acid oxidation [79, 80], resulting in a more severe myocardial hypertrophy and rapid progression to heart failure. These genes influence similar cellular pathways in cardiomyocytes to create energy handling defects, which then induce left-ventricular hypertrophy, chamber dilation, and progressive heart failure.

### 1.1.3 Ischemic Cardiomyopathy

Ischemic cardiomyopathies (ICM) encompass pathologies driven by compromised blood supply to the myocardium, predominantly due to acute or chronic occlusion of coronary arteries (i.e. myocardial infarction (MI)) [31]. This diminished blood supply causes focal cardiomyocyte necrosis and apoptosis distal to the occlusion, compensatory fibrosis to stabilize the dysfunctional region, and a hypertrophy response in the remaining muscle to reestablish cardiac function [34, 55]. Murine models of MI are most commonly formed through surgical intervention (Figure 2); however, select chemical and transgenic models of MI/ICM are also highlighted.

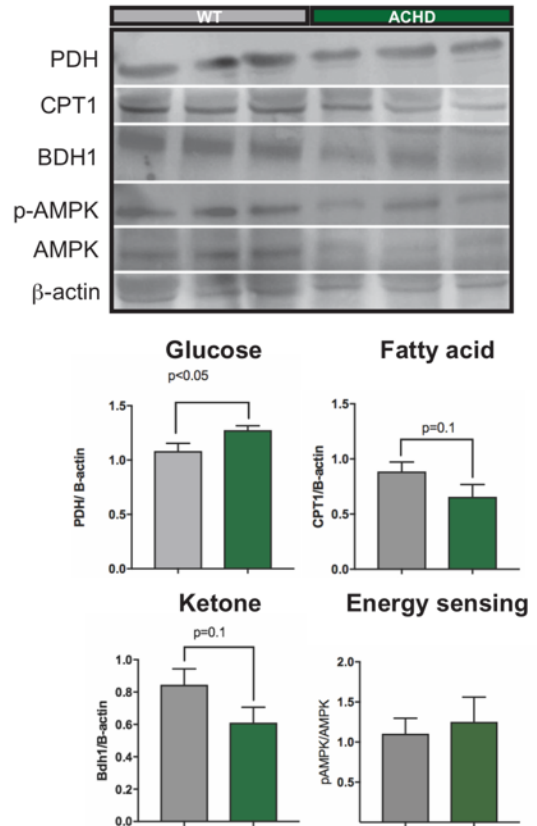


Figure 3. Western blot (top) in 8-week-old *Nkx<sup>PD/-</sup>* hearts demonstrate a loss in proteins involved in cellular energy handling, and suggest (bottom) a potential metabolic reprogramming.

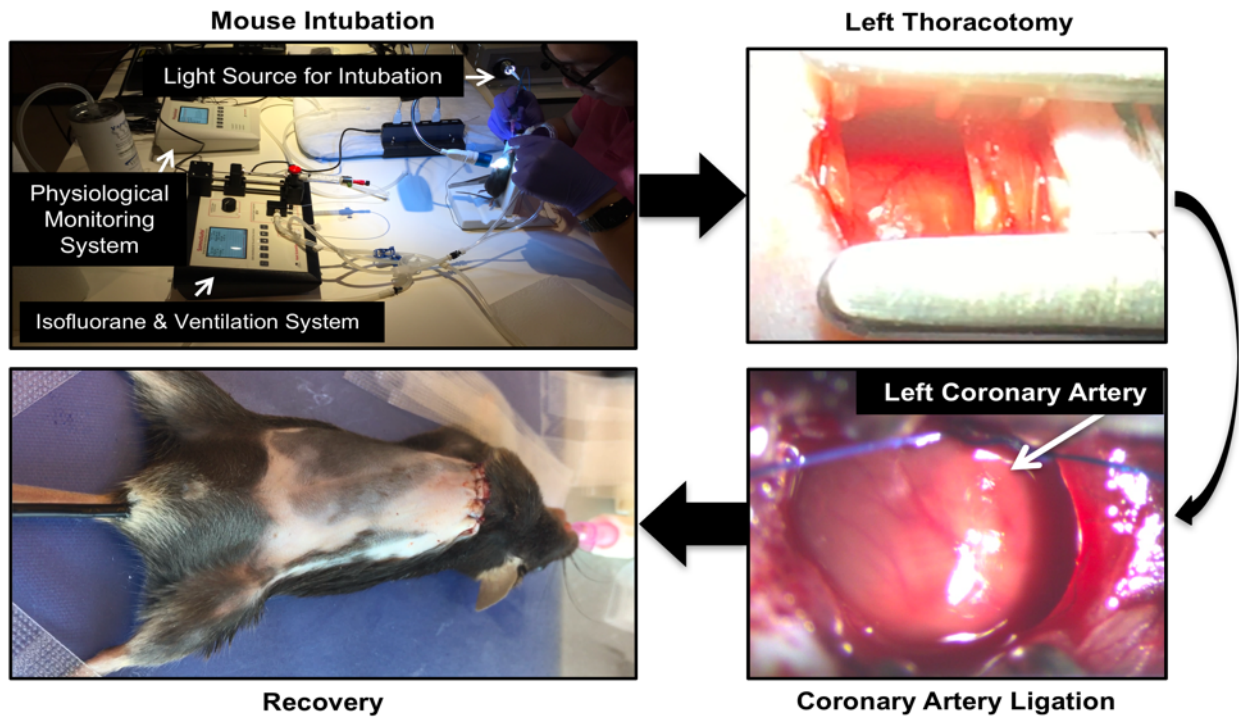


Figure 4. Representative steps in the myocardial infarction surgery performed in our lab. The duration by which the left coronary artery is occluded differentiates the two models we will employ for this proposed research.

While specifications in occlusion protocols differ between studies, the overarching procedure to induce MI in mice includes: 1) anesthesia and ventilation of the mouse, 2) thoracotomy at the 4<sup>th</sup> intercostal space, 3) identification and isolation of the left coronary artery (LCA) with a suture, 4) occlusion of the LCA, and 5) recovery of the mouse [81-83]. The aforementioned steps are illustrated in Figure 4. Occlusion methods that permanently ligate the LCA just below the left auricle serve as models of acute MI (i.e. thrombotic event), useful for studying the post-MI remodeling process/scar formation [84-86] and lethal complications (i.e. ventricular rupture) [87, 88]. In order to model more chronic forms of MI/ICM associated with coronary plaques and transient ischemia, surgical ischemia-reperfusion techniques for mice have been developed [81, 83, 89]. While responsive fibrosis and cardiac dysfunction can seemingly reverse after discontinuation of the ischemia-reperfusion protocol, these studies have also shed light onto the myocardial hibernation phenomenon. This leads to the hypothesis that cardiomyocytes may downregulate internal function as protection from transient ischemia [89]. Myocardial hibernation has thus been suggested as a potential therapeutic avenue for ICM by

“preconditioning” the myocardium [90, 91]. Additional promising therapies include targeted inhibition of the cytokine producing NF- $\kappa$ B pathway, which is notable as drugs that target this pathway already exist clinically for other applications [92, 93].

Complimentary to these popular surgical models of murine ICM, chemically injured and genetically modified models also exist. ICM induced by drug cardiotoxicity is of particular interest to pharmaceutical companies as irreversible damage to cardiomyocytes is a life-threatening side effect. Notable cardiotoxic drugs include isoproterenol [94, 95] and doxorubicin [96, 97]. Tissues surrounding coronary capillaries are susceptible to oxidative stress from these drugs, mimicking hallmarks of ischemia; however, their cardiotoxicity based mechanism makes them suboptimal models of ICM. Furthermore, recent transgenic models using mice deficient in both HDL receptor scavenger receptor class B type I (SR-BI) and apoE have shown to develop small diffuse MIs following diet-accelerated atherogenesis [98-100]. This atherogenesis involvement suggests that it may more closely reflect clinical forms of ICM [34]; however, the model still requires refinement to prevent relatively rapid death following induction, critical for researchers to study the post-MI remodeling process.

## **1.2 *In Vivo* Assessment of Myocardial Kinematics**

### **1.2.1 Conventional Imaging Techniques**

Addressing the needs of patients suffering from the aforementioned cardiomyopathies, the development and use of *in vivo* imaging has been crucial to monitoring disease progression. For example, echocardiography is often recommended as a preliminary workup for any sign of cardiac distress [10, 11, 101]. While the general imaging principles do not drastically shift from humans to animals, small animal models (e.g. rabbits, rats, mice, etc.) give researchers a greater level of control over the underlying pathophysiology and experimental factors [5], as discussed above. This allows imaging-derived biomarkers to be validated against disease phenotypes prior to clinical adaptation, which in turn could raise confidence in their clinical utility.

Three primary options for preclinical include micro-computed tomography (micro-CT), high-field magnetic resonance imaging (MRI), and high-frequency ultrasound (US). Micro-CT can rapidly acquire three-dimensional data of internal structures, with contrast derived from the relative density of adjacent tissues. Unfortunately, CT has limited utility for *in-vivo* murine cardiac

studies as its use of ionizing radiation can be harmful with routine exposure, adding unintentional confounding factors to these studies. Furthermore, the need for contrast agents to enhance heart morphology can be costly with larger cohorts [102-104]. High-field MRI can provide both dynamic and compositional information of the heart without the need for ionizing radiation or contrast agents. MRI produces image contrast by exploiting the magnetic properties of hydrogen protons, found abundantly in water molecules throughout the body. Cine-MRI protocols in particular exploit simultaneously acquired cardiac and respiratory signals to retrospectively construct image loops synchronized to one representative cardiac cycle [105, 106]. Cine-loops are then used acquired in spatial parallel to provide volumetric information across the heart. Researchers have then used these cine MRI data to extract ventricular geometries and quantify global function changes *in vivo* for select models of DCM [107, 108], HCM [24, 70], and MI/ICM [109-111]. Simultaneous addition of dobutamine, a  $\beta_1$ -receptor agonist, can simulate exercise-induced stress in diseased mice and help to also measure systolic reserve function [112-114]. Nevertheless, while cine-MRI is a versatile tool and commonly considered the gold-standard technique for preclinical cardiac imaging, the relatively higher costs and longer acquisitions are practical obstacles to its more widespread usage in this field.

### **1.2.2 Direct MRI Measurement of Myocardial Kinematics**

While high-field MRI techniques will not be the focus of this thesis, notable advancements in this field have been made that can directly estimate ventricular deformations and quantify intramyocardial kinematics. One of the initial iterations used spatially distributed pre-saturation pulses to embed a signal-nulled grid onto the end-diastolic frame of cine data, which can be algorithmically tracked through the cardiac cycle [115-118]. Several studies have applied these “tagging” methods to murine DCM models and demonstrated reductions in strain localized to the thinned regions of the myocardium [47, 119, 120]. A study by Hankiewicz, et al. systematically tracked strain changes over several months and suggested that reductions in strain may even precede wall thinning [121]. More recent work looking to both streamline the analysis and improve the reliability of findings from these types of images have applied methods such as non-linear image registration [117] and machine learning [122] with notable success.

Nevertheless, any conclusions drawn using tagging should also address the technique limitations. Tagging methods currently necessitate prospective gating in order to ensure placement

of the un-deformed grid at end-diastole, reintroducing potential issues inherent to prospective-gating (discussed above). Furthermore, as grid spacing must allow the underlying signal to be adequately captured, only regional deformations can be measured rather than displacement of individual voxels. Finally, most literature on tagging methods so far have imaged planar deformations, a suboptimal representation of physiological dynamics. This has though been addressed in recent studies that have demonstrated success in volumetric tagging and measurement of 3D cardiac strain in mice [47].

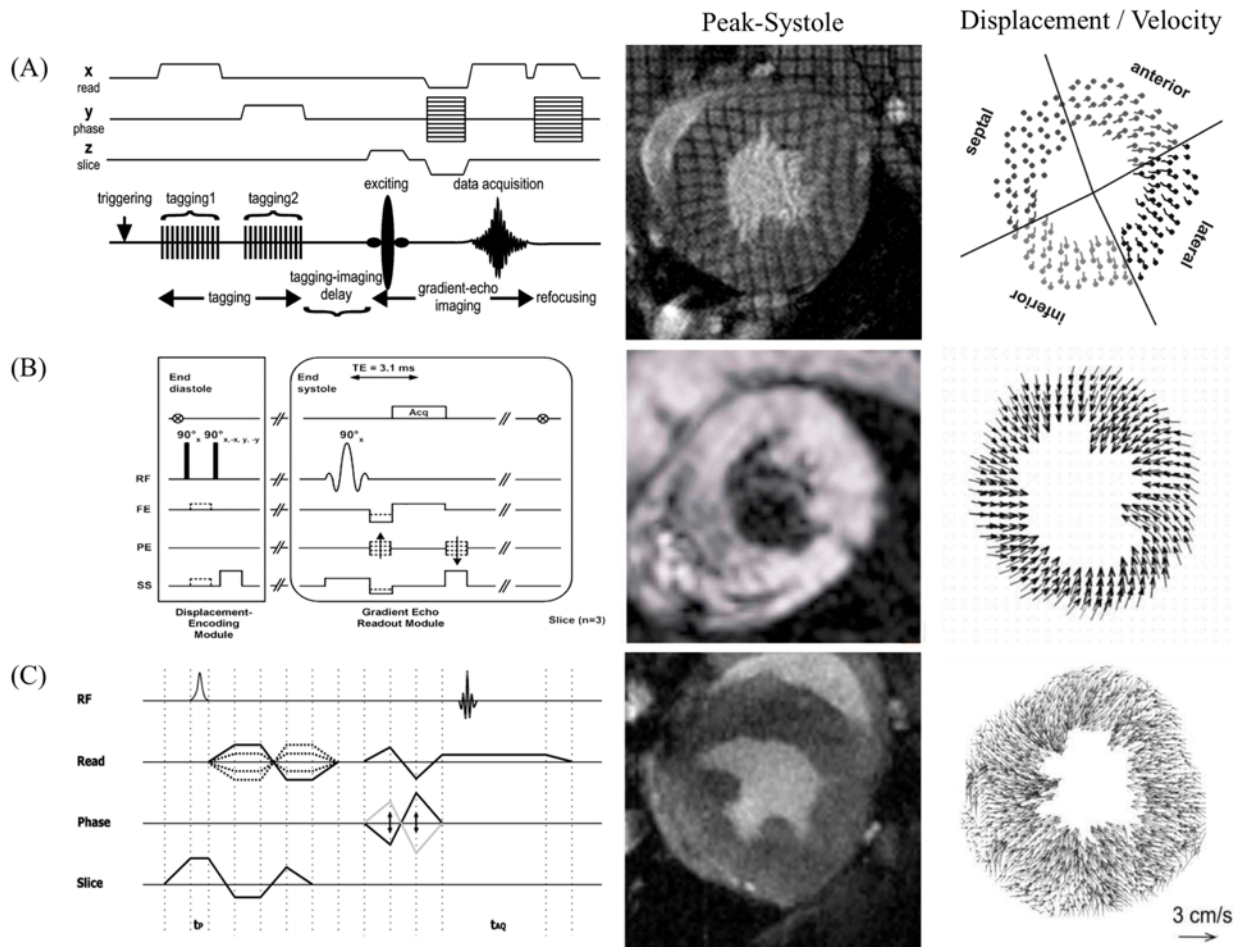


Figure 5. Representative images of three MR strain quantification techniques: (A) tagging, (B) DENSE, and (C) TPM. Corresponding pulse sequences, magnitude images at peak-systole, and peak-systolic displacement (tagging and dense) and velocity (TPM) maps are shown in line together. Figure adapted from Hankiewicz et al. [121], Gilson et al. [123], and Herold et al. [124].

With the same aim of providing strain measurements *in vivo*, two more recent techniques have focused on signal phase information, in contrast to signal magnitude used in tagging. The first technique, Displacement ENcoding with Simulated Echoes (DENSE), uses a series of two 90° preparation pulses separated by a spatial encoding gradient to set a known phase distribution that can be subsequently reassessed when the k-space signal is acquired [125]. Under this paradigm, displacements can be measured at each voxel. Furthermore, strain values have been validated in mice against echocardiography [126] and tagging [123] methods. While limited literature exists with applications to murine models of cardiomyopathy [127], recent studies have at least demonstrated capabilities comparable to tagging methods with measuring strain in three-dimensions [128, 129] and at multiple stages of the cardiac cycle [130].

The second method Tissue Phase Mapping (TPM) employs bi-polar velocity-encoding gradients in the phase-encoding direction, just prior to the echo readout, allowing velocity information to be mapped at a voxel-wise resolution [124, 131-133]. Velocity information is captured as the bi-polar gradients essentially null the phase of stationary tissues leaving dynamic tissue with a phase accumulation, and thus strain can be calculated through integration [127, 134]. While TPM still requires further development due to signal-to-noise limitations, we believe if some promising research into 4D ultra-short TE (UTE) phase-contrast imaging is adapted for TPM applications [135], TPM could eventually provide the best spatiotemporal resolution of the three presented.

### **1.2.3 High-Frequency Ultrasound**

High-frequency ultrasound is a commonly employed alternative to micro-CT and high-field MRI, which both avoids ionizing radiation and is more cost-effective. It is particularly useful for routine cardiac imaging due to its relatively high spatial-temporal resolution, portability, and ease-of-use [12]. Still, its inherent nature as a planar imaging technique necessitates geometric assumptions of heart morphology to estimate cardiac function metrics. This can be particularly problematic when studying models such as ICM where dysfunction is localized and asymmetric. Furthermore, as ultrasound contrast is based on acoustic impedance, the amount of compositional information probed from myocardial tissue is limited. Recent developments in photoacoustic ultrasound are working to provide such non-invasive compositional information, yet applications in the mouse heart have not been demonstrated and is typically limited to imaging hemoglobin otherwise [136].

In order to match the volumetric imaging capabilities of cine-MRI and expand the capabilities of high-frequency ultrasound technology, recent developments in our own lab have introduced a four-dimensional ultrasound (4DUS) technique that directly addresses these needs [29, 30, 137]. A more detailed introduction to this technology is provided in *Preliminary 4DUS Validation*.

## 2. PRELIMINARY 4DUS VALIDATION

In this section, we showcase the validation work done regarding our 4DUS technology. This study served as the motivational foundation for the subsequent research outlined in this document. We detail here the design and results of our study that compared 4DUS-based measurements of global left-ventricular function (i.e. ejection fraction, stroke volume, etc.) to short-axis M-mode and cine MRI data, assessed on the same cohort of mice [29]. The content presented in this chapter was adapted from the work published in *Tomography* entitled “High-Frequency 4-Dimensional Ultrasound (4DUS): A Reliable Method for Assessing Murine Cardiac Function”; made available under a Creative Commons Attribution License through the following link: <http://dx.doi.org/10.18383/j.tom.2017.00016>.

### 2.1 Abstract

In vivo imaging has provided a unique framework for studying pathological progression in various mouse models of cardiac disease. While conventional short-axis motion-mode (SAX MM) ultrasound and cine MRI are two of the most prevalent strategies to quantify cardiac function, they have notable limitations including imprecision, inaccuracy, and geometric assumptions with ultrasound, or large and costly systems with substantial infrastructure requirements with MRI. Here we present an automated four-dimensional ultrasound (4DUS) technique that provides comparable information to cine MRI through the spatiotemporally synced imaging of cardiac motion. Cardiac function metrics derived from SAX MM, cine MRI, and 4DUS data show close agreement between cine MRI and 4DUS, but overestimations by SAX MM. The inclusion of a mouse model of cardiac hypertrophy further highlights the precision of 4DUS compared to SAX MM, with narrower groupings of cardiac metrics based on health status. Our findings suggest that murine 4DUS can be used as a reliable, accurate, and cost-effective technique for longitudinal studies of cardiac function and disease progression.

### 2.2 Introduction

The development of murine cardiac disease models has become a foundation to systematically study mechanisms and factors that influence negative outcomes, such as heart

failure [5, 42, 57]. While *ex vivo* techniques (e.g. histology, proteomics) provide substantial information regarding gross and molecular composition, their information is limited to the state of tissue at sacrifice. *In vivo* imaging on the other hand can provide longitudinal information and result in a more comprehensive understanding of disease progression, particularly when studying changes in cardiac function. Though many noninvasive imaging modalities exist, high frequency ultrasound and cine magnetic resonance imaging (MRI) are most widely used to assess murine cardiac function [17, 18, 23].

High frequency ultrasound uses MHz frequency ultrasonic waves to acquire images of the heart, with contrast corresponding to differences in acoustic impedance between tissue types. This modality is particularly useful for imaging mice, as even with their rapid heart rates (approaching 600 bpm), near real-time temporal resolution can be achieved. Nevertheless, standard ultrasound imaging techniques for calculating cardiac function (e.g. short-axis motion-mode or M-Mode) require the use of geometric models to estimate the ventricular volumes as spheres, ellipsoids, or other shapes [16, 138]. While these geometric assumptions are commonly used to study heart function *in vivo* [10, 11], the left ventricle (LV) in a mouse has a complicated three-dimensional shape, which can increase in complexity with varying disease states.

Cardiac cine MRI exploits the contrasting magnetic properties of myocardial tissue and flowing blood to collect volumetric information across a heartbeat. These 4D (3D+time) data are spatiotemporally compiled from spatially adjacent slices of cine data across the heart. Compared to ultrasound, cine MRI takes longer to acquire since the region of interest must be sampled several times before each slice of cine data can be properly reconstructed. Still, cine MRI is often considered a gold-standard method for acquiring LV information as the chamber's entire boundary can be directly imaged [24, 28, 110]. Unfortunately, acquiring cine MRI data is often costlier due to system availability, maintenance, and required infrastructure needed to operate a superconducting magnet.

Building upon the idea of spatiotemporally compiling loops of MRI data, we present here an automated 4D ultrasound technique that can provide comparable information free of heuristics. We compared this technique against conventional short-axis M-Mode and cine MRI, using cardiac function metrics to assess their relative performance. The results of this murine study suggest that 4D cardiac ultrasound has advantages over standard 2D techniques and can be used as an alternative to cine MRI.

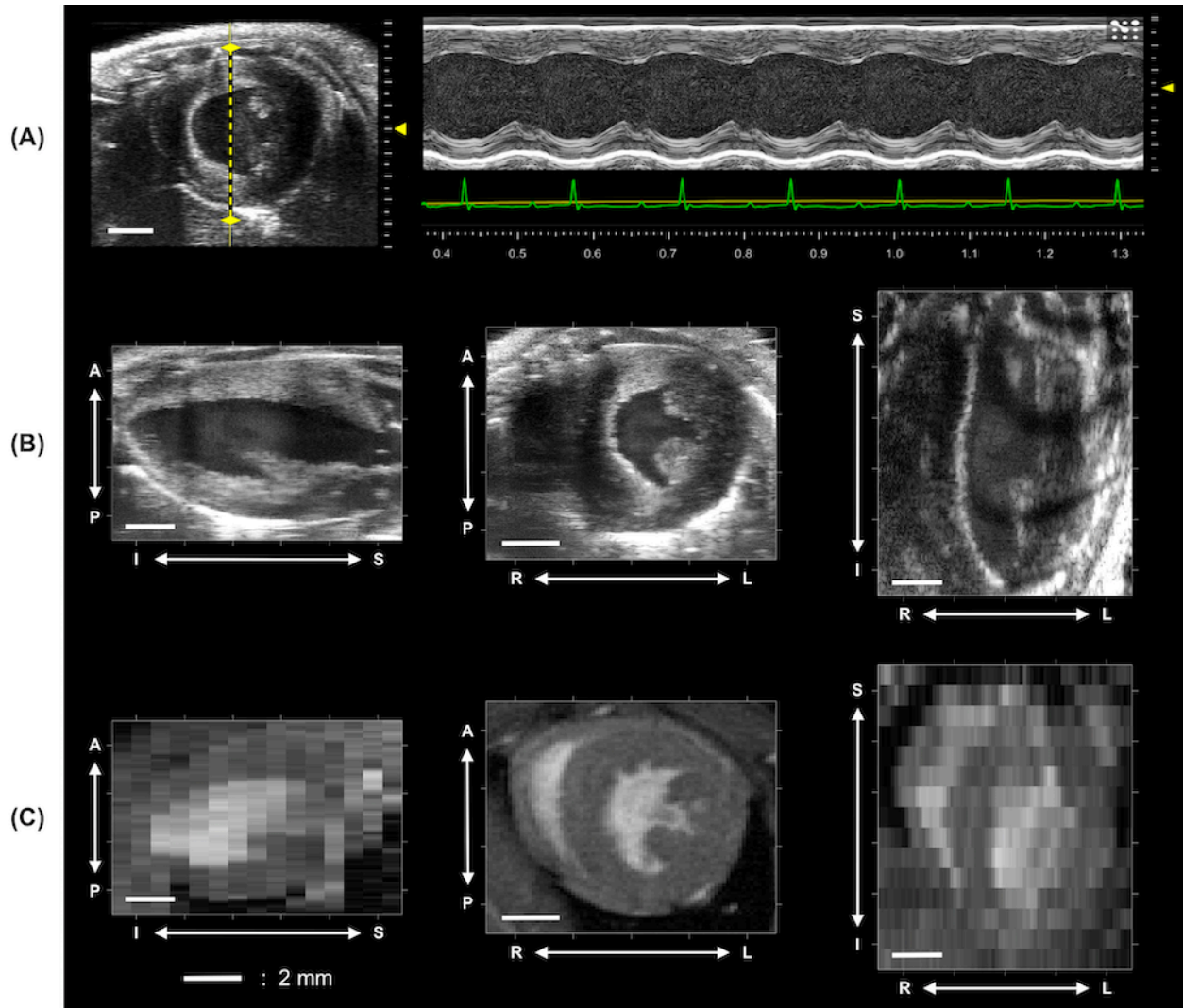


Figure 6. Representative displays of the imaging modalities used on a representative mouse: (top) short-axis MM (SAX MM), (mid) 4D ultrasound (4DUS), and (bottom) bright-blood gradient echo MRI. The SAX MM row shows the prescribed cursor for sampling (dashed yellow line) along with corresponding M-Mode data time-synced to ECG signals. The 4DUS and MRI rows both show long-axis (left), short-axis (center), and four-chamber (right) views at corresponding slice locations.

## 2.3 Methodology

### 2.3.1 Murine Models

A total of ten female mice were used in this study. All mice were bred at Purdue University and derived from *Cpt2*-floxed mice crossed with Cre-expressing mice where Cre was driven by the muscle creatine kinase promoter (Stock No: 006475; Jackson Laboratories, Bar Harbor, ME, USA; [79, 80]). Mice deficient in cardiac *Cpt2* (*Cpt2*<sup>M-/-</sup>; n = 5; age = 11.2 weeks; body mass = 20.1±0.71

grams), hereafter referred to as the *Cpt2<sup>M-/-</sup>* cohort, have impaired cardiomyocyte fatty acid oxidative metabolism due to compromised transport of long-chain fatty acids into the mitochondria through acyl-carnitine-mediated transport [79]. Our previous work showed that the loss of cardiac *Cpt2* results in left ventricular hypertrophy [80]. Control mice, hereafter referred to as the wild-type cohort, were littermates lacking the Cre gene (*Cpt2<sup>lox/lox</sup>*; n = 5; age = 11.2 weeks; body mass = 19.5±0.57 grams). All animal experiments were approved by the Purdue Animal Care and Use Committee.

### **2.3.2 Magnetic Resonance Imaging (MRI)**

Cardiac MRI data were compiled for each mouse from adjacent short-axis cine loops across the left-ventricle using a small-bore 7T MRI system (BioSpec 70/30 USR, Bruker Corporation, Billerica, MA). A circularly polarized transmit/receive <sup>1</sup>H volume coil was used in combination with a retrospectively-gated Fast Low-Angle SHot (IntraGateFLASH) sequence with in-slice navigator [106, 113] with a repetition time/echo time [TR/TE] = 7/3 ms; flip angle [FA] = 20°; slice thickness = 1.0 mm, cine frames = 14, matrix size = 256<sup>2</sup>, NEX = 1, field of view [FOV] = 35 x 25 mm, and pixel size = 137 x 98 μm. To help position sequential short-axis slices, a four-chamber long-axis view of the heart was acquired with similar parameters. Short-axis slices were prescribed ensuring coverage from the apex to the ascending aorta. Magnitude cine data were extracted and spatiotemporally concatenated into 4D data using MATLAB (MathWorks, Natick, MA, USA). Figure 6C shows representative MR data at end-diastole with axial, sagittal, and coronal slices through the center of the LV.

### **2.3.3 High-Frequency Ultrasound: 4DUS and Short-Axis M-Mode**

Four-dimensional ultrasound (4DUS) and short-axis M-Mode (SAX MM) data were acquired using a high frequency small animal ultrasound system (Vevo 3100, FUJIFILM VisualSonics Inc., Toronto, Ontario, Canada) and a 40 MHz center frequency linear array transducer (MX550D, FUJIFILM VisualSonics Inc.). In preparation for ultrasound imaging, depilatory cream was applied to the ventral thorax to prevent hair-based artifacts. The ultrasound probe was clamped to a linearly translating step motor and positioned parallel to the short-axis of the LV. System integrated triggering between the probe and motor automatically acquired high frame rate (300 fps)

cardiac- and respiratory-gated cine loops and spatiotemporally compiled them into 4D data. A volumetric FOV was prescribed to ensure that the end-diastolic epicardium would fit in all frames, spanning from the apex to the aortic valve. The axial and lateral pixel sizes were set at 12.0 x 55.2  $\mu\text{m}$  (axial resolution = 40  $\mu\text{m}$ ; lateral resolution = 90  $\mu\text{m}$ ), with a step-size of 76.2  $\mu\text{m}$ . Figure 6B shows a representative example of 4DUS data at end-diastole, with axial, sagittal, and coronal slices through the center of the LV, similar to the MR data display.

Following 4D data collection, the probe was positioned mid-papillary with a short-axis orientation. A line and cursor defining the SAX MM data was prescribed down the center of the ventricle, and approximately five seconds of data were acquired. Figure 6A shows a representation of the prescribed cursor and corresponding SAX MM data.

#### **2.3.4 Anesthesia and Physiological Monitoring**

Mice were anesthetized during each imaging procedure using a low-flow vaporizer (SomnoSuite, Kent Scientific, Torrington, CT, USA) with  $\sim 2.5\%$  isoflurane at 250 ml/min [139]. Exact anesthetic level was modulated as needed to maintain a heart rate near 500 beats per minute and respiration rate near 60 breaths per minute. During MRI, heart rate and respiration were monitored using three subcutaneous needle electrodes and a pneumatic pillow pressure sensor, respectively (SA Instruments, Stony Brook, NY, USA). Furthermore, each animal was maintained at 37°C using a feedback modulated fan that blew heated air into the bore of the magnet. During ultrasound imaging, a heated stage with integrated gold-plated electrodes (Vevo Imaging Station, FUJIFILM VisualSonics Inc.) warmed the animal to a temperature of approximately 37°C while also obtaining heart rate and respiratory signals. Respiratory signals were simultaneously extracted from gold-plated electrodes by filtering low frequency signal fluctuations, caused by changes in impedance across the lungs during inhalation. Rectal temperature probes were used to monitor core body temperature with both imaging systems.

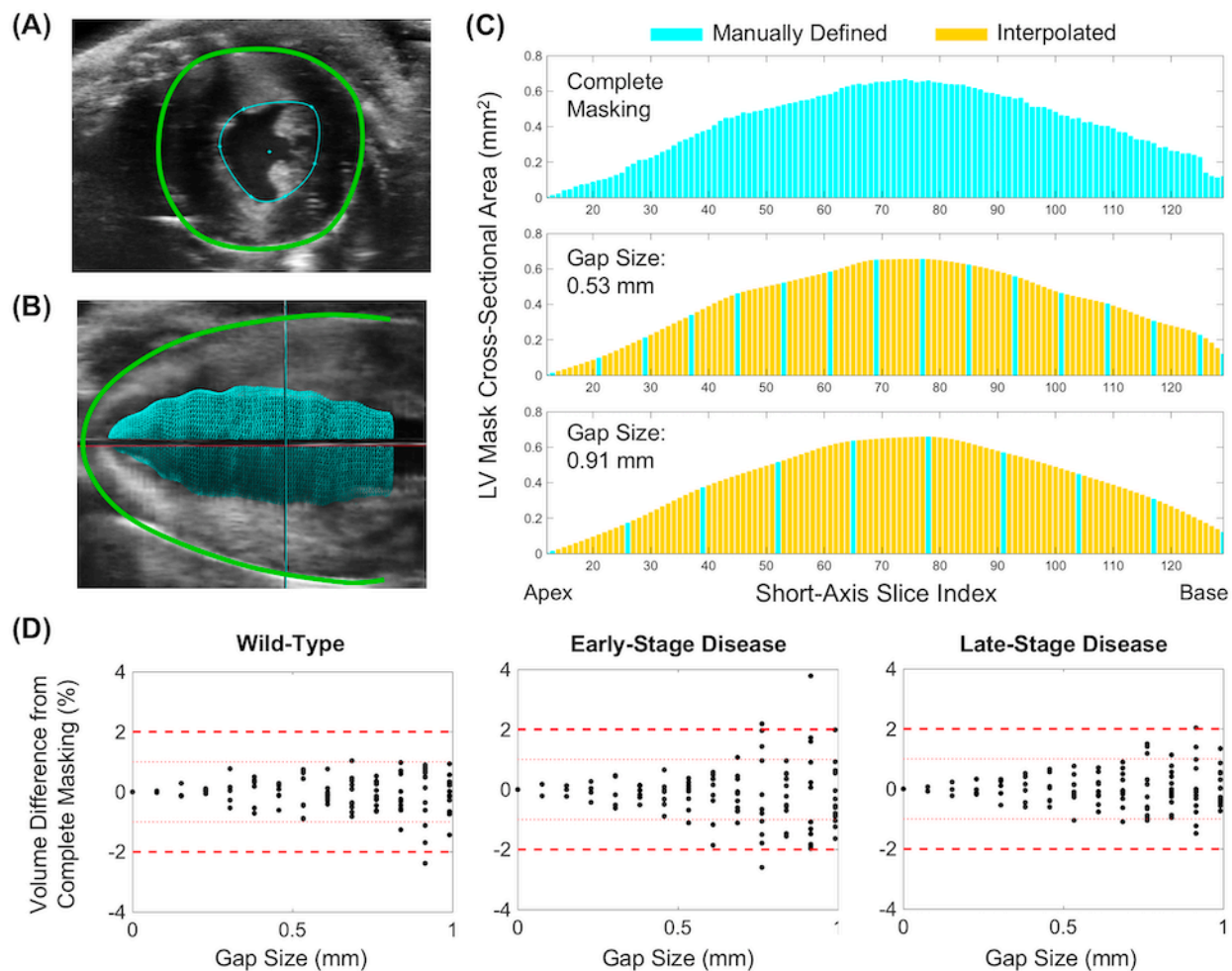


Figure 7. Overview of masking and slice analysis. Example (A) short-axis 4DUS slice with outlines of endocardial (blue) and epicardial (green) borders drawn. Adjacent short-axis border definitions are pieced together to create a volumetric mask, as shown in (B) with an example mask (blue) of the left ventricle in a long-axis view. The epicardial border (green) was included in (B) as well for reference. In order to identify the sensitivity of total mask volume to interpolated borders across skipped slices, (C; top) a complete masking (i.e. every slice across the volume was manually outlined) had equally sized subsets of slices deleted, (C; middle/bottom) which were subsequently filled using cubic spline interpolation. A slice thickness of 0.0762 mm was used to calculate physical gap sizes. At each gap size, the set of remaining slices – excluding the most proximal and distal slices – were serially shifted to identify variability based on gap positioning. Total volumes were calculated for each paradigm as the sum of all cross-sectional areas. Percent differences in volume from the complete masking across all gap paradigms are shown for a representative (D; left) wild-type, (D; middle) early stage disease, and (D; right) late stage disease mouse.

### 2.3.5 Cardiac Function Assessment

Using a custom MATLAB GUI and Vevo 3100 compatible VevoLAB analysis software (v3.0) for the MRI and 4DUS data, respectively, the endocardial and epicardial borders of the LV were manually outlined across short-axis views of the heart. The endocardial border was used to define the LV chamber, and the endocardial and epicardial borders were used in conjunction to define the LV myocardium. Maintaining conventions set by the American Society of Echocardiography [10, 11], the proximal extent of the LV cavity was defined as the mitral and aortic valves, and papillary muscles were considered part of the LV cavity. These guidelines were followed across all animals, regardless of gross differences in heart size or shape. Figure 7A and B illustrates an example of the aforementioned border definitions.

Expediting mask creation in the 4DUS data, we manually outlined slices that were approximately 0.3-0.5mm (i.e. 4-6 slices) apart and then used cubic spline interpolation to fill in the boundaries over skipped regions (e.g. Figure 7C; middle). In order to ensure that using such interpolation wouldn't produce large deviations from the expected ground truth, a sensitivity analysis was performed; LV mask volumes were compared over a series of gap size and position paradigms. Figure 7C shows an example cross-sectional area profile for a mask without any gaps (i.e. complete masking), as well as for two subsequent gap paradigms. Quantifying the percent difference in volume of every gap paradigm from the complete masking, Figure 7D demonstrates the results of sensitivity analysis for an example wild-type, early-stage disease, and late-stage disease mouse. We observed that gap sizes approximately 0.5mm or less did not produce percent differences in mask volumes over 1%, thus providing us confidence in the reliability of our masking protocol.

To extract measurements from the SAX MM data, the VevoLAB software was used to draw lines corresponding to the endocardial and epicardial borders through at least three cardiac cycles. Estimates of left ventricular geometry were thus calculated using the mean of corresponding measurements at end-diastole and peak-systole (i.e. maximum and minimum distances between endocardial borders). A single reviewer performed all measurements to prevent inter-operator variability.

Ventricular chamber volumes defined by the endocardial border from MRI and 4DUS data measured at end-diastole (EDV) and peak-systole (PSV) were used to calculate the LV stroke volume (SV) and ejection fraction (EF). To estimate the mass of the LV myocardium (i.e. Left

Ventricle Mass (LVM)), EDV was subtracted from the total volume defined by the epicardial border at end-diastole (EpiEDV), and the resultant volume multiplied by a cardiac tissue density of 1.05 mg/ $\mu$ L [140, 141]. The equations used to calculate cardiac function include:

$$EF = \frac{(EDV - PSV)}{EDV} \times 100 \quad [1]$$

$$SV = EDV - PSV \quad [2]$$

$$LVM = 1.05 \times (EpiEDV - EDV) \quad [3]$$

In contrast to direct measurements from the volumetric data, the M-Mode analysis used the Teichholz equation to quantify LV Volume (LVV),

$$LVV = \left( \frac{7.0}{(2.4 + LVID)} \right) \times LVID^3 \quad [4]$$

in which Left Ventricular Inner-Diameter (LVID) is used to estimate the geometry of the ventricle at any corresponding point in the cardiac cycle [142]. These estimated volumes at end-diastole and peak-systole were used with the same equations as above to calculate EF and SV. Calculations of LVM based on M-Mode data incorporated the measured thickness of the LV Anterior Wall (LVAW) and Posterior Wall (LVPW), as shown in the equation:

$$LVM = 1.05 \times [(LVID + LVAW + LVPW)^3 - LVID^3] \times 0.8 \quad [5]$$

### 2.3.6 Histology

Following imaging, mice were euthanized with CO<sub>2</sub> overdose and cervical dislocation. Hearts were excised and then placed directly in 4.0% paraformaldehyde (PFA) and stored at 4°C. After six days, hearts were transferred to 0.1% PFA and again stored at 4°C until histology was performed. Each heart was embedded in paraffin and sectioned along the mid-papillary short-axis of the LV. Tissue sections were stained with H&E and Masson's Trichrome following standard protocols.

### 2.3.7 Statistical Analysis

Differences between imaging methods were assessed in scatter dot plots. A one-way ANOVA with multiple comparisons was performed to identify significant differences between each pairing of

methods. In order to compare cardiac function metrics between the three methods and two groups of mice (wild-type and *Cpt2<sup>M-/-</sup>*), a two-way ANOVA with Tukey corrections for multiple comparisons was performed.

## 2.4 Results

The presented study introduces an automated 4DUS technique and compares its performance in assessing cardiac function against conventionally employed SAX MM and MRI methods. Quantified metrics of cardiac function (i.e. EDV, PSV, EF, SV, and LVM) from each of the three aforementioned techniques, acquired on each subject, were the basis for comparison. The 4DUS and MRI methods did not produce significant differences in any of the employed metrics, while SAX MM overestimated these values on average (Figure 8). A one-way ANOVA indicated a significantly larger EF from SAX MM versus 4DUS ( $p = 0.020$ ), larger SV from SAX MM versus both the 4DUS ( $p = 0.001$ ) and MRI methods ( $p = 0.005$ ), and larger EDV from SAX MM versus 4DUS ( $p = 0.021$ ). As cine MRI data are widely accepted as a gold-standard in measuring chamber volumes, our findings suggest that 4DUS could be a reliable alternative to cine MRI. Furthermore, as 4DUS and MRI do not rely on simplified models of LV geometries, these results provide further evidence that the geometric models used in SAX MM could be a source of inaccuracy in assessing cardiac function [10, 11, 16].

Subsequent analysis compared method performance taking into account cohort classifications (i.e. wild-type or *Cpt2<sup>M-/-</sup>*). Table 1 shows metric averages separated by cohort and identifies significant differences following a two-way ANOVA, which incorporated both imaging modality and cohort as factors. Neither wild-type or diseased mice demonstrated any significant difference between the 4DUS and MRI techniques, similar to the results of our initial one-way ANOVA analysis. However, significantly larger values were observed for SAX MM versus MRI methods in 1) the wild-type group for EDV ( $p = 0.014$ ) and SV ( $p = 0.002$ ), and 2) the diseased group for EF ( $p = 0.02$ ) and LVM ( $p = 0.002$ ). Furthermore, the SAX MM had significantly larger values than the 4DUS methods in 1) the wild-type group for EDV ( $p = 0.013$ ) and SV ( $p = 0.001$ ), and 2) the diseased group for SV ( $p = 0.014$ ) and LVM ( $p = 0.002$ ). The only insignificant interaction between imaging method and cohort was for LVM ( $p = 0.116$ ); however, this is most likely due to the large overestimation by SAX MM in the *Cpt2<sup>M-/-</sup>* cohort. Interestingly, SAX MM overestimated EDV in our wild-type mice, but the differences in LVM measurements were not

significant; an opposite trend observed in the *Cpt2<sup>M/-</sup>* group. We originally hypothesized that if either SAX MM metric would be inaccurate, it would be when cardiac morphology deviated from the wild-type state. Instead, the observed overestimation of LVM in the wild-type cohort suggests that the wild-type murine myocardium may be smaller than assumed in the employed geometric models. Conversely, future use of SAX MM in murine models may consider refinement of the equations used to calculate the presented metrics, to better match the morphology of the murine heart.

Table 1. Average values for all measured and calculated metrics for (A) wild-type and (B) *Cpt2<sup>M/-</sup>* cohorts. Two-way ANOVA analysis with Tukey post-hoc comparisons were performed on the shown data. Significant within-group differences are designated with \* for SAX MM versus MRI values and + for SAX MM versus 4DUS values, as well as one, two, or three symbols for significance levels of  $p < 0.05$ ,  $p < 0.01$ , and  $p = 0.001$ , respectively. No significant differences were found between the 4DUS and MRI values for any metrics.

| (A)    | Wild-Type Mice           |                |               |                   |                    |
|--------|--------------------------|----------------|---------------|-------------------|--------------------|
|        | EDV ( $\mu$ L)           | PSV ( $\mu$ L) | EF (%)        | SV ( $\mu$ L)     | LVM (mg)           |
| SAX MM | 51.1 (14.4) **+          | 20.2 (9.4)     | 62.0 (8.5)    | 30.9 (6.2) **,+++ | 73.7 (9.6)         |
| MRI    | 38.2 (3.1)               | 15.8 (1.6)     | 58.6 (3.1)    | 22.4 (2.3)        | 75.6 (8.4)         |
| 4DUS   | 38.1 (5.8)               | 16.9 (2.8)     | 55.7 (2.1)    | 21.2 (3.2)        | 69.2 (3.0)         |
| (B)    | CPT2 <sup>M/-</sup> Mice |                |               |                   |                    |
|        | EDV ( $\mu$ L)           | PSV ( $\mu$ L) | EF (%)        | SV ( $\mu$ L)     | LVM (mg)           |
| SAX MM | 61.2 (26.3)              | 30.7 (26.6)    | 56.1 (18.9) * | 30.4 (4.7) +      | 235.5 (89.9) **,++ |
| MRI    | 61.6 (27.5)              | 35.6 (25.1)    | 46.4 (12.3)   | 26.0 (3.9)        | 166.9 (39.7)       |
| 4DUS   | 52.9 (21.6)              | 28.9 (21.4)    | 50.5 (15.9)   | 24.0 (2.0)        | 166.7 (33.1)       |

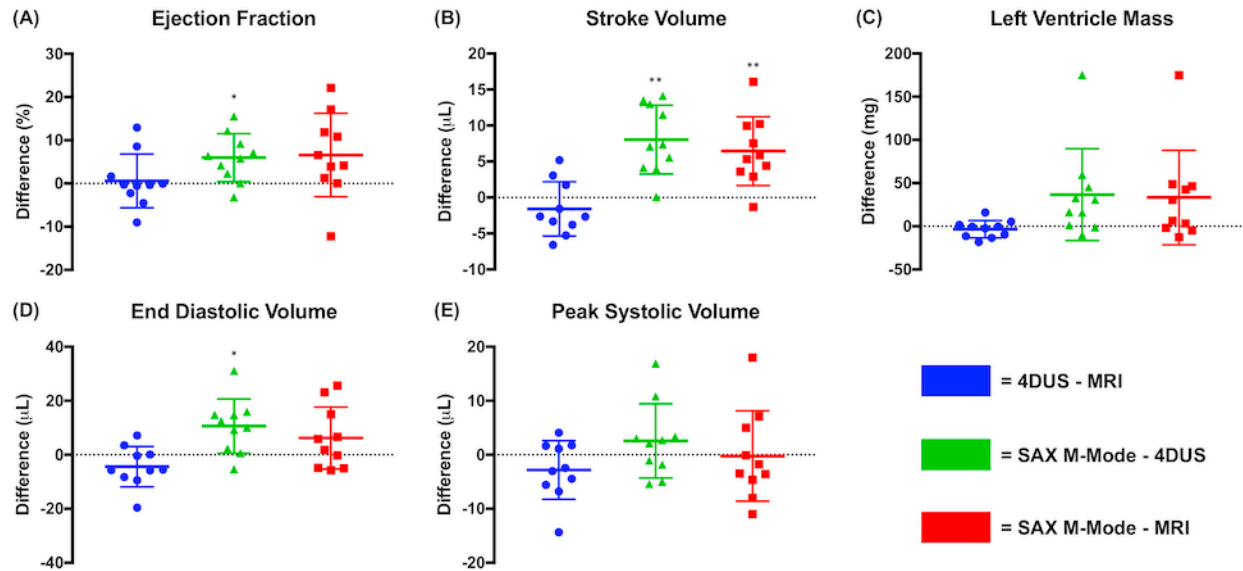


Figure 8. Scatter dot plots with mean and standard deviation bars comparing measurement differences between each pair of imaging methods. In each plot, the left blue column represents the 4DUS - MRI values, the green center column represents the SAX MM - 4DUS values, and the red right column represents the SAX MM - MRI values. The plots of (A) ejection fraction, (B) stroke volume, and (C) left ventricle mass each represent metrics derived from volume estimates made at (D) end-diastole and (E) peak-systole, commonly used to evaluate left ventricular function. One-way ANOVA analysis identified statistical significance between methods as designated by \* ( $p < 0.05$ ) and \*\* ( $p < 0.01$ ) respectively.

While we have so far focused on the agreement between each imaging modality, the use of *Cpt2<sup>M-/-</sup>* mice also demonstrate the benefit of acquiring reliable function metrics toward characterizing cardiac remodeling and the ultimate progression to heart failure. As observed in recent literature, this mouse model develops early concentric hypertrophy of the LV followed by chamber dilation [80]. Representative histology (Figure 9) confirms the presence of both late (n=2) and early (n=3) stages of the disease within the *Cpt2<sup>M-/-</sup>* cohort, characterized by gross cardiomyocyte hypertrophy with or without notable cardiomyocyte necrosis (i.e. hyper eosinophilia and loss of cross striations), respectively. Plots of EF versus SV and EDV versus LVM (Figure 10) illustrate how both the wild-type and diseased cohorts can be characterized by physiologic or morphologic oriented metrics, respectively. In plots of EF versus SV, we note that while stroke volume is relatively conserved for all mice, only early stage disease mice preserve an EF comparable to wild-type mice. In plots of EDV versus SV, both metrics seem to gradually increase with the relative stage of disease, illustrating somewhat distinct groupings based on the

wild-type, *Cpt2*<sup>M/-</sup> phenotype with early-stage disease, and *Cpt2*<sup>M/-</sup> phenotype with late-stage disease. To demonstrate these groupings, data was displayed both as individual points and average distributions for the wild-type and *Cpt2*<sup>M/-</sup> cohorts. These plots qualitatively exhibit the method agreement between MRI and 4DUS methods that have been quantitatively studied above.

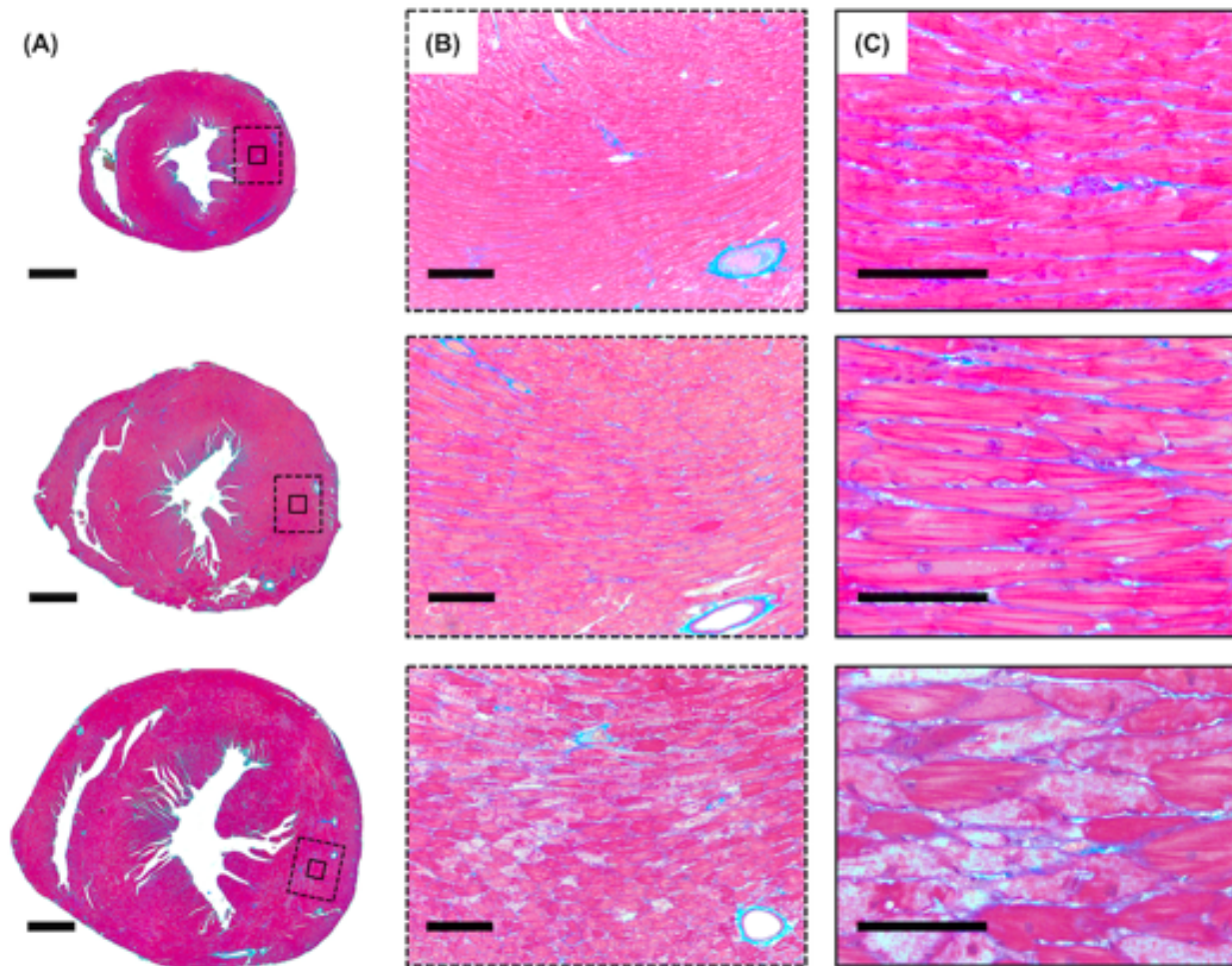


Figure 9. Representative Masson's Trichrome histology of the various disease stages imaged, with magnifications at (A) 4x (scale bar = 1.0mm), (B) 10x (scale bar = 200  $\mu$ m), and (C) 40x (scale bar = 100  $\mu$ m). The first row shows a representative non-mutated mouse (n = 5) in which wild-type cardiomyocyte size and density is observed. The second row shows an early stage of hypertrophy (n = 3) where enlarged cardiomyocytes are observed without any noticeable necrosis. The third row shows a late stage of hypertrophy (n = 2) in which enlarged cardiomyocytes and cell necrosis with less stain uptake are both observed.

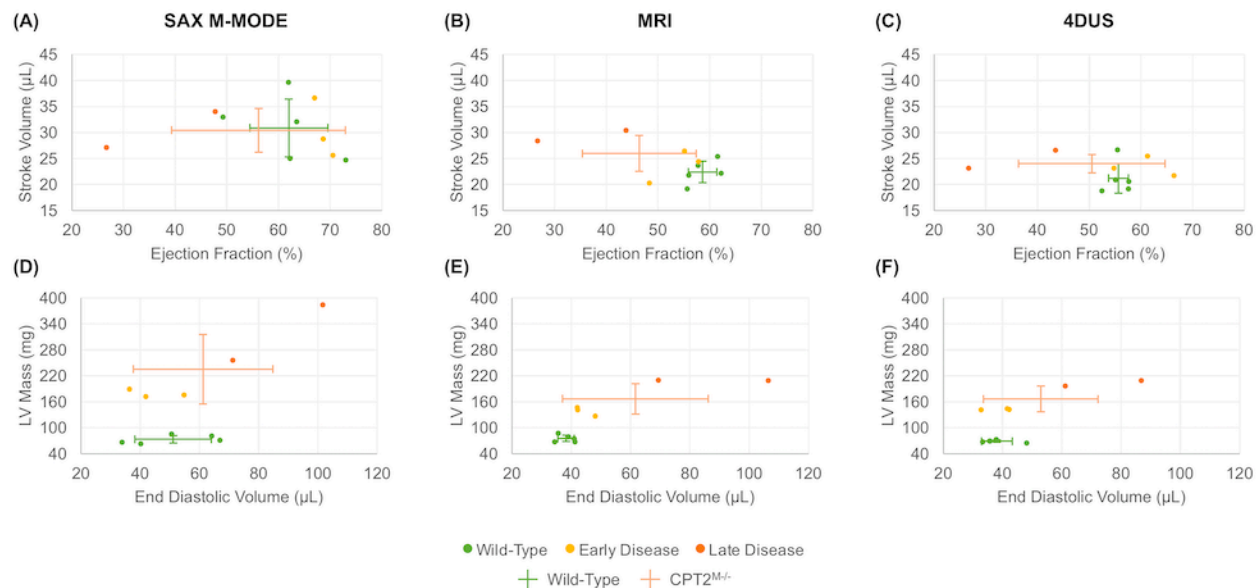


Figure 10. Characterization plots of the wild-type, early stage disease, and late stage disease mice derived from the 4DUS based metrics. The top three plots of EF versus SV for (A) SAX MM, (B) MRI, (C) 4DUS illustrate the relative spread of cardiac function metrics across the study animals. Distributions are more closely matched for the MRI and 4DUS techniques. This agreement in metric distributions is also observed for the structural metrics EDV versus LVM (D-F). The characteristics expected for the  $Cpt2^{M-/-}$  model are highlighted in these plots showing relative clusters depending on health status.

## 2.5 Discussion and Conclusion

Despite the advantages of 4DUS including rapid acquisition (e.g. 5-10 min for 4DUS, <1 min for SAX MM, and 45-60 min for cine MRI), relatively low-cost, and high spatiotemporal resolution, this approach does have several limitations compared to cine MRI. Sternum, rib, and lung artifacts limit the imaging window and can obscure portions of the heart. This can be particularly hindering if interested in right ventricular pathologies, as the sternum artifact can blur a large portion of its endocardial borders. Second, similar to cine MRI, accurate ECG and respiration signals are required to spatiotemporally compile the 4DUS images. To this end, pathologies which suffer from cardiac arrhythmias will need to be tested to ensure proper spatiotemporal compilation. Third, the higher spatial and temporal resolution of 4DUS information comparably increases the digital size of the data. While most commonly available computational resources can handle such data sizes for analysis, down-sampling in the spatial and/or temporal domain can serve to reduce computational costs if desired.

In conclusion, we demonstrate in this study that 4DUS can provide data comparable to cine MRI for quantifying cardiac function metrics, with improved precision and accuracy over SAX MM ultrasound. Nevertheless, SAX MM is used widely as a relatively rapid and economical option for longitudinal studies of cardiac disease in murine studies [17, 18]. Fortunately, the benefits of ultrasound and volumetric acquisition can be combined with only a slightly longer scan time compared to SAX MM. Using 4DUS imaging, rapid assessments with high frequency ultrasound can be conducted with the crucial advantage of producing reliable measurements similar to the gold-standard of cardiac MRI without assuming an idealized geometric model. Furthermore, the added benefit of higher through-plane resolution compared to MRI may help provide clearer data for studying cardiac disease models in which the myocardium evolves into even more complex shapes (e.g. myocardial infarction). In the following section, we will outline the research planned to take this next step with the 4DUS technology, further exploring regional metrics of cardiac function extracted for the 4DUS data and how those metrics may help explain disease progression.

### 3. REGIONAL KINEMATIC ANALYSIS OF DISEASE PROGRESSION IN CPT2<sup>M/-</sup> MODEL OF HYPERTROPHIC CARDIOMYOPATHY

In this section, we highlight an application of 4DUS imaging to study cardiac dysfunction progression in murine model of hypertrophic cardiomyopathy (*Cpt2*<sup>M/-</sup>). We detail here a standardized procedure for analyzing 4DUS data and simultaneously extracting measurements of left-ventricular global function, morphometry, and regional strain. We further pose a novel metric, the Hybrid Strain Index (HSI), which demonstrates the greatest utility in characterizing disease progression. The content presented in this chapter has been submitted for publication in *American Journal of Physiology Heart and Circulatory Physiology* entitled “Improving characterization of hypertrophy-induced murine cardiac dysfunction progression using four-dimensional ultrasound derived strain metrics”.

#### 3.1 Abstract

Mouse models of cardiac disease have become essential tools in the study of pathological mechanisms, but the small size of rodents makes it challenging to quantify heart function with noninvasive imaging. Building off recent developments in high-frequency four-dimensional ultrasound (4DUS) imaging, we have applied this technology to study cardiac dysfunction progression in a murine model of hypertrophic cardiomyopathy. Cardiac knockout of carnitine palmitoyltransferase 2 (*Cpt2*<sup>M/-</sup>) in mice hinders cardiomyocyte bioenergetic metabolism of long-chain fatty acids, and leads to progressive hypertrophic cardiomyopathy and heart failure. The proposed analysis provides a standardized approach to measure localized wall kinematics and simultaneously extract metrics of global cardiac function, LV morphometry, regional circumferential strain, and regional longitudinal strain from an interpolated 4D mesh of the endo- and epi-cardial boundaries. Comparison of metric changes due to aging suggest that circumferential strain at the base and longitudinal strain along the posterior wall are most sensitive to disease progression. We further introduce a novel Hybrid Strain Index (HSI) that incorporates information from these two regions and may have greater utility to characterize disease progression relative to other extracted metrics. Future work will look to apply these methods to additional

disease models and further demonstrate the utility of metrics derived from 4DUS imaging and strain mapping.

### 3.2 New & Noteworthy

High-frequency four-dimensional ultrasound can be used in conjunction with standardized analysis procedures to simultaneously extract left-ventricular global function, morphometry, and regional strain metrics. Furthermore, a novel hybrid strain index (HSI) formula demonstrates greater performance compared to all other metrics in characterizing disease progression in a model of hypertrophic cardiomyopathy.

### 3.3 Introduction

Due to the heart's central role in the distribution of oxygen, nutrients, signaling factors, and heat throughout the body, progressive cardiac dysfunction can not only compromise an individual's quality-of-life, but also lead to systemic organ failure, morbidity, and mortality [33]. While cardiac hypertrophy is often a non-pathogenic adaptation to cardiovascular stress (e.g., aerobic exercise), when stressors persist or cardiomyocyte adaptation is compromised, the heart may progress to hypertrophic cardiomyopathy (HCM) [31, 34, 40]. Conditions that cause HCM, such as metabolic disease and hypertension, result in dysfunctional fatty acid oxidative metabolism in the myocardium, thereby limiting biogenetic contributions an important energy substrate for the heart [143, 144]. As such, patients and animal models genetically predisposed to metabolic inflexibility present with often severe forms of HCM [145-149].

Establishing a better understanding of the pathological mechanisms and progression of HCM using murine models allows for controlled manipulations of disease-linked factors and longitudinal monitoring of cardiac function [5-9, 150]. Herein we focus on one such model, in which HCM is induced due to a cardiac homozygous knockout of the carnitine palmitoyltransferase 2 (*Cpt2*) enzyme in the heart. We have demonstrated that deficiency of CPT2, a required enzyme for mitochondrial fatty acid oxidation of long-chain fatty acids, causes cardiomyocyte metabolic inflexibility and leads to progressive myocardial hypertrophy [79, 80].

Complementary to such murine models of cardiac disease, high-frequency ultrasound has become one of the most commonly used imaging tools to longitudinally and non-invasively

monitor heart function. Traditional ultrasound transducers for small animals only allow for planar imaging, thus reported metrics of global cardiac function (e.g., ejection fraction, stroke volume, cardiac output) heavily rely on predictions of the idealized geometries of the left ventricle (LV) [14, 16-18]. Fortunately, measurements of regional left-ventricular strain can be derived directly from planar imaging views and demonstrate greater sensitivity to myocardial function compared to ejection fraction [151]. Still, collection of multiple non-parallel views of the left-ventricle requires physical repositioning of the ultrasound probe, introducing potential misalignment errors when comparing values within a mouse or across animals. Recent advancements in high-frequency four-dimensional ultrasound (4DUS) imaging mitigates these issues, providing gated volumetric data of the entire murine left-ventricle, with faster acquisitions and higher spatiotemporal resolution compared to high-field cine-MRI [29, 30, 152].

Using a series of longitudinal 4DUS data collected from both *Cpt2<sup>M/-</sup>* mice and littermate controls, we describe here for the first time a standardized method for extracting regional kinematics information from the endo- and epi-cardial boundaries of the LV myocardium and investigate how cardiac strain metrics derived from these kinematic data can be used to characterize disease progression. Furthermore, we propose a hybrid strain index (HSI) metric which combines basal circumferential and posterior free-wall longitudinal strains, and demonstrate its superior utility in characterizing HCM progression.

## 3.4 Methods

### 3.4.1 Animal Models and Study Timeline.

Heart and skeletal muscle (*Cpt2<sup>M/-</sup>*) CPT2 conditionally deficient C57BL/6 female mice were generated using the MCK-Cre mice (Jackson Laboratories stock no. 006475) as described [80]. Littermates lacking Cre expression were used as controls. Mice were given free access to water and standard chow (PicoLab 5053, Lab Diets), in pathogen-free housing under 12-hour light-dark cycles. A total of 26 mice were used for this study, comprised of 12 *Cpt2<sup>M/-</sup>* mice (47 total 4DUS datasets) and 14 littermate controls (41 total 4DUS datasets), each imaged longitudinally at least twice between 4 and 18 weeks of age. Figure 11 provides example 4DUS images, gross sections, and histology from a representative mouse in each cohort. *Cpt2<sup>M/-</sup>* and littermate control mice were euthanized at week 18 and had hearts freshly isolated and similarly prepared for histology

(H&E and Masson's Trichrome). If all *Cpt2<sup>M/-</sup>* mice in a cohort died prior to week 18, the corresponding littermate controls were euthanized. All animal experiments were approved by the Purdue Animal Care and Use Committee.

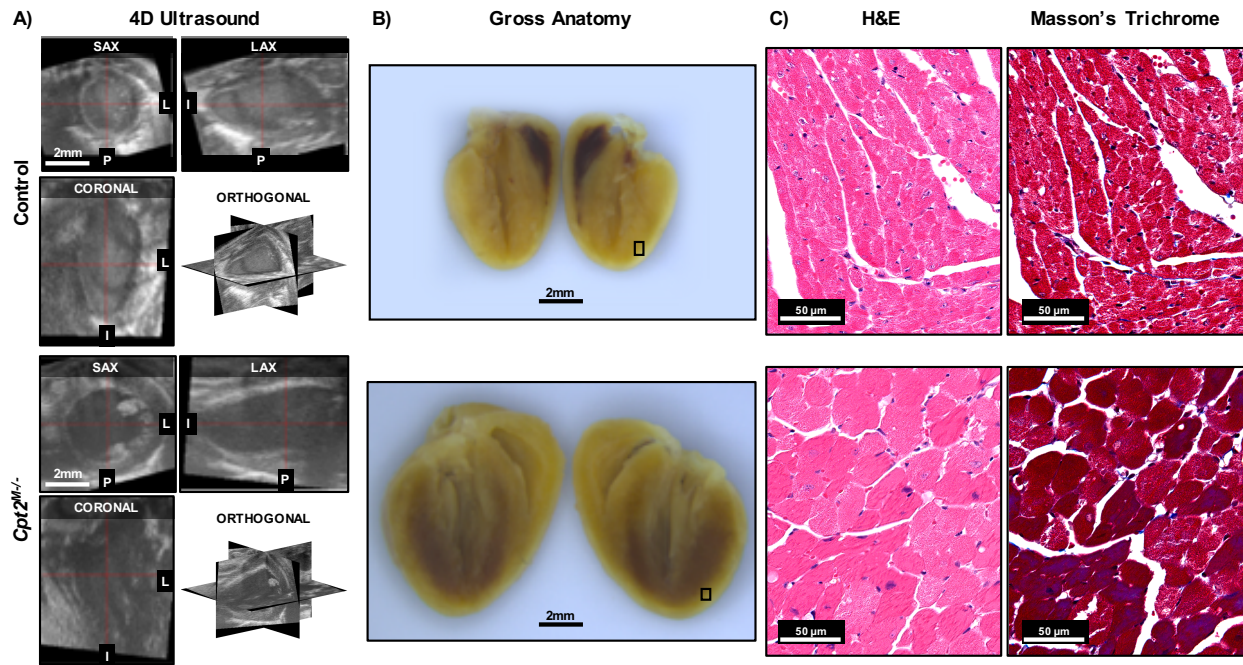


Figure 11. *Cpt2<sup>M/-</sup>* induced hypertrophy compared to control. Representative control (top) and *Cpt2<sup>M/-</sup>* (bottom) mouse hearts at 15 weeks of age visualized with A) three orthogonal views from four-dimensional ultrasound (4DUS) data at end-diastole, B) gross anatomical sections post-fixation, and C) H&E and Masson's Trichrome histology from selected box regions. Ultrasound and gross section scale bar = 2mm. Histology scale bar = 100µm. Ultrasound image planes are designated as short-axis (SAX), long-axis (LAX), and coronal; orientation is designated with labels for the posterior (P), inferior (I), and left (L) sides of the heart.

### 3.4.2 Ultrasound Imaging

4DUS data was collected using the Vevo2100 high-frequency ultrasound system (FUJIFILM VisualSonics Inc., Toronto, Ontario, Canada), a 40 MHz center frequency transducer (MS550D), and a translating linear step motor. Mice were weighed prior to imaging and then anesthetized using a low-flow vaporizer (SomnoSuite, Kent Scientific, Torrington, CT, USA) with ~2.5% isoflurane at 250 ml/min [139]. Mice were then secured to a heated stage with gold-plated electrodes and had ventral thorax hair removed using depilatory cream. Serial short-axis ECG-gated Kilohertz Visualization (EKV) cine loops were acquired across the full left-ventricle (i.e., inferior to the epicardial apex through superior to the aortic valve), with step sizes of approximately

200  $\mu\text{m}$  and gating by cardiac- and respiratory-signals [29, 30]. Extracted ultrasound data was then spatiotemporally compiled into a 4DUS dataset in MATLAB (MathWorks Inc., Natick, MA).

### 3.4.3 Boundary Definition and Kinematics Analysis.

An in-house MATLAB graphical user interface (GUI) was used to visualize 4DUS data and track LV kinematics along the endo- and epi-cardial borders. Figure 12 shows a schematic representation of the standardized analysis procedure:

- A. Spatially reorient volumes to a standard set of x, y, and z axes (i.e., the apex-to-base line defines a central z-axis, the anterior and posterior walls lie perpendicular to the y-axis, and the free-wall and septum lie perpendicular to the x-axis);
- B. Track the translation of the LV chamber base and apex along the z-axis throughout the cardiac cycle;
- C. Using a grid of automatically defined endo- and epi-cardial boundary points, track local wall motion throughout the cardiac cycle using the distance between each point and the central z-axis as reference; and
- D. Using the tracked grid positions, interpolate a final 4D mesh of each boundary, sampled uniformly at 60 rotations around the z-axis, 60 slices from base to apex, and at 60 time points across the cardiac cycle.

The grid defined in step C is structured such that points lie along four parallel short-axis slices (i.e., 25, 50, 75, and 100% from the apex to base) and at six rotations around the kinematic axis (i.e., 30, 90, 150, 210, 270, and 330° from the free-wall oriented axis). As the base and apex positions are time dependent, tracked in step B, the z-positions of grid points are subsequently dependent on the base and apex positions at any given point across the cardiac cycle.

Using the derived 4D meshes of each LV boundary, measurements of global cardiac function (e.g., ejection fraction, stroke volume), LV morphometry (e.g., end diastolic volume, left-ventricular mass), and regional strain were calculated, similar to those previously reported [15, 153, 154].

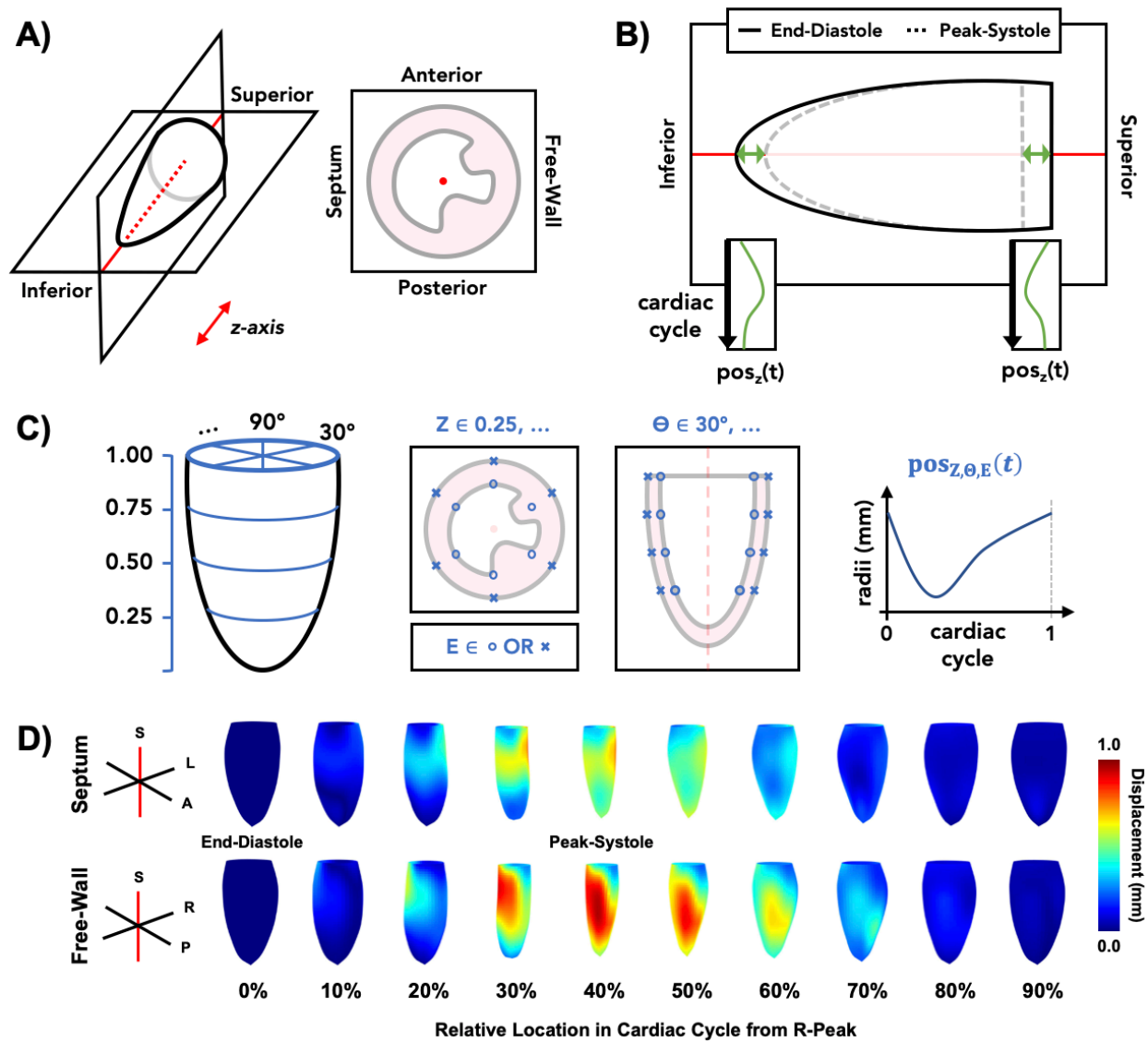


Figure 12. Schematic for standardized 4DUS analysis procedure. The outlined steps include: A) reorientation of data to defined axes, B) tracking z-axis position ( $pos_z$ ) of the left-ventricular base and apex across relative time ( $t$ ) in the cardiac cycle, C) defining and tracking local wall motion ( $pos_{z,\theta,E}$ ) at a grid of endo- ( $E=0$ ) and epi-cardial ( $E=x$ ) points equally spaced across four short-axis slices ( $Z$ ) and six rotations ( $\theta$ ) around the left ventricle, and D) quantification of regional kinematics from which strain metrics are calculated. Meshes in section D) are oriented such that the viewer is looking at the septal wall (top) or the free-wall (bottom), at 10% increments throughout a representative cardiac cycle. Red-axes denote the same central “z-axis” that the data is oriented to in the first step.

### 3.4.4 Derivation of Regional Cardiac Strain.

We calculated the circumferential component of the Green-Lagrange strain tensor to estimate cyclic strain ( $E_{\theta\theta}$ ), assuming a circular cross-section at each short-axis slice location [155]:

$$E_{\theta\theta}(z, t) = \frac{1}{2} \left( \left( \frac{C(z, t)}{C_D(z)} \right)^2 - 1 \right) \quad [6]$$

where  $C$  represents the relative circumference at short-axis slice  $z$  and time  $t$  in the cardiac cycle;  $C_D$  is the circumference at end-diastole (i.e.,  $t=0$ ). Curves of  $E_{\theta\theta}$  were derived for slices corresponding to the basal, mid-ventricular, and apical regions of the left ventricle, from which peak-strain, early systolic strain rate, late systolic strain rate, early diastolic strain rate, and late diastolic strain rate were extracted.

Complementary measurements of longitudinal ( $E_{LL}$ ) strain were calculated using the engineering linear small strain approximation:

$$E_{LL}(\theta, t) = \frac{L(\theta, t) - L_D(\theta)}{L_D(\theta)} \quad [7]$$

where  $L$  represents the apex-to-base length along the boundary at rotation  $\theta$  and time  $t$  in the cardiac cycle, and  $L_D$  is the respective length at end-diastole. Metrics of peak-strain, systolic strain rate, early diastolic strain rate, and late diastolic strain rate were similarly extracted for each of the strain curves corresponding to the anterior free-wall, anterior, anterior septum, posterior septum, posterior, and posterior free-wall sections of the heart.

### 3.4.5 Hybrid Strain Index

Since the circumferential and longitudinal reference frames reflect the two conventional views of the LV (i.e. short-axis and long-axis), we sought to investigate whether a combination of the most sensitive location-specific metric in each respective reference frame could create an even better marker of cardiac dysfunction progression. Thus, we propose here a novel metric, the Hybrid Strain Index (HSI):

$$HSI = \sqrt{E_{\theta\theta,Base}^2 + E_{LL,Posterior}^2} \quad [8]$$

computed as the L2 norm of the peak circumferential strain value at the base of the heart ( $E_{\theta\theta,Base}$ ) and peak longitudinal strain value along the posterior wall ( $E_{LL,Posterior}$ ), which were identified as the most sensitive metrics in the circumferential and longitudinal reference frames, respectively.

### 3.4.6 Longitudinal Metric Analysis

To assess the rate of change in each studied metric through time, a linear regression was fit to values from the same animal against age at the time of imaging. Herein, we refer to the slope derived from linear regression as the metric's "trend". Additionally, to assess changes as a function of genotype and age only, a linear regression was fit to a pool of all values from each cohort against the age at imaging, treating all data as independent. Using 95% confidence intervals (CI) associated with linear regression from each cohort, the earliest age at which the CIs no longer overlap was used as a marker for how soon the respective metric might be able to differentiate *Cpt2<sup>M/-</sup>* mice from controls.

### 3.4.7 Receiver Operating Characteristic Analysis

In order to quantify the degree to which each metric can differentiate data from each cohort, using either the metric value or aging-based trends, we calculated area under the curve (AUC) values for each respective receiver operating characteristics (ROC) curve. While disease progression in the *Cpt2<sup>M/-</sup>* cohort was variable (i.e., some mice died prematurely while others reached 18 weeks of age to be sacrificed), all *Cpt2<sup>M/-</sup>* mice were considered to represent progressive cardiac dysfunction.

### 3.4.8 Statistics

All statistical tests were performed in Prism (GraphPad Software, San Diego, CA). Cohort differences in metric trends were investigated using a non-parametric Mann-Whitney test, and  $p < 0.05$  was considered statistically significant. All cohort-specific metric trend summaries are reported as median [interquartile range]. To further assess the relative variability of metric trends in the *Cpt2<sup>M/-</sup>* cohort compared to control, an interquartile range (IQR) ratio is computed:

$$IQR\ Ratio = \frac{IQR_{Cpt2}}{IQR_{control}} \quad [9]$$

where  $IQR_{Cpt2}$  is the interquartile range of the *Cpt2<sup>M/-</sup>* cohort values, and  $IQR_{control}$  is the respective interquartile range of the control cohort values. Metric summary information, Mann-Whitney test  $p$ -values, IQR ratio, AUC values, and 95% CI intersections for all computed metrics,

except strain rate, are reported in Table 2. All comparable information for strain rate metrics are reported in Supplemental Table 1.

## 3.5 Results

### 3.5.1 Global Function and LV Morphometry

Three-dimensional renderings of a representative heart are shown in Figure 13A at end-diastole and peak-systole, from which global cardiac function and morphometry measurements were calculated. Focusing on longitudinal changes in each animal, Figure 13B, D, and E show significant trend differences in ejection fraction (EF), end-diastolic volume (EDV), and left-ventricular mass (LVM), respectively. No significant trend differences were observed for stroke volume (SV; Figure 13A) or wall thickness (Figure 13F). Figure 13C demonstrates with EF the use of linear regression 95% confidence intervals to identify the earliest age at which the confidence intervals no longer overlap; subsequent measurements for all metrics are shown in Table 2. It is notable that stroke volume showed no separation based on 95% CI, suggesting that regardless of age no significant differences in stroke volume would be observed. Furthermore, both left-ventricular mass and wall thickness had no overlapping regions of 95% CI, suggesting that significant differences between control and *Cpt2<sup>M/-</sup>* mice were present even prior to four weeks of age. EF demonstrated the highest AUC value (AUC = 1.000) amongst all global function trends, with an 95% CI intersection at 7.11 weeks of age (Table 2); however, produced a lower AUC (AUC = 0.839) compared to left-ventricular mass (AUC = 0.949) and wall thickness (AUC = 0.981) when comparing metric values independent of age.

Table 2. Measurements of metric trends through aging. For each cohort, medians [interquartile ranges] are provided for control and *Cpt2<sup>M-/-</sup>* mice, along with p-values from Mann-Whitney tests, ratio of interquartile ranges (IQR) in *Cpt2<sup>M-/-</sup>* and control trends, area under curve (AUC) values, and the 95% confidence interval (CI) intersection locations. Metrics where 95% confidence intervals overlapped for the entire age range of the study were noted with “---”, and metrics where 95% confidence intervals did not overlap are noted with “DNO”.

| Metric                                    | Control (n=14)        | <i>Cpt2<sup>M-/-</sup></i> (n=12) | p-value             | IQR Ratio | Trend AUC | 95% CI Int. | Metric AUC |       |
|-------------------------------------------|-----------------------|-----------------------------------|---------------------|-----------|-----------|-------------|------------|-------|
| <b>End-Diastolic Volume</b>               | 0.711 [0.187,1.194]   | 5.826 [2.537,16.037]              | 0.0001              | 13.40     | 0.946     | 8.96        | 0.720      |       |
| <b>Peak-Systolic Volume</b>               | 0.265 [0.048,0.603]   | 5.768 [1.850,16.034]              | 0.0000              | 25.57     | 0.988     | 8.64        | 0.789      |       |
| <b>Stroke Volume</b>                      | 0.397 [0.037,0.802]   | 0.281 [-0.086,0.687]              | 0.6620              | 1.01      | 0.554     | ---         | 0.536      |       |
| <b>Ejection Fraction</b>                  | -0.205 [-0.741,0.216] | -3.364 [-6.559,-1.633]            | 0.0000              | 5.15      | 1.000     | 7.11        | 0.839      |       |
| <b>Left Ventricle Mass</b>                | 2.078 [1.299,2.525]   | 9.302 [8.599,25.402]              | 0.0000              | 13.71     | 0.988     | DNO         | 0.949      |       |
| <b>LV Wall Thickness</b>                  | 0.007 [0.003,0.010]   | 0.024 [0.002,0.034]               | 0.0760              | 4.85      | 0.708     | DNO         | 0.981      |       |
| <b>Peak <math>E_{\theta\theta}</math></b> | <b>Base</b>           | 0.106 [-0.093,0.404]              | 1.586 [1.065,3.148] | 0.0000    | 4.19      | 0.988       | 6.52       | 0.861 |
|                                           | <b>Mid-LV</b>         | 0.181 [-0.157,0.435]              | 1.712 [0.670,3.346] | 0.0002    | 4.52      | 0.929       | 8.30       | 0.730 |
|                                           | <b>Apical</b>         | 0.007 [-0.126,0.338]              | 1.787 [0.414,2.840] | 0.0037    | 5.22      | 0.839       | 9.77       | 0.652 |
| <b>Peak <math>E_{LL}</math></b>           | <b>Ant. FW</b>        | 0.168 [-0.006,0.429]              | 0.898 [0.547,1.118] | 0.0002    | 1.31      | 0.929       | 4.58       | 0.903 |
|                                           | <b>Anterior</b>       | 0.129 [-0.043,0.396]              | 0.893 [0.496,1.089] | 0.0002    | 1.35      | 0.940       | 6.06       | 0.860 |
|                                           | <b>Ant. Sep.</b>      | 0.160 [-0.026,0.361]              | 0.845 [0.509,1.115] | 0.0001    | 1.57      | 0.952       | 6.91       | 0.821 |
|                                           | <b>Post. Sep</b>      | 0.062 [-0.034,0.263]              | 1.068 [0.641,1.314] | 0.0000    | 2.27      | 0.976       | 6.17       | 0.880 |
|                                           | <b>Posterior</b>      | 0.069 [-0.064,0.427]              | 1.223 [0.708,1.684] | 0.0000    | 1.99      | 0.982       | 5.27       | 0.913 |
|                                           | <b>Post. FW</b>       | 0.155 [-0.041,0.478]              | 1.002 [0.594,1.254] | 0.0001    | 1.27      | 0.952       | 4.86       | 0.909 |
| <b>Hybrid Strain Index</b>                | -0.100 [-0.445,0.180] | -1.893 [-3.723,-1.261]            | 0.0000              | 3.94      | 1.000     | 5.72        | 0.907      |       |

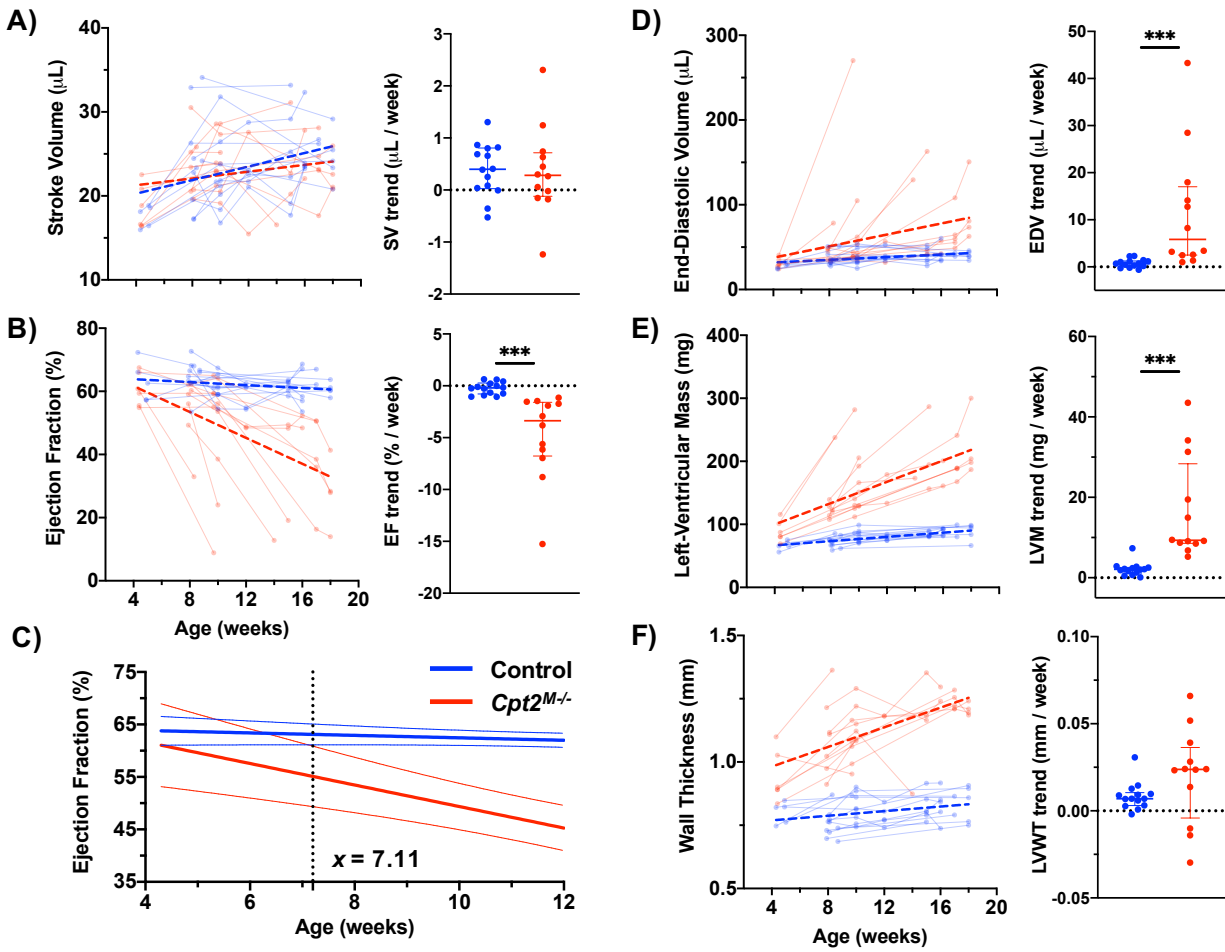


Figure 13. Global function and morphometric quantification of hypertrophy driven dysfunction through aging. Global function and anatomy metrics derived from endo- and epi-cardial surfaces at both end-diastole and peak-systole are investigated, including A) stroke volume (SV), B) ejection fraction (EF), D) end-diastolic volume (EDV), E) left-ventricular mass (LVM), and F) wall thickness (LVWT). On each scatter plot of longitudinally collected measurements, data from control mice are shown in blue and *Cpt2<sup>M-/-</sup>* mice are shown in red. Points from the same mouse are shown connected, and linear regression performed on across each cohort are visualized with thick dashed lines. To assess the earliest age in which metrics from a *Cpt2<sup>M-/-</sup>* mouse might deviate from the control population, the cumulative linear regression lines with 95% confidence intervals C) for ejection fraction were plotted and the age at which the confidence intervals no-longer overlap was identified (i.e., 7.11 weeks for EF). Additionally, dot plots are shown for each metric comparing slopes derived from mouse-specific linear regression, with horizontal lines designating median and interquartile ranges. Markers above each comparison plot indicate significance levels from non-parametric Mann-Whitney tests (\*\*\*)  $p < 0.001$ .

### 3.5.2 Regional Circumferential Strain

Locations at which circumferential strain ( $E_{\theta\theta}$ ) metrics were derived are shown in Figure 14A, alongside a representative strain curve with markings for peak strain, systolic strain rate, early diastolic strain rate, and late diastolic strain rate. Similar to those shown for global function metrics, longitudinal changes in peak  $E_{\theta\theta}$  at the base, mid-ventricle (Mid-LV), and apical regions are plotted in Figure 14B. Comparisons of peak  $E_{\theta\theta}$  trends show statistically significant differences between control and  $Cpt2^{M-/-}$  mice at each location, with p-values given in Table 2. Computed AUC values suggest that the greatest trend differences were observed at the base (AUC = 0.988), followed by Mid-LV (AUC = 0.929), and then apical regions (AUC = 0.839). Furthermore, while IQR ratios are similar between all three regions (i.e., 4.19, 4.52, and 5.22 respectively), trends at the base observed the earliest 95% CI intersection at 6.52 weeks old. When comparing metric values independent of age, peak  $E_{\theta\theta}$  at the base still showed the highest AUC (AUC = 0.861) compared to the Mid-LV (AUC = 0.730) and apical regions (AUC = 0.652).

Complementary to peak strain values, example longitudinal metric plots are shown in Figure 14C for systolic strain rate ( $\Delta E_{\theta\theta,sys.}$ ), early diastolic strain rate ( $\Delta E_{\theta\theta,early\ dia.}$ ), and late diastolic strain rate ( $\Delta E_{\theta\theta,late\ dia.}$ ) at the base of the heart. Supplemental Figure 1 provides longitudinal and trend comparison plots of all strain rate metrics at the base, mid-LV, and apical regions. Comparisons of individual trends, with values at the base shown in Figure 14C, indicate significant differences between control and  $Cpt2^{M-/-}$  mice for all  $\Delta E_{\theta\theta}$  metrics. Despite these significant differences, no  $\Delta E_{\theta\theta}$  metric had an AUC > 0.988, suggesting that peak  $E_{\theta\theta}$  at the base still demonstrates the best performance amongst circumferential strain metrics in differentiating trends from  $Cpt2^{M-/-}$  mice. Of note,  $\Delta E_{\theta\theta,lat\ dia.}$  at the base did not show any overlap in 95% CIs, suggesting that myocardial relaxation at the base may be compromised even prior to 4 weeks of age.

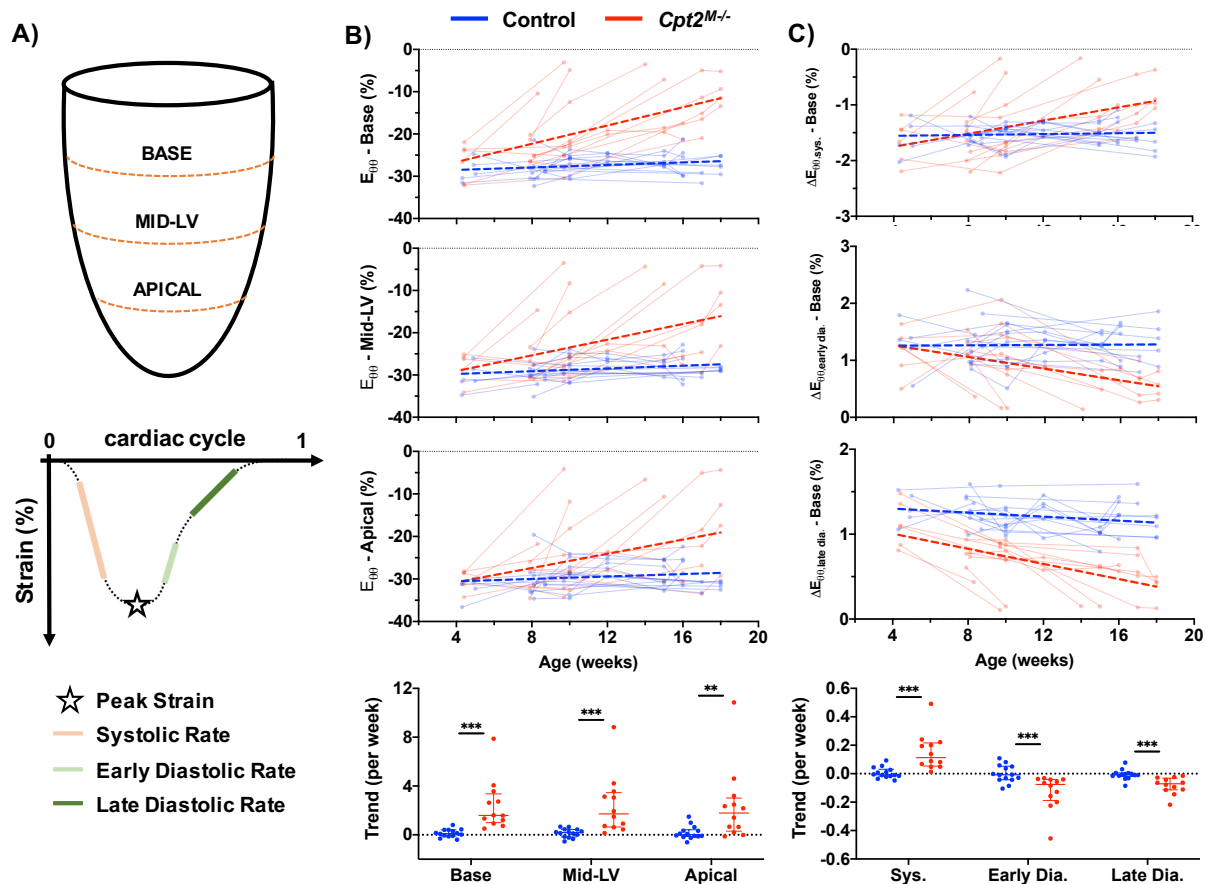


Figure 14. Regional circumferential strain measurements. Schematic (A) of where across the left ventricle circumferential strain was measured, and how peak strain ( $E_{\theta\theta}$ ), systolic strain rate ( $\Delta E_{\theta\theta,sys.}$ ), early diastolic strain rate ( $\Delta E_{\theta\theta,early dia.}$ ), and late diastolic strain rate ( $\Delta E_{\theta\theta,late dia.}$ ) were defined on a representative strain curve. Longitudinally measured peak circumferential strain (B) are shown for the base, mid-ventricle (Mid-LV), and apical slices, with data from control mice shown in blue and  $Cpt2^{M-/-}$  mice shown in red. Points from the same mouse are shown connected, and linear regression performed on across each cohort are visualized with thick dashed lines. Comparison plots of strain trends from each mouse and region are shown (bottom), with horizontal lines designating median and interquartile ranges. Significance markers above each comparison plot indicate p-value level from non-parametric Mann-Whitney tests ( $***p < 0.001$ ;  $**p < 0.01$ ). Additionally, example plots of longitudinal measurements, and trend comparisons, are provided (C) for systolic (sys.), early diastolic (early dia.), and late diastolic (late dia.) strain rates at the base of the heart.

### 3.5.3 Regional Longitudinal Strain

Locations at which circumferential strain ( $E_{LL}$ ) metrics were derived are schematically shown in Figure 15A. Longitudinal changes in peak  $E_{LL}$  along the posterior septum, posterior, posterior free-wall, anterior free-wall, anterior, and anterior septum regions are plotted in Figure 15B. Additionally, comparisons of peak  $E_{LL}$  trends show statistically significant differences between control and  $Cpt2^{M/-}$  mice at each location. Computed AUC values are comparable across all regions (AUC = 0.929-0.982), though greatest performance is observed along the posterior wall (AUC = 0.982). Computed 95% CI intersections show earlier separation for peak  $E_{LL}$  along the posterior wall at 5.27 weeks old, though the earliest intersection is seen at 4.58 weeks of age along the anterior free-wall. When comparing metric values independent of age, peak  $E_{LL}$  along the posterior wall still showed the highest AUC (AUC = 0.913) compared to all other regions (AUC = 0.821-0.909).

Longitudinal and trend comparison plots of systolic strain rate ( $\Delta E_{LL,sys.}$ ), early diastolic strain rate ( $\Delta E_{LL,early dia.}$ ), and late diastolic strain rate ( $\Delta E_{LL,late dia.}$ ) for each respective region are provided in Supplemental Figure 2. All  $\Delta E_{LL}$  trend differences were statistically significant, except for  $\Delta E_{LL,late dia.}$  along the posterior free-wall. The highest computed AUC value for  $\Delta E_{LL}$  trends was for  $\Delta E_{LL,sys.}$  along the posterior wall (AUC = 0.893), suggesting that peak  $E_{LL}$  along the posterior wall still demonstrates the best performance in differentiating trends from  $Cpt2^{M/-}$  mice amongst all longitudinal strain metrics. Of note,  $\Delta E_{LL,late dia.}$  along the anterior free-wall, posterior wall, and posterior free-wall did not show any overlap in 95% CIs, suggesting that similar to findings with  $\Delta E_{\theta\theta,lat dia.}$ , myocardial relaxation along the entire free-wall may be compromised even prior to 4 weeks of age.

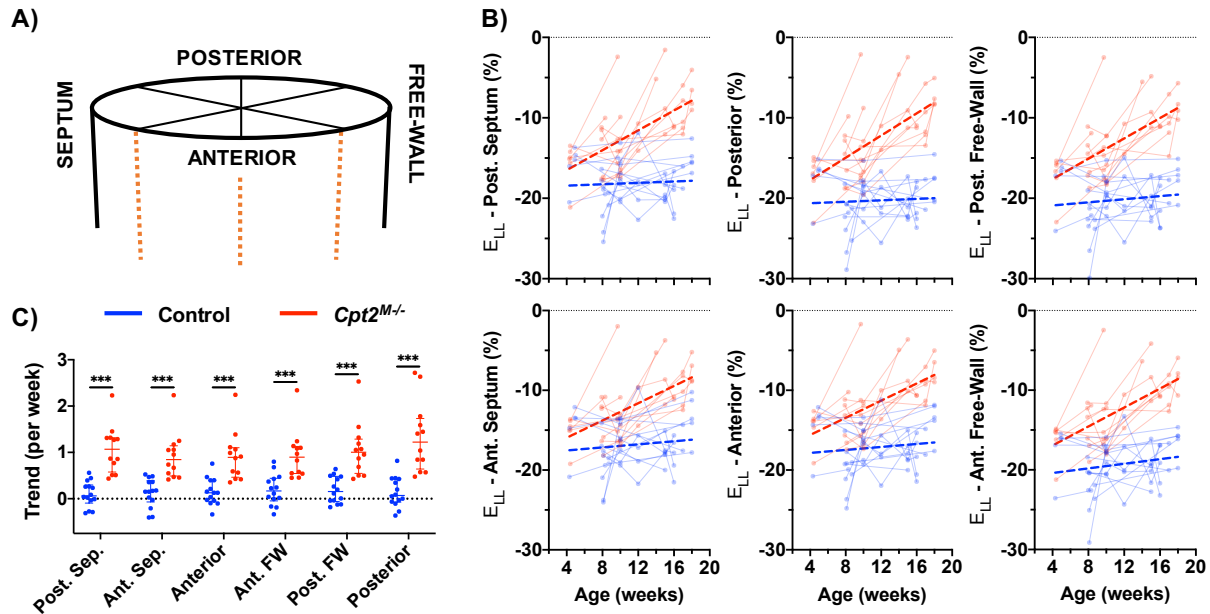


Figure 15. Regional longitudinal strain measurements. Schematic (A) localizing the area from which the left ventricle longitudinal strain ( $E_{LL}$ ) was measured. Peak longitudinal strain measured across time (B) are shown for rotations around the central z-axis corresponding to the posterior septum (Post. Sep.), posterior, posterior free-wall (Post. FW), anterior free-wall (Ant. FW), anterior, and anterior septum (Ant. Sep.) regions of the heart. Data from control mice shown in blue and  $Cpt2^{M-/-}$  mice shown in red. Points from the same mouse are shown connected, and linear regression performed on across each cohort are visualized with thick dashed lines. Comparison plots (C) of strain trends from each mouse and region are shown (bottom), with horizontal lines designating median and interquartile ranges. Significance markers above each comparison plot indicate p-value level from non-parametric Mann-Whitney tests ( $***p < 0.001$ ).

### 3.5.4 Hybrid Strain Index

Plotting peak posterior wall  $E_{LL}$  values along the against peak base  $E_{\theta\theta}$  values, as shown in Figure 16A, we can visualize the potential utility of using both metrics simultaneously to differentiate data from control and  $Cpt2^{M-/-}$  mice. Taking the L2 norm of these two values – effectively the distance from (0,0) to any given point – we compute the proposed Hybrid Strain Index (HSI). Longitudinal plots of HSI values and associated comparison of HSI trends are provided in Figure 16B, demonstrating a significant difference in trends between control and  $Cpt2^{M-/-}$  mice ( $p < 0.0001$ ).

Comparing the relative utility of all computed metrics in differentiating disease progression in  $Cpt2^{M-/-}$  mice against natural aging in control mice, Figure 16C shows trend IQR ratios plotted against AUC values. Axes are zoomed to show metrics for which  $AUC > 0.97$  and  $IQR < 6$ , respectively. Not only does HSI have the highest achievable AUC value ( $AUC = 1.00$ ), but it has a lower IQR ratio (3.94) than EF ( $AUC = 1.00$ ; IQR Ratio = 5.15) and peak base  $E_{\theta\theta}$  ( $AUC = 0.988$ ; IQR Ratio = 4.19). While lower IQR ratios are observed in peak  $E_{LL}$  along the posterior wall (1.99) and posterior septum (2.27), neither of these metrics show trend AUC values  $> 0.985$ . Figure 16D further highlights the age-independent utility of HSI by plotting 95% confidence interval intersections against metric AUC values.

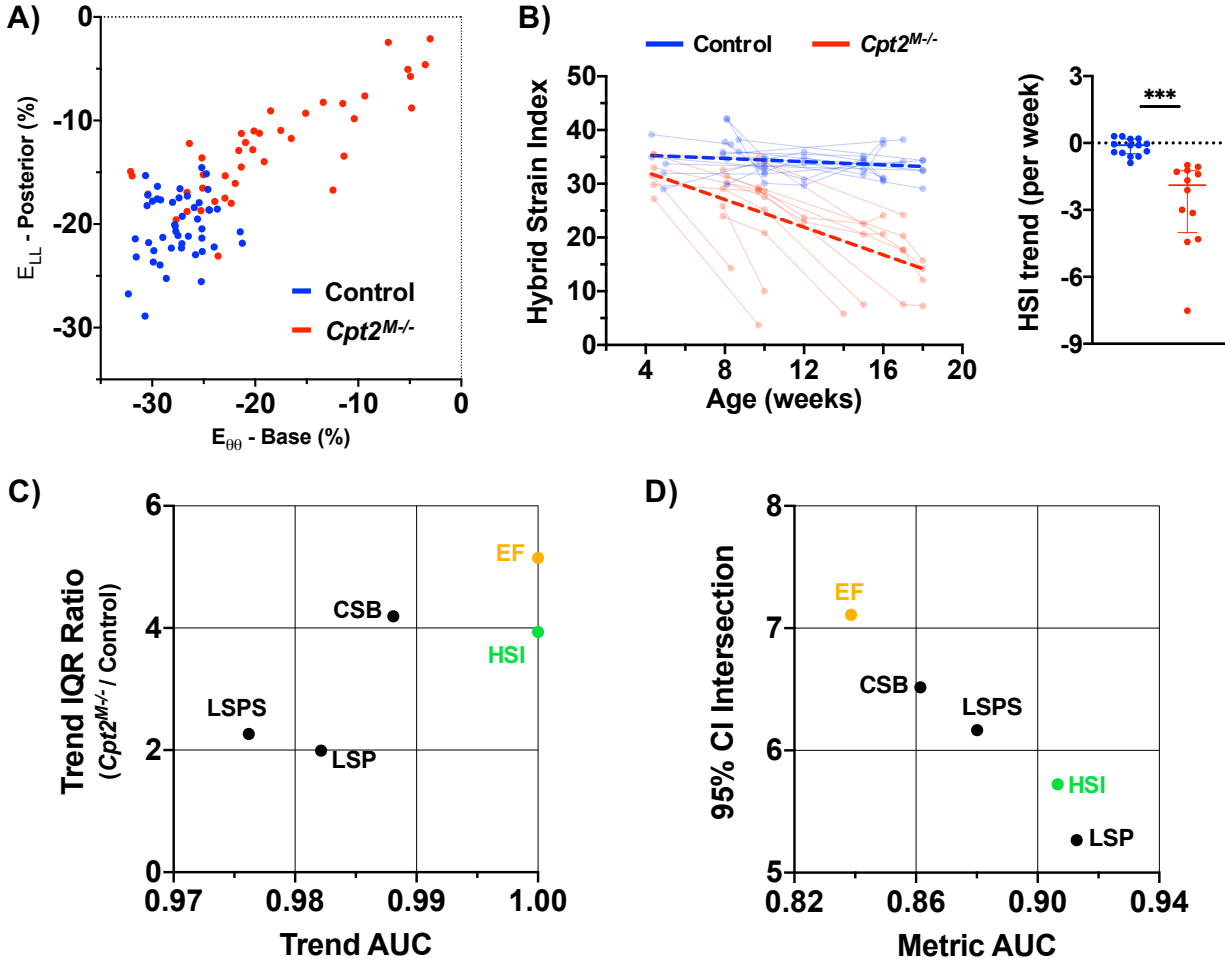


Figure 16. Hybrid Strain Index (HSI). Scatter plot (A) of the basal peak circumferential strain ( $E_{\theta\theta}$ ) value against posterior peak longitudinal strain ( $E_{LL}$ ) value for each 4DUS dataset, with data from control mice shown in blue and  $Cpt2^{M-/-}$  mice shown in red, visualizes the relationship between the two components incorporated into the HSI metric. Similar to those shown for circumferential and longitudinal strain, HSI measurements across time (B) are overlaid with cumulative linear regression results as thick dashed lines, as well as a comparison plot of HSI trends for individual mice. Significance markers indicate  $p$ -value level from non-parametric Mann-Whitney tests ( $***p < 0.001$ ). Demonstrating of the use of HSI in better characterizing disease progression, a scatter plot (C) of AUC values from ROC analysis against the ratio of trend standard deviations is provided, with HSI (green) providing the maximum area-under-curve (AUC) value alongside ejection fraction (EF; orange), yet with a lower interquartile range (IQR) ratio. Other shown metrics include: left-ventricular mass (LVM), peak circumferential strain at the base (CSB), and peak longitudinal strain at the posterior wall (LSP), anterior septum (LSAS), and posterior septum (LSPS). Metric utility is further explored by plotting 95% confidence interval intersections against age-independent metric AUC values (D), demonstrating with a higher AUC and earlier intersection that HSI could also be a more sensitive diagnostic marker of disease than ejection fraction.

### 3.6 Discussion

In this study we demonstrate how high-frequency 4DUS and derived metrics can be used to comprehensively study cardiac dysfunction progression in a murine model of hypertrophic cardiomyopathy (HCM). We specifically outline a standardized procedure for analysis of left-ventricular 4DUS data. This approach was taken to try and mitigate noted issues in reproducibility during standard echocardiographic data acquisition due to physical manipulation of the ultrasound probe [156-158]. This is accomplished by leveraging the relatively high spatial resolution of 4DUS to allow post-acquisition alignment of data to a standard set of axes, based on landmarks common to left-ventricular anatomy. Following reorientation, tracking of base and apex motion along the central z-axis allows us to compensate for the longitudinal contraction of the heart when extracting short-axis views across the cardiac cycle, effectively minimizing effects of through-plane motion common to cardiac imaging. Finally, the proposed 24-point grid structure from which endo- and epi-cardial 4D meshes are interpolated provides a uniformly distributed subset of spatial locations around the left-ventricle, which also simplifies wall motion tracking to a single axis (i.e., radius between each point and the center z-axis).

Applying these methods to the *Cpt2<sup>M/-</sup>* mouse model, measurements of LV morphometry suggest that hallmarks of HCM, namely LV mass and wall thickness are significantly increased even before the earliest imaging time-points of 4 weeks old. Observed significant increases in end-diastolic volume and decreases in EF provide additional evidence that *Cpt2<sup>M/-</sup>* mice exhibit HCM hallmarks of progressive LV chamber dilatation and cardiac dysfunction leading to heart failure, respectively. This is further supported by the fact that six of the twelve *Cpt2<sup>M/-</sup>* mice (50%) died premature to the planned final time-point. Predicting mouse survival is not possible without establishing cardiac parameters that are directly related to the progression and severity of the cardiomyopathy. Hence, the presentation of variable rates of disease progression in this *Cpt2<sup>M/-</sup>* model provided us with the power to correlate imaging data to the progression towards heart failure. This approach provides insights into highly predictive correlates with the potential for use in both research and clinical applications.

Looking to better understand regional drivers of cardiac dysfunction, we investigated circumferential and longitudinal strain metrics from select regions around the heart. As recent literature has pointed to regional strain being a more sensitive metric to cardiac dysfunction than EF [151], we focused here on identifying which regions and strain metrics that were most sensitive

to disease progression. In these regards, peak  $E_{\theta\theta}$  at the base and peak  $E_{LL}$  along the posterior wall were identified as two important regional metrics. While the identification of peak  $E_{LL}$  along the posterior wall may reflect the overall reduction of LV contractility, as this is where the highest magnitude  $E_{LL}$  values are observed around the LV, the disproportionately large reduction in peak  $E_{\theta\theta}$  at the base may hint at effects of diastolic dysfunction with its proximity to the mitral valve [159]. Future studies acquiring additional pulse wave Doppler data through the mitral valve could further investigate this hypothesis.

As an extension information provided by the outlined 4DUS analysis methods, our proposed novel Hybrid Strain Index (HSI) draws from the best performing circumferential and longitudinal strain metrics to provide a more sensitive marker of disease progression than all other computed function metrics. The relative performance of all metrics were quantified using both metric and trend AUC values, IQR ratio, and 95% CI intersection, from which HSI demonstrates the best overall utility in identifying *Cpt2<sup>M-/-</sup>* mice against controls. While both EF and HSI provide maximal trend AUC values, thus suggesting similar utility in describing disease progression, HSI provides both a higher metric AUC and earlier 95% CI intersection than EF, indicating that it might be more sensitive to mild cardiac dysfunction and would decrease prior to EF. This seems intuitive as HSI reflects the contractility of two orthogonal reference frames (i.e., circumferential and longitudinal) that together cover the extent of the LV, yet isolates the metric in each frame that demonstrates the greatest sensitivity to cardiac dysfunction. With this in mind, different variations of the HSI metric could be formulated that are specific to unique cardiomyopathies.

Finally, while the imaging timepoints of the mice in this study were inconsistent, a variety of ages, disease states, and follow-up scan timings are commonplace in the clinic. As numerous factors might influence the frequency by which patients have echocardiographic assessments, the focus on changes in measurements over several imaging sessions is more informative to potential declines in cardiac function than an isolated measurement. While further validation work is needed, our results suggest that in this paradigm HSI could be a complementary marker to help characterize cardiac dysfunction progression and disease progression. In particular, the use of HSI could prove useful in the characterization of heart failure with preserved ejection fraction (HFpEF) where a more sensitive marker to cardiac dysfunction could help in diagnosis and to better assess patient responses to subsequent treatment [160-162].

### **3.6.1 Limitations**

Despite the demonstrated promise in the proposed analysis and results, several limitations still exist. The use of ultrasound technology for cardiac imaging inherently presents issues with both shadowing artifacts from the ribcage and mirror artifacts from the surrounding lungs. Their impact can be mitigated during imaging with proper probe placement, and during 4DUS analysis by using multi-planar views to estimate borders through impacted regions. Secondly, the calculation of strain in both the circumferential and longitudinal frames is assumed to be uniform throughout the cardiac cycle. While this assumption allows the tracking of regional wall motion at any given grid point to be simplified to the radius of that point to the center z-axis, recent literature has suggested this assumption may not always be valid and might oversimplify more complex disease models, such as myocardial infarction where focal akinetic regions of the heart are observed [163, 164]. Finally, one component of cardiac kinematics that has not been addressed in this analysis is myocardial twist. While it is known that the rotation of the base and apex of the heart through the cardiac cycle can be impacted in various cardiomyopathies, the ability to quantify rotation and twist has not yet been integrated into the current analysis. Future work will be needed to both incorporate rotational information into the creation of LV 4D meshes and quantify its impact in various disease models.

### **3.7 Conclusion**

We demonstrate here for the first time the application of high-frequency 4DUS imaging to a murine model of hypertrophic cardiomyopathy. The proposed analysis provides a standardized approach to measure localized wall kinematics and simultaneously extract metrics of global cardiac function, LV morphometry, regional circumferential strain, and regional longitudinal strain from an interpolated 4D mesh of the endo- and epi-cardial boundaries. We further propose a Hybrid Strain Index (HSI), composed of peak circumferential strain at the base and longitudinal strain along the posterior wall, which provides greater utility to characterizing disease progression than all other extracted metrics. Future could be used to apply these methods to additional disease models and further validate the utility of metrics derived from the 4DUS imaging and strain mapping.

## 4. SPATIOTEMPORAL STRAIN MAPS OF DISEASE PROGRESSION IN NKX2-5 MODEL OF HYPERTROPHIC CARDIOMYOPATHY

In this section, we highlight an application of 4DUS imaging to study cardiac dysfunction progression in another murine model of hypertrophic cardiomyopathy (*Nkx2-5<sup>183P/+</sup>*). Similar to Chapter 3, we detail here a standardized procedure for analyzing 4DUS data that can simultaneously extract measurements of left-ventricular global function, morphometry, and regional strain. We further pose a paradigm for displaying the circumferential and longitudinal strain results as spatiotemporal maps, which can provide a more comprehensive visualization of cardiac function. The content presented in this chapter will be submitted for publication in *Cardiovascular Research* entitled “Kinematic Analysis of Murine Cardiac Hypertrophy Using High-Frequency Four-Dimensional Ultrasound”.

### 4.1 Introduction

Murine models play a critical role in uncovering the underlying mechanisms of cardiac disease and progression [5, 57]. These models are particularly useful in the study of congenital heart disease (CHD), where clinical manifestations often lead to early lethality. While recent advancements in corrective interventions for CHD malformations have led to more frequent patient survival into adulthood, suggesting maintenance of global heart function, further research is still needed to better understand on how specific genetic precursors of CHD alter regional cardiac function through aging. One factor of recent interest is the NKX2-5 gene, which has been identified as a homeobox transcription factor in cardiac precursors and is essential for early heart development and myocardial cell fate. Mutations in the human NKX2-5 gene have been associated with a diverse range of CHD and conduction defect (CD) phenotypes, including atrial and ventricular septal defects, atrioventricular conduction block, tetralogy of Fallot, hypoplastic left heart, transposition of the great arteries, dextrocardia, and valvular malformations.

Aiming to better understand the impact of NKX2-5 mutations on cardiac physiology, here we investigate a murine model with these mutations and propose novel analysis methods that might provide more comprehensive information into how regional ventricular function is altered. Absence of NKX2-5 in mice results in impaired cardiac growth and chamber formation, disrupted

gene regulatory network, and early embryonic lethality. Conditional deletion at postnatal stages has shown that NKX2-5 activity is also essential for maintenance of the cardiac conduction system. Preliminary work with these mice has demonstrated an early decrease in cardiomyocyte mitochondrial density and cellular respiration. This shift in metabolic capacity leads to an increased dependence on fatty acid oxidation [77], progressive concentric hypertrophy, and subsequent heart failure.

Complementary to mouse models of cardiac disease, high-frequency ultrasound has become an integral tool for quantifying global cardiac function *in vivo* (i.e., ejection fraction, stroke volume, etc.) [150]. More recent developments in high-frequency four-dimensional ultrasound (4DUS) have advanced this imaging technologies' capabilities even further to provide localized quantification of left ventricular (LV) kinematics, with higher spatiotemporal resolution than high-field cardiac cine-MRI [29, 30]. We propose here a novel analysis paradigm that not only standardizes the analysis of LV 4DUS data to quantify ventricular kinematics, but also creates novel visualizations of circumferential and longitudinal strain in the form of spatiotemporal maps.

## 4.2 Methods

### 4.2.1 Animal Models

Six C57BL/6J male mice with genetically induced cardiac hypertrophy (*Nkx2-5<sup>183P/+</sup>*) [77, 78, 165] and six littermate controls were used for this study. To identify both cross-sectional and longitudinal differences between *Nkx2-5<sup>183P/+</sup>* (i.e., mutant) and littermate control (i.e., wild-type) mice, imaging was performed at 8, 12, and 16 weeks old. Following imaging at 16 weeks old, all mice were euthanized, had saline perfused through the inferior vena cava to clear blood in the heart chambers, and then had their hearts excised, sectioned, and snap frozen for proteomics analysis. Each heart was sectioned into four pre-defined regions: basal free-wall, basal septum, apical free-wall, and apical septum. All animal experiments were approved by the Purdue Animal Care and Use Committee.

### 4.2.2 Ultrasound Acquisition

4DUS data was collected using a Vevo2100 high-frequency ultrasound system (FUJIFILM VisualSonics Inc., Toronto, Ontario, Canada) with a 40 MHz center frequency transducer (MS550D) attached to a translating linear step motor. In preparation for imaging, mice were anesthetized using a low-flow vaporizer (SomnoSuite, Kent Scientific, Torrington, CT, USA) with ~2.5% isoflurane at 250 ml/min [139], secured to a heated stage with gold-plated electrodes that collected cardiorespiratory signals, and had ventral thorax hair removed using depilatory cream. Serial short-axis ECG-gated Kilohertz Visualization (EKV) cine loops were acquired starting inferior to the left-ventricular apex and ending at the aortic arch, stepping approximately 200  $\mu\text{m}$  between slices. 4DUS data was then compiled in MATLAB (MathWorks Inc.) using the spatial position of each slice and gating by associated cardiac and respiratory signals [29, 30].

### 4.2.3 Boundary Definition and Kinematics Analysis

A custom MATLAB toolbox was developed to analyze each 4DUS dataset using the following standardized steps (Figure 17):

- A. Reorienting the input spatial axes to standard axes (i.e., z-axis = the apex-to-base line, y-axis = the anterior to posterior walls line, and x-axis = the free-wall to septum line);
- B. Tracking z-axis positions of the apex and base across the cardiac cycle, from which four parallel short-axis slices (i.e., 25, 50, 75, and 100% to the base) are extracted;
- C. Defining a grid of endocardial and epicardial boundary points located at each relative short-axis slice, and uniformly spaced across six rotations around the kinematic axis (i.e., 30, 90, 150, 210, 270, and 330° from the free-wall oriented axis), from which local wall motion is tracked across the cardiac cycle; and
- D. Using the tracked grid positions at each time-point to interpolate a final 4D grid of each boundary, sampled spatially at 60 uniform rotations around and 60 uniformly spaced slices down the left-ventricle, and temporally at 60 uniformly distributed points across the cardiac cycle.

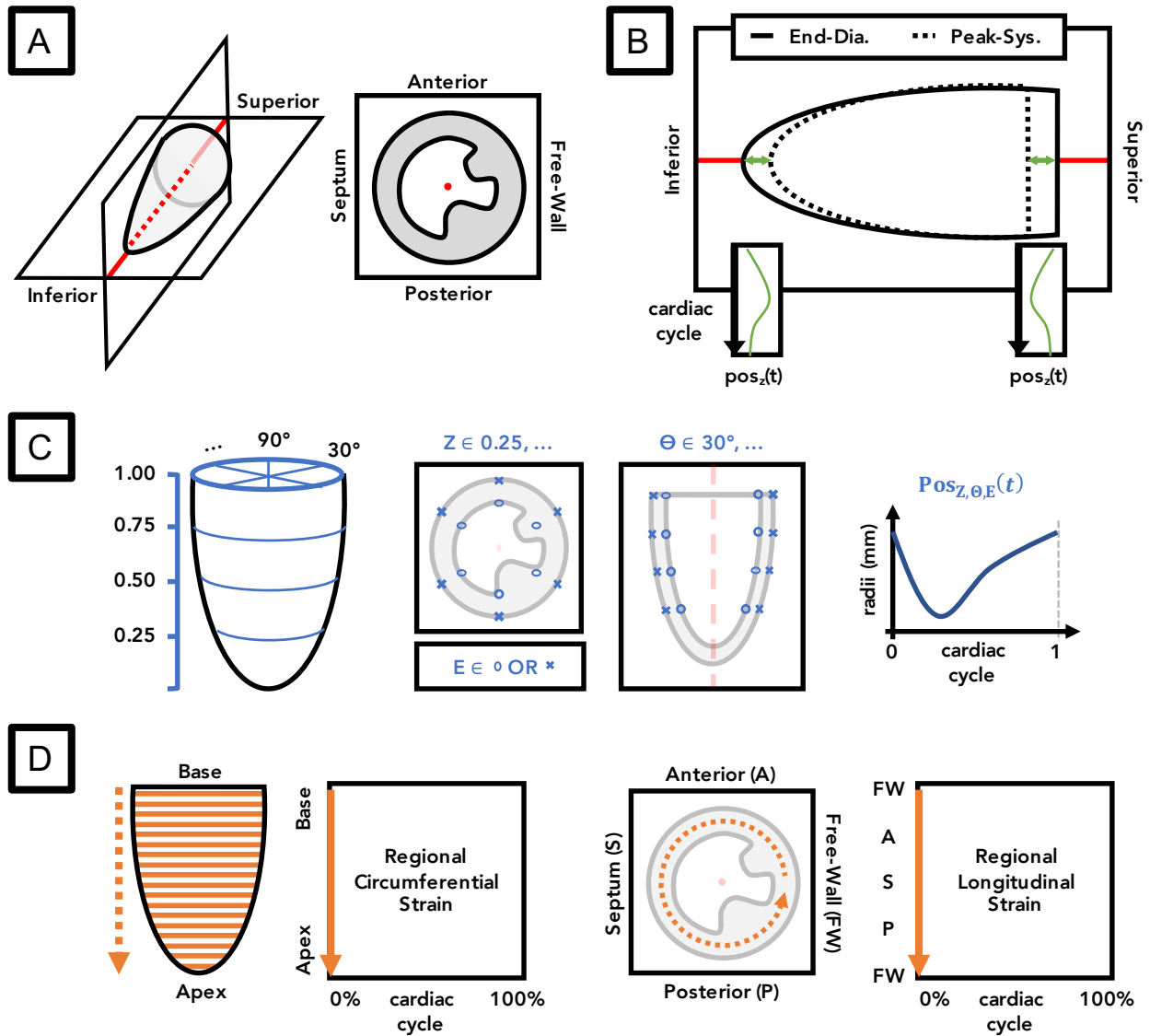


Figure 17. Schematic for standardized 4DUS analysis procedure. The outlined steps include: A) reorientation of data to defined axes, B) tracking z-axis position ( $pos_z$ ) of the left-ventricular base and apex across relative time ( $t$ ) in the cardiac cycle, C) defining and tracking local wall motion ( $pos_{z,\theta,E}$ ) at a grid of endocardial ( $E=0$ ) and epicardial ( $E=x$ ) points equally spaced across four short-axis slices ( $Z$ ) and six rotations ( $\theta$ ) around the left ventricle, and D) quantification and plotting of regional kinematics as circumferential and longitudinal spatiotemporal strain maps. Red axes denote the same central “z-axis” that the data is oriented to in the first step.

Similar to those reported in literature [15, 153, 154], measurements of global cardiac function (e.g., ejection fraction, stroke volume, and left-ventricular mass) and regional myocardial kinematics (i.e., circumferential and longitudinal strain) were extracted from the final 4D left-ventricular meshes. Regarding circumferential strain ( $E_{\theta\theta}$ ), we used the Green-Lagrange strain tensor definition assuming circular cross-sections [155]:

$$E_{\theta\theta}(t) = \frac{1}{2} \left( \left( \frac{C(t)}{C_D} \right)^2 - 1 \right) \quad [10]$$

where  $C$  represents the relative circumference at time  $t$  in the cardiac cycle;  $C_D$  is the circumference at end-diastole (i.e.,  $t=0$ ). Curves of  $E_{\theta\theta}$  were derived for slices corresponding to the basal, mid-ventricular, and apical regions of the left ventricle, from which peak-strain, systolic strain rate, and diastolic strain rate can be extracted.

Complementary measurements of longitudinal ( $E_{LL}$ ) strain can be calculated using the linear strain approximation:

$$E_{LL}(t) = \frac{L(t) - L_D}{L_D} \quad [11]$$

where  $L$  represents the cross-sectional length at time  $t$  in the cardiac cycle, and  $L_D$  is the respective length at end-diastole.  $E_{LL}$  was derived at each of the six rotations around the central z-axis (i.e., 30, 90, 150, 210, 270, and 330° from the left free-wall). Furthermore, peak-strain, systolic strain rate, and diastolic strain rate can also be extracted for each of these strain curves.

#### 4.2.4 Spatiotemporal Strain Mapping

Since each 4D mesh is defined by equally sized matrices of spatiotemporal boundary information, changes in mesh morphology across the cardiac cycle can be systematically quantified and compiled into spatiotemporal maps. Herein, we describe two such maps that are based on the commonly reported circumferential and longitudinal strain metrics, illustrated in Figure 17D. Spatiotemporal maps of circumferential strain effectively visualize strain curves computed at each short-axis slice down the 4D LV mesh, described using a modified Equation 10:

$$E_{\theta\theta}(z, t) = \frac{1}{2} \left( \left( \frac{C(z, t)}{C_D(z)} \right)^2 - 1 \right) \quad [12]$$

where  $C$  represents the relative circumference at slice  $z$  and time  $t$  in the cardiac cycle;  $C_D$  is the circumference at end-diastole (i.e.,  $t=0$ ). Comparable maps of longitudinal strain were derived using the linear small strain approximation at each rotation around the center axis:

$$E_{LL}(\theta, t) = \frac{L(\theta, t) - L_D(\theta)}{L_D(\theta)} \quad [13]$$

where  $L$  represents the apex-to-base length along the boundary at rotation  $\theta$  and time  $t$  in the cardiac cycle;  $L_D$  is the respective length at end-diastole.

#### **4.2.5 Cross-Sectional and Longitudinal Assessments.**

Since spatiotemporal strain map matrix sizes were standardized during analysis using shape-preserving interpolations (i.e., 60 spatial locations by 60 time-points across the normalized cardiac cycle), resultant maps can be stacked by cohort and age, allowing for pixelwise statistical comparisons. Demonstrated in Figure 18 using age and cohort averaged circumferential strain maps, cross-sectional differences between cohorts are quantified using area under the curve (AUC) values for pixelwise receiver operating characteristics (ROC) curves. Additionally, aging based trends are calculated by averaging slopes from linear regression run pixelwise on each animal's respective data from 8, 12, and 16 weeks old. Trend maps are shown as percent strain per month for both circumferential and longitudinal strain maps.

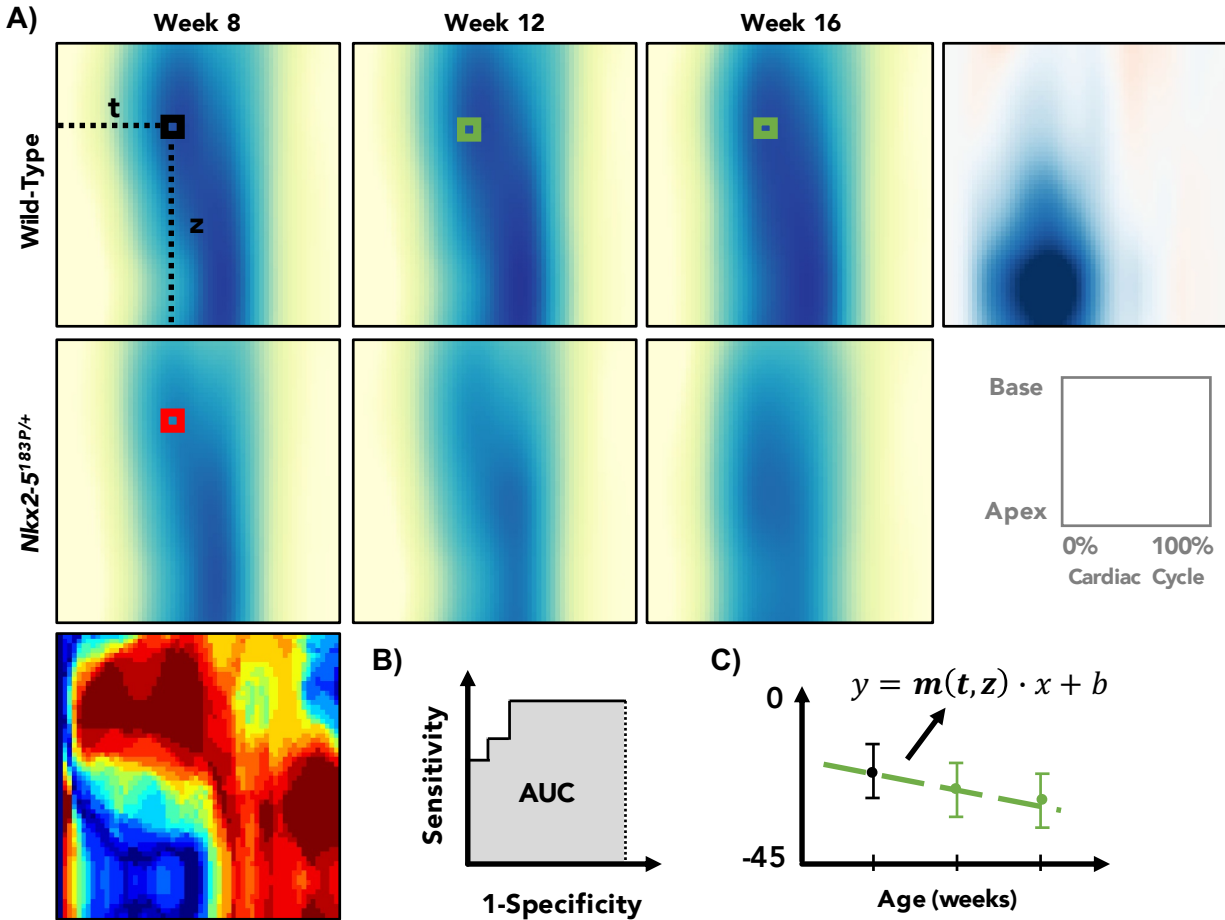


Figure 18. Visualization of pixelwise cross-sectional and aging based trend analysis, demonstrated using (A) circumferential spatiotemporal strain maps. Dotted black lines highlight both the time within the cardiac cycle (t) and location across the left-ventricle (z) for which data are isolated for analysis, stratified by both cohort and age. Cross-sectional analysis is performed by calculating (B) area under the curve (AUC) values from receiver operating characteristics (ROC) curves. Aging based trend analysis is performed with (C) linear regression through data from 8, 12, and 16 weeks old, displayed as percent strain per month.

#### 4.2.6 Statistics

All statistical tests were performed in Prism (GraphPad Software, San Diego, CA). Cohort differences in global function, morphometry, and regional strain metrics at each imaged age were investigated using a two-way repeated measures ANOVA with post-hoc Bonferroni's multiple comparisons test;  $p < 0.05$  was considered statistically significant. All cohort-specific metric summaries are reported as mean (standard deviation).

## 4.3 Results and Discussion

### 4.3.1 Global Function and Regional Strain

Comparisons of global function and morphometry are plotted in Figure 19A, showing ejection fraction and LV mass significantly different between groups at weeks 8 (EF  $p = 0.0015$ ; LVM  $p = 0.0018$ ), 12 (EF  $p = 0.0022$ ; LVM  $p = 0.0081$ ), and 16 (EF  $p = 0.0115$ ; LVM  $p = 0.0022$ ). In contrast, no significant differences were found at any week for end-diastolic volume and stroke volume. Comparisons of peak circumferential strain at the base, mid-ventricular, and apical regions are plotted in Figure 19B, with all three regions showing significant differences between cohorts at weeks 12 (base  $p = 0.0018$ ; mid-LV  $p = 0.0060$ ; apical  $p = 0.0043$ ) and 16 (base  $p = 0.0045$ ; mid-LV  $p = 0.0104$ ; apical  $p = 0.0083$ ). At week 8, significant differences were only found at the base ( $p = 0.0015$ ) and mid-LV ( $p = 0.0105$ ). Interestingly, comparisons of longitudinal strain metrics at all six rotations around the LV show no significant differences between groups. A summary of all computed global function and morphometry, as well as regional circumferential and longitudinal strain, metrics compared at weeks 8, 12, and 16 are provided in Supplemental Table 2.

Noting that the circumferential reference frame seems to be the more sensitive to the induced hypertrophic cardiomyopathy than the longitudinal frame, and the apical region of the heart does not show a significant difference between groups at week 8, we further explored the relationship between the base and apical regions throughout aging. Figure 19C plots the peak circumferential strain at the base against the apical strain, with data at weeks 8, 12, and 16 shown with increasing levels of transparency. While the ratio between the two regions seem similar, there is a notable separation between each cohorts' data cluster. Additionally, while the control data seems to remain in the same region across aging, there is a shift to lower magnitude apical strain values in the *Nkx2-5<sup>183/+</sup>* cohort. Future work may leverage this approach of clustering base versus apical strain information to better characterize the cardiac disease progression against control data.

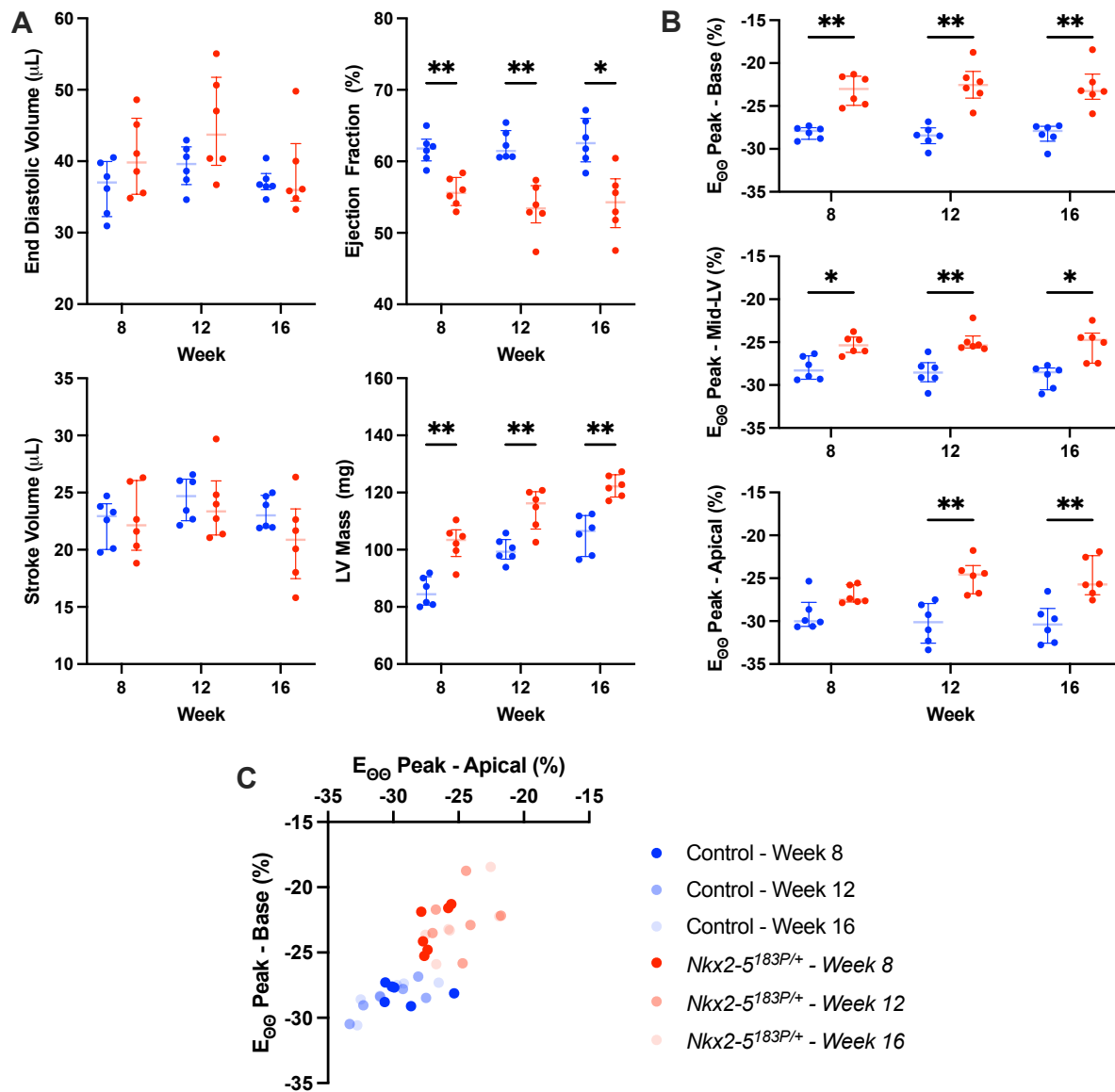


Figure 19. Comparisons of global function, morphometry, and regional circumferential strain. Global function (i.e., end-diastolic volume, stroke volume, and ejection fraction) and morphometry (i.e., left-ventricular mass) measurements (A) are shown for both control (blue) and  $Nkx2-5^{183/+}$  (red) mice, with significance markers for cross-sectional comparisons. Peak circumferential strain  $E_{\theta\theta}$  measurements (B) are shown for the base, mid-ventricle (Mid-LV), and apical slices, with comparable statistical comparison markers. Significance markers above each comparison plot indicate p-value level from two-way ANOVA with post-hoc Bonferroni's multiple comparisons test (\*\* $p < 0.01$ ; \* $p < 0.05$ ). Additionally, a scatter plot of peak  $E_{\theta\theta}$  at the base versus apical regions (C) with data from weeks 8, 12, and 16 shown with increasing levels of transparency, demonstrate the shift in the base to apical region relationship throughout aging in each cohort.

### 4.3.2 Spatiotemporal Strain Mapping

Figure 20 highlights circumferential strain maps for each cohort across weeks 8, 12, and 16. At the earliest age imaged, circumferential strain magnitude deficits in the  $Nkx2-5^{183P/+}$  cohort were primarily observed at the base of the heart during systole, suggesting weakened contractility near the mitral and aortic valves. As both cohorts aged to week 16, a disproportionately lower magnitude circumferential strain was observed apically for the  $Nkx2-5^{183P/+}$  cohort. Interestingly, both cohorts showed a decrease in strain magnitude in the basal region through aging, suggesting a natural shift of systolic contractility towards the apex over time. A visualization of all circumferential strain maps that were used to perform this analysis are provided in Supplemental Figure 3.

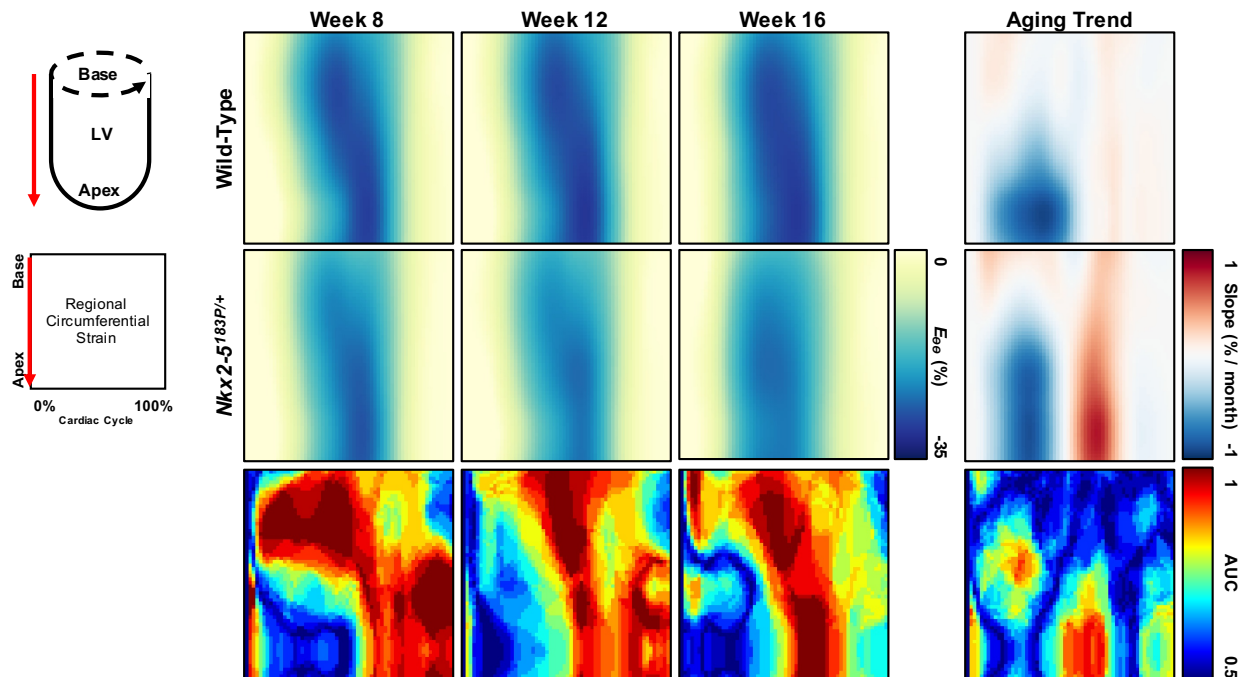


Figure 20. Colormaps of circumferential strain profiles averaged at each time-point for both wild-type and  $Nkx$  cohorts. Plots as shown with relative short-axis slice locations on the y-axis and normalized time from R-peak through a cardiac cycle on the x-axis (bottom right diagram). For each time-point (first three columns), pixelwise z-scores are computed for the  $Nkx$  cohort against the wild-type cohort distribution; averaged z-score colormaps are then displayed above (bottom row). Additionally, using linear regression, the pixel-wise slope across time (last column) is computed for each cohort (last column), normalized to a per-month basis.

Figure 21 highlights longitudinal strain maps for each cohort across weeks 8, 12, and 16. In both cohorts, the posterior free-wall observes higher magnitude longitudinal strain throughout systole. Although unlike circumferential strain, negligible differences in the AUC maps were observed at week 8, suggesting that circumferential systolic contractility may be more sensitive to the early development of hypertrophy. By week 16, the distribution of longitudinal strain in the *Nkx2-5<sup>183P/+</sup>* cohort show more uniformity around the ventricle, and the duration of the systolic contraction wave appears shortened. Interestingly, both cohorts show a trend of increased early systolic longitudinal strain, suggesting a more rapid systolic contraction around the entire myocardium. A visualization of all longitudinal strain maps that were used to perform this analysis are provided in Supplemental Figure 4.

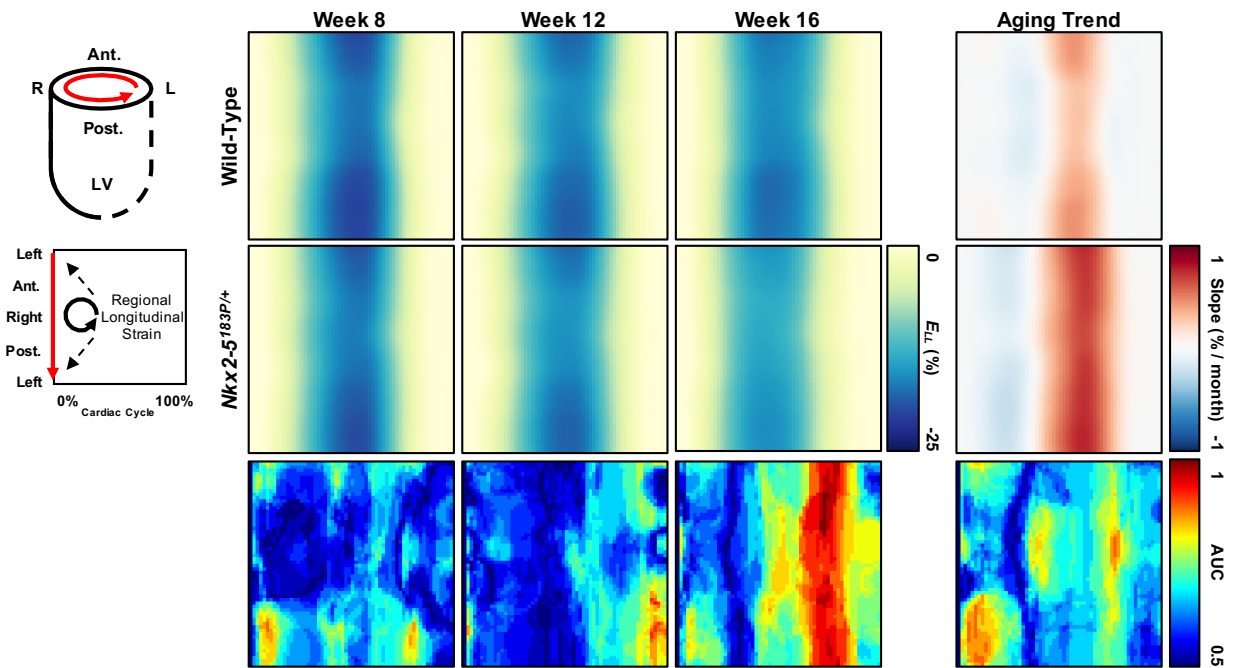


Figure 21. Colormaps of regional longitudinal strain profiles averaged at each time-point for both wild-type and *Nkx* cohorts. Plots as shown with relative rotations around kinematic axis on the y-axis and normalized time from R-peak through a cardiac cycle on the x-axis (bottom right diagram). For each time-point (first three columns), pixelwise z-scores are computed for the *Nkx* cohort against the wild-type cohort distribution; averaged z-score colormaps are then displayed above (bottom row). Additionally, using linear regression, the pixel-wise slope across time (last column) is computed for each cohort (last column), normalized to a per-month basis.

## 4.4 Conclusions

We demonstrate here the ability to use 4DUS imaging to produce spatiotemporal maps of both circumferential and longitudinal strain, from which we can quantify changes in cardiac kinematics that correlate with age and phenotype. In this study, we identified when and where kinematic patterns deviate in a genetic model of cardiac hypertrophy (*Nkx2-5<sup>183P/+</sup>*). Our findings suggest that inhibited cardiomyocyte energy handling induced by the *Nkx2-5<sup>183P/+</sup>* mutation not only induces a hypertrophic myocardium [166], but also alters the systolic contraction profile. As research exploring regionally specific strain in mice using 4DUS technology remains limited [152], these findings may provide a framework for how 4DUS can be leveraged to provide more comprehensive characterizations of cardiac function and disease.

Not only will these metrics provide a deeper understanding of the regional cardiac dynamics, but will also help researchers improve techniques for multi-array echocardiography analysis [19-22]. Furthermore, researchers who already use small animal ultrasound systems in their studies could immediately benefit from our work as our acquisition procedure and proposed analysis toolbox use commercially available equipment (i.e. FUJIFILM VisualSonics Vevo2100/3100 systems; MATLAB). Finally, future work will look to combine our regional strain information with proteomics analysis performed on tissue excised from those specific regions in order to better quantify the relationship between cardiac function and the makeup of the underlying myocardial tissue. We hope that with widespread adoption of our methods, we will enable research groups throughout our field to expand the breadth of knowledge obtained with ultrasound imaging in murine models of cardiac disease.

## 5. MACHINE LEARNING APPLICATIONS TO 4DUS KINEMATICS ANALYSIS

In this section we detail, to our knowledge, the first application of machine learning to the problem of automatic boundary detection to murine four-dimensional ultrasound (4DUS) data. We propose three models that are constructed such that short-axis images are analyzed individually (Model 1), parallel slices are incorporated simultaneously (Model 2), and predictions are assisted by a single user-input position (Model 3). We built our models based on ground-truth data drawn from 136 4DUS datasets, comprised of mice with healthy and hypertrophic hearts, each having 30-40 time-frames across a representative cardiac cycle. Our results imply an increase in prediction performance from Model 1 to 3, and we discuss why certain regions of the heart might experience increased errors. Furthermore, various metrics of cardiac function are computed from model predictions alone and we compared them to ground-truth. The content presented in this chapter was adapted from the work recently accepted in *Applied Sciences* entitled “Machine Learning Driven Contouring of High-Frequency Four-Dimensional Cardiac Ultrasound Data”; made available under a Creative Commons Attribution License through the following link: TBD.

### 5.1 Abstract

Automatic boundary detection of 4D ultrasound (4DUS) cardiac data is a promising yet challenging application at the intersection of machine learning and medicine. Using recently developed murine 4DUS cardiac imaging data, we demonstrate here a set of three machine learning models that predict left ventricular wall kinematics along both the endo- and epi-cardial boundaries. Each model is fundamentally built on three key features: 1) the projection of raw US data to a lower dimensional subspace, 2) a smoothing spline basis across time, and 3) a strategic parameterization of the left ventricular boundaries. Model 1 is constructed such that boundary predictions are based on individual short-axis images, regardless of their relative position in the ventricle. Model 2 simultaneously incorporates parallel short-axis image data into its predictions. Model 3 builds on the multi-slice approach of model 2, but assists predictions with a single ground-truth position at end-diastole. To assess the performance of each model, Monte Carlo cross validation was used to assess the performance of each model on unseen data. For predicting the

radial distance of the endocardium, models 1, 2, and 3 yielded average  $R^2$  values of 0.41, 0.49, and 0.71, respectively. Monte Carlo simulations of the endocardial wall showed significantly closer predictions when using model 2 versus model 1 at a rate of 48.67%, and using model 3 versus model 2 at a rate of 83.50%. These findings suggest that a machine learning approach where multi-slice data is simultaneously used as input and predictions are aided by a single user input yields the most robust performance. Subsequently, we explore how metrics of cardiac kinematics compare between ground-truth contours and predicted boundaries. We observed negligible deviations from ground-truth when using predicted boundaries alone, except in the case of early diastolic strain rate, providing confidence for the use of such machine learning models for rapid and reliable assessments of murine cardiac function. To our knowledge, this is the first application of machine learning to murine left ventricular 4DUS data. Future work will be needed to strengthen both model performance and applicability to different cardiac disease models.

## 5.2 Introduction

As heart disease remains the number one cause of death in the United States [33], echocardiography remains an integral tool to the proper diagnosis and prognosis of abnormal cardiac function. Furthermore, the development of murine models of cardiac disease have provided researchers a strong foundation to further our understanding of pathological hallmarks and how specific genetic and/or environmental factors might drive progression [5-9]. To bridge the gap between imaging technology and murine disease models, high-frequency ultrasound uses MHz frequency ultrasonic waves to acquire images of small structures (e.g. mouse left ventricle with a thickness of  $\sim 1$ mm) that are rapidly moving (e.g. mouse heart rate is  $\sim 500$ -600 bpm), thus too difficult to be adequately viewed using clinical ultrasound systems. Recent advancements in high-frequency ultrasound technologies have also introduced a collection of four-dimensional ultrasound (4DUS) approaches, allowing for more thorough analyses of cardiac motion beyond global metrics based on idealized geometries (i.e., ejection fraction, stroke volume), similar to that commonly reported with clinical cine-magnetic resonance imaging (cine-MRI) [29, 30, 152].

In tandem with the advancement of ultrasound imaging technology, integrations of machine learning and artificial intelligence algorithms -- particularly deep neural nets -- have shown promise in rapidly and robustly characterizing cardiac kinematics and ultrasound data in general [167-174]. While machine learning has demonstrated notable successes in ventricle

segmentation on 4D cardiac MRI data [175-177], epicardial fat segmentation in Computed Tomography (CT) data [178, 179], and even boundary detection in clinical 2DUS echocardiography data [10], applications to murine 4DUS data remain limited [169]. This is in part due to unique challenges presented by 4DUS data. Most notably, cardiac US images in mice show lower image contrast in combination with large amounts of speckle noise (e.g., see Figure 25). Furthermore, as the probe typically covers half of the entire ventral thorax, these artifacts can even render manual segmentation difficult. Finally, 4DUS data in general suffers from high dimensionality; even 3DUS segmentation is considered a difficult problem given current tools [10]. The high dimensionality in combination with the relatively small sample sizes commonly seen in medical applications, of which our dataset is no exception, presents even further challenges.

Here we develop a machine learning model to contour 4DUS data acquired from healthy and diseased (i.e., hypertrophic cardiomyopathy) mice. To our knowledge, this is the first publication of machine learning applied to murine cardiac 4DUS data. While our model is described in detail below, it contains three fundamental components: 1) a low dimensional representation of the raw US data, 2) a basis expansion of time to incorporate the regularity in epicardial movement throughout the cardiac cycle, and 3) the requirement that the model need only predict output values at preselected anchor points using interpolating cubic splines to form the final output structure.

The following section “Materials and Methods” outlines the procedures followed to acquire the data used in training our models, details each model’s composition, and describes how we test each model’s predictive accuracy. The “Results and Discussion” section then demonstrates our quantitative model performance tests’ results and provides context regarding broader applicability and limitations. Finally, we discuss other modelling approaches for future work and potential clinical translatability.

## **5.3 Materials and Methods**

### **5.3.1 Ultrasound Data**

Imaging was performed using a Vevo3100 high-frequency ultrasound system (FUJIFILM VisualSonics Inc.) with a 40 MHz center frequency transducer (MX550D) and a translating linear step motor. In preparation for imaging, mice were anesthetized using approximately 1.5-2.0%

isoflurane, secured supine on a heated stage with gold-plated electrodes that collected cardiac and respiratory signals, and had hair removed from the ventral surface via a depilatory cream. Each 4DUS dataset was acquired by translating through short-axis slices from below the apex of the heart to above aortic arch, with a sampling frame rate of approximately 300 fps and total scan time of 6-10 minutes.

A total of 136 4DUS datasets were used to implement the machine learning algorithm, taken from previous studies on genetically-induced cardiac hypertrophy. One effort focused on a mutation of  $Nkx2-5^{183P/+}$  [77, 78, 165], consisting of 24 mutant and 24 littermate-control 4DUS datasets. The second focused on a mutation of  $CPT2^{M/-}$  [79, 80], consisting of 41 mutant and 47 littermate-control 4DUS datasets. While each of these studies does include repeated imaging on some mice at numerous time-points, for the scope of this work each 4DUS scan was treated as independent data. All animal experiments were approved by the Purdue University Institutional Animal Care and Use Committee (protocol code 121100077326; approved December 11, 2015).

### 5.3.2 4DUS Analysis and Contour Structure

Each 4DUS dataset is loaded into a custom interactive toolbox developed in MATLAB (MathWorks Inc.), where data is first reoriented to align to a standard axis and then the endo- and epi-cardial boundaries are manually tracked across a representative cardiac cycle (Figure 22A). The standard axes follow a cartesian coordinate system, and are defined by: 1) the left-ventricular apex and center of the base both fall on the z-axis, 2) the anterior and posterior walls fall along the y-axis, and 3) the septal wall falls on the negative x-axis (i.e., standard radiological orientation). Following reorientation, the z-axis location of the apex and base are tracked across the cardiac cycle (Figure 22B). Then iteratively at each point in time, four equally spaced parallel short-axis slices are interpolated from the reoriented 4DUS data, corresponding to 25, 50, 75, and 100% of the distance from the apex to base. The initial tracking of base and apex locations allows for through-plane motion to be compensated for during subsequent wall-tracking.

In order to create a final three-dimensional mesh of the endo- and epi-cardial boundaries of the left ventricle, a structured subset of points was defined (Figure 22C) such that: 1) each of the four parallel slices contains six points for each of the two boundaries, 2) those points are constrained to equally spaced rotations around the central z-axis (i.e., 30, 90, 150, 210, 270, and 330 degrees relative to the positive x-axis), and 3) the distance between each point and the central

z-axis is a function of relative time across the cardiac cycle. Once all points are individually repositioned across the cardiac cycle to define the regional kinematics, hobby splines were used to interpolate a three-dimensional mesh of the left-ventricle at a standardized array of cycle-positions. Specifically for this work, the final 4D mesh of the left-ventricle included 60 locations around the z-axis, 60 locations from the apex-to-base along the z-axis, and 60 time-points across the cardiac cycle.

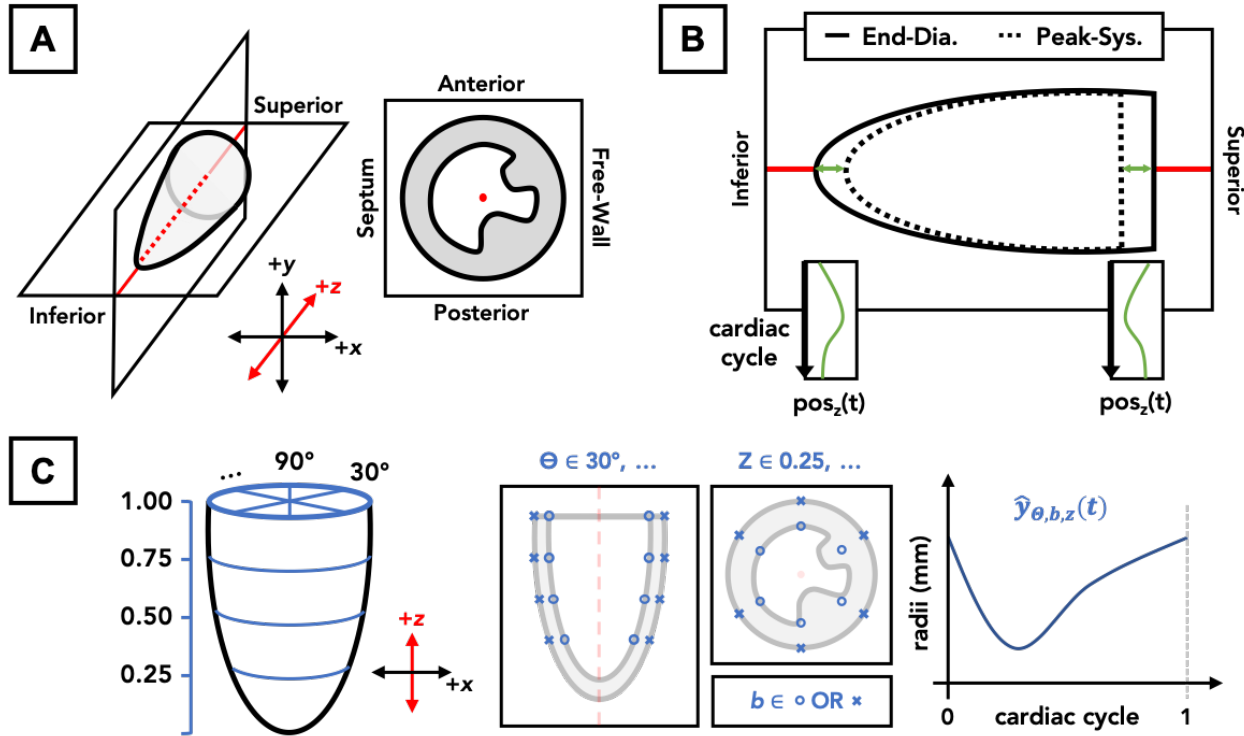


Figure 22. Schematic for post-acquisition analysis on left-ventricular 4DUS data, including: (A) spatial reorientation to align with a central z-axis (i.e., inferior (-z) to superior (+z)), (B) tracking of apex and base locations, and (C) definition of boundary points on the endo- and epi-cardial boundaries (Eq. 14), excluding papillary muscles, to be tracked across the cardiac cycle.

### 5.3.3 Machine Learning Algorithms

#### 5.3.3.1 Prediction Objective

In this context, a machine learning model takes a given 4DUS image as input and returns two predicted 3D surfaces (one for the endocardial boundary, one for the epicardial boundary) for each timepoint. The nature of the task immediately presents several difficulties: the data is high dimensional (160,000 pixels per image with about 5,000 total images), US data naturally contains

speckle noise, and the model output consists of two smooth 3D surfaces across time with no specified parametric form. The data processing approach described in section 2.2 significantly reduces the problem complexity while still allowing for flexible contours to be estimated. Predicting radial distances of each anchor point becomes a regression problem, with the complete contours being inferred using smoothing splines after the anchor points have been estimated.

### 5.3.3.2 Modeling Approach

In order to manage the high dimensionality of the image data, principal component analysis (PCA) was used to project the US images onto a lower dimensional subspace. Since the selected anchor points have fairly regular movement patterns, we further incorporated smoothing splines to capture the average path for each anchor point across time. The full model incorporates both the rotated, compressed image data along with a smoothing spline basis:

$$\hat{y}_{\theta,b,z}(t) = \mathbf{W}_{k,z}\beta_{\theta,b,z} + \Phi(t)\gamma_{\theta,b,z} \quad [14]$$

where  $\hat{y}_{\theta,b,z}$  indicates the predicted response vector of radii for the anchor point indexed by the given angle, boundary, and horizontal slice respectively.  $\mathbf{W}_k$  is represents the pixel image data for image slice  $z$ , which has been compressed using the first  $k$  principal components.  $\Phi(t)$  represents the time-dependent smoothing spline basis, and  $\beta_{\theta,b,z}$  and  $\gamma_{\theta,b,z}$  represent the parameter vectors to be fit for each  $(\theta, b, z)$  combination. The model was fit using least squares.

### 5.3.3.3 Model Variants

We also explored two other model variations for comparison. With model 1 (Eq. 14) given above, the second model (Eq. 15) uses principal components from all  $z$  slices combined for each anchor point, instead of only using the horizontal slice of the target anchor point:

$$\hat{y}_{\theta,b,z}(t) = \mathbf{W}_k\beta_{\theta,b,z} + \Phi(t)\gamma_{\theta,b,z} \quad [15]$$

This approach was utilized to see if information from the other three slices aids in model prediction. Our third model (Eq. 16) simulates a scenario where the machine learning model is human-assisted:

$$\hat{y}_{\theta,b,z}(t) = \mathbf{W}_k\beta_{\theta,b,z} + \Phi(t)\gamma_{\theta,b,z} + \delta\mu_{\theta_0,b_0,z_0} \quad [16]$$

where  $\mu_{\theta_0, b_0, z_0}$  is the true radius for the given anchor point, and  $\delta$  is a single additional scalar parameter to be fit. In this case, the model assumes that a user has provided the annotation of a single anchor point, of the 48 total, at the beginning image of each full US dataset. Thus, the model has access to the true target response value for one of the roughly 1500 anchor points to be predicted for a given spatiotemporal location. This approach was taken to see whether a single annotation could significantly help in the prediction of the rest of the anchor points in the video sequence. If effective, this strategy could enhance model accuracy with only minor additional effort from a user.

### 5.3.4 Measuring Model Performance

To test the effectiveness of the developed models, 100 iterations of Monte Carlo cross-validations were used on the dataset with a training/validation/test split ratio of 6:1:1. The validation sets were used to select the number of principal components for each permutation of the data, while mean squared error (MSE) and  $R^2$  values were evaluated on the held-out test set. To provide an additional measure of difference between the models, we performed pairwise t-tests across the three models for the MSE within each permutation of the test set for each setting of  $(\theta, b, z)$ . Due to the large test-set sample size (i.e., over approximately 500), assumption of normality of the sample mean difference was considered appropriate. The percentage of t-tests with  $p < 0.05$  was computed, aggregated across the angles, short-axis slices, and Monte Carlo sample. We note that this does not necessarily provide any statistical guarantees regarding Type I/II error rates, but is intended instead to serve as an additional metric for model comparison.

### 5.3.5 Description of Metrics Derived from LV Mesh

Once a final 4D mesh of the left-ventricle is created, a series of metrics that characterize its regional kinematics are systematically extracted based on the Lagrangian-definition of linear or engineering strain [14, 15, 18, 180] in both the circumferential (Eq. 17) or longitudinal frame (Eq. 18):

$$\varepsilon_c(t, z) = \frac{\textit{perimeter}_t - \textit{perimeter}_{t=0}}{\textit{perimeter}_{t=0}} \quad [17]$$

$$\varepsilon_L(t, \theta) = \frac{\textit{length}_t - \textit{length}_{t=0}}{\textit{length}_{t=0}} \quad [18]$$

where each metric is a function of time  $t$  (i.e., a given position within the cardiac cycle), and circumferential and longitudinal strain curves are a function of both position  $z$  (i.e., location along the  $z$ -axis) and angle  $\theta$  (i.e., rotation from the positive  $x$ -axis), respectively. Furthermore, additional metrics can be derived from each curve including the early/late systolic strain rates and early/late diastolic strain rates, providing insight into how the heart is moving between end-diastolic and peak-systolic states.

To assess the robustness and practical use of the machine learning-based predictions of wall kinematics, these metrics were computed at select locations in the circumferential (e.g. basal, mid-LV, and apical) and longitudinal (e.g. anterior, posterior, anterior free-wall and septum, and posterior free-wall and septum) frames. Derived metrics from both the ground-truth and machine learning-predicted boundaries were compared using paired t-tests with Bonferroni-Dunn's multiple comparisons corrections. We note that the distribution of several metrics showed some minor deviations from normality (e.g. slight skewness). Adjusted Shapiro-Wilk tests suggested non-normality for roughly 10% of the cross-validation samples. However, the central limit theorem ensures that even when deviations exist from normality among the individual observations, the sampling distribution of the test statistic converges to a normal distribution with larger sample sizes. The recommended sample size threshold for assuming normality via the central limit theorem is 30 [181]. As the sample sizes used for our t-tests were roughly 600, it is safe to assume normality of the computed test statistics.

## 5.4 Results and Discussion

### 5.4.1 Model Fitting Results

A visual summary of the test set prediction results for models 1, 2, and 3 are demonstrated in Figure 23A, B, and C, respectively. Qualitatively, we can see improvements in  $R^2$  and mean squared error (MSE) for each successive model. Of note, we observe higher MSE for all three models around the posterior-septum in the basal slice. We believe this may be because the basal septum commonly lies posterior to the sternum and is thus affected by shadowing artifacts. Not only does that make the basal septum harder to annotate, which lowers precision in the ground-truth data, but also the lack of border contrast means it may be incorrectly accounted for in the PCA-based image compression.

Table 3 provides a numerical summary of the three models' performance. We notice that with regard to every metric in Table 3, model 2 outperforms model 1, and model 3 outperforms model 2. Taken together, these results suggest that simultaneously incorporating all four slices in the prediction model (model 2) yields modest but noticeable improvement over using individual slices (model 1). Furthermore, annotation of a single point at  $t=0$  (model 3) can significantly improve model predictive accuracy above the previous versions not incorporating user annotations.

Table 3. Numerical comparison of model performance for both endocardial and epicardial boundaries. With each model, mean test-set MSE with associated standard deviations and  $R^2$  values are displayed. Additionally, the percentage of significant t-tests when the given row's model's test set MSE is smaller than that of the model indicated in the column is also provided.

|                | Endocardial            |                |            |            | Epicardial             |                |            |            |
|----------------|------------------------|----------------|------------|------------|------------------------|----------------|------------|------------|
|                | MSE (mm <sup>2</sup> ) | R <sup>2</sup> | vs. M1 (%) | vs. M2 (%) | MSE (mm <sup>2</sup> ) | R <sup>2</sup> | vs. M1 (%) | vs. M2 (%) |
| <b>Model 1</b> | 0.069 ± 0.054          | 0.41           | ---        | ---        | 0.068 ± 0.044          | 0.51           | ---        | ---        |
| <b>Model 2</b> | 0.060 ± 0.049          | 0.49           | 48.7       | ---        | 0.058 ± 0.039          | 0.59           | 54.4       | ---        |
| <b>Model 3</b> | 0.030 ± 0.021          | 0.71           | 88.0       | 83.5       | 0.037 ± 0.020          | 0.71           | 81.9       | 71.3       |

While Figure 23 and Table 3 summarize aggregated model performance across all 100 test-set permutations, it also is instructive to see a particular example of the models' predictions vs. the ground truth. Figure 24A shows the predicted vs. actual radii for the 30° endocardial anchor point at the base of the heart plotted for a single test set using model 2. Qualitatively, model 2's predictions overall appear relatively close to the ground truth. Errors in predictions seem to be mainly due to offsets in the size of the heart, rather than the wall kinematics (i.e., curve shape is correct but placed off from border). Figure 24B and E shows the accuracy gained using model 3 by incorporating user-assistance on an endocardial point. The heart size is more accurately inferred in this case, yielding better predictions overall. These results illustrate that qualitatively, both the unassisted and assisted models show reasonable performance for both the endocardial and epicardial boundaries on unseen data, with slightly higher accuracy for the endocardial boundary (Figure 24A and B vs. D and E). Additionally, although the unassisted model's predictions are relatively close to the ground truth (Figure 24A and D), the assisted model yields noticeably improved performance, especially for the endocardial boundary (Figure 24B).

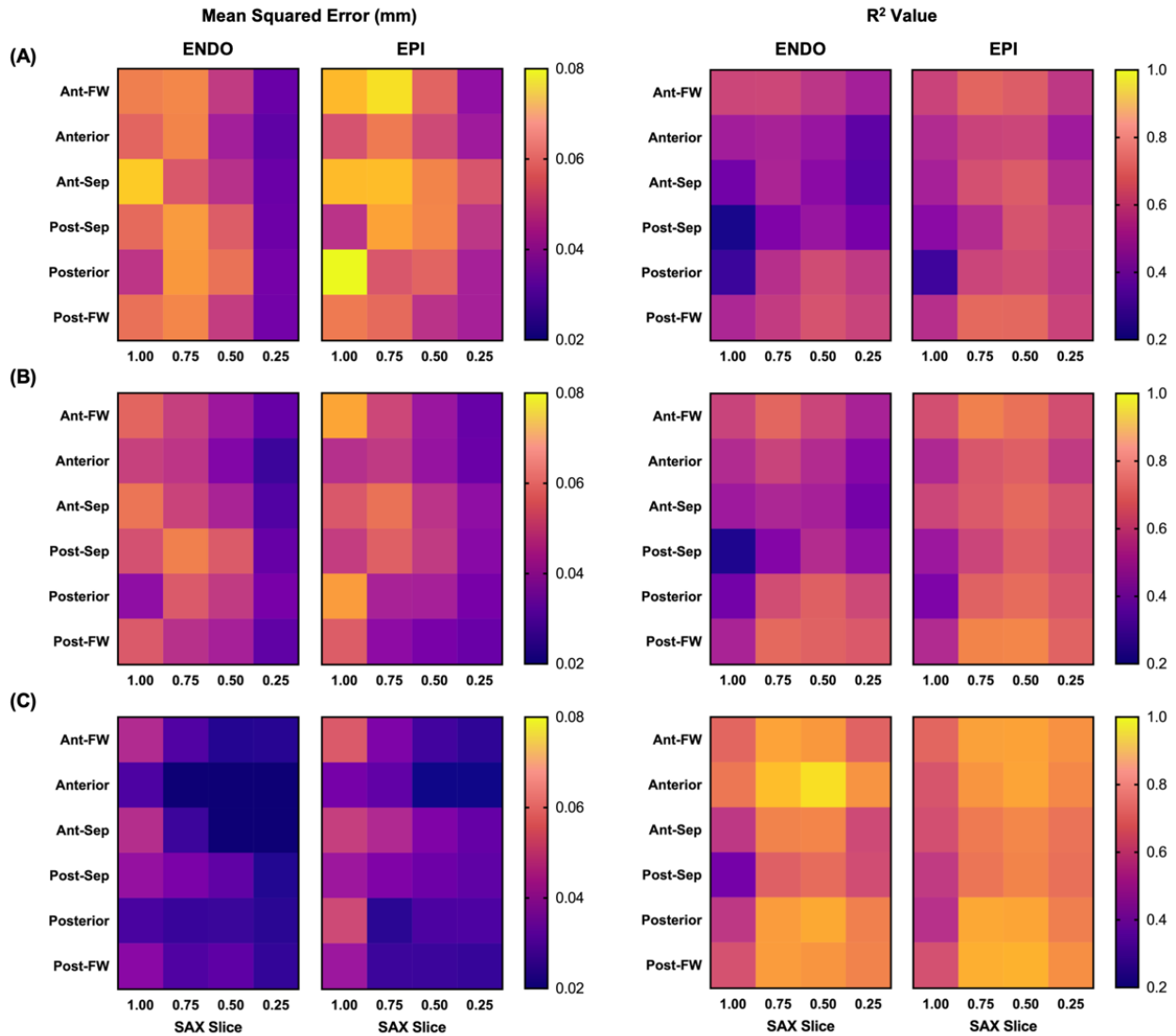


Figure 23. Heatmap representations of median mean-squared-error (left) and associated R values (right) following 100 Monte Carlo simulations of the 6:1:1 testing paradigm, stratified by theta, b, and z. Predictions are based on models (A) 1 (i.e., individual z slices), (B) 2 (i.e., combined z slices), and (C) 3 (i.e., assisted). Specifically here, model 3 was assisted by incorporating t=0 radius values taken from the endocardial anterior mid-ventricle position (i.e., z=0.5, theta=90 deg).

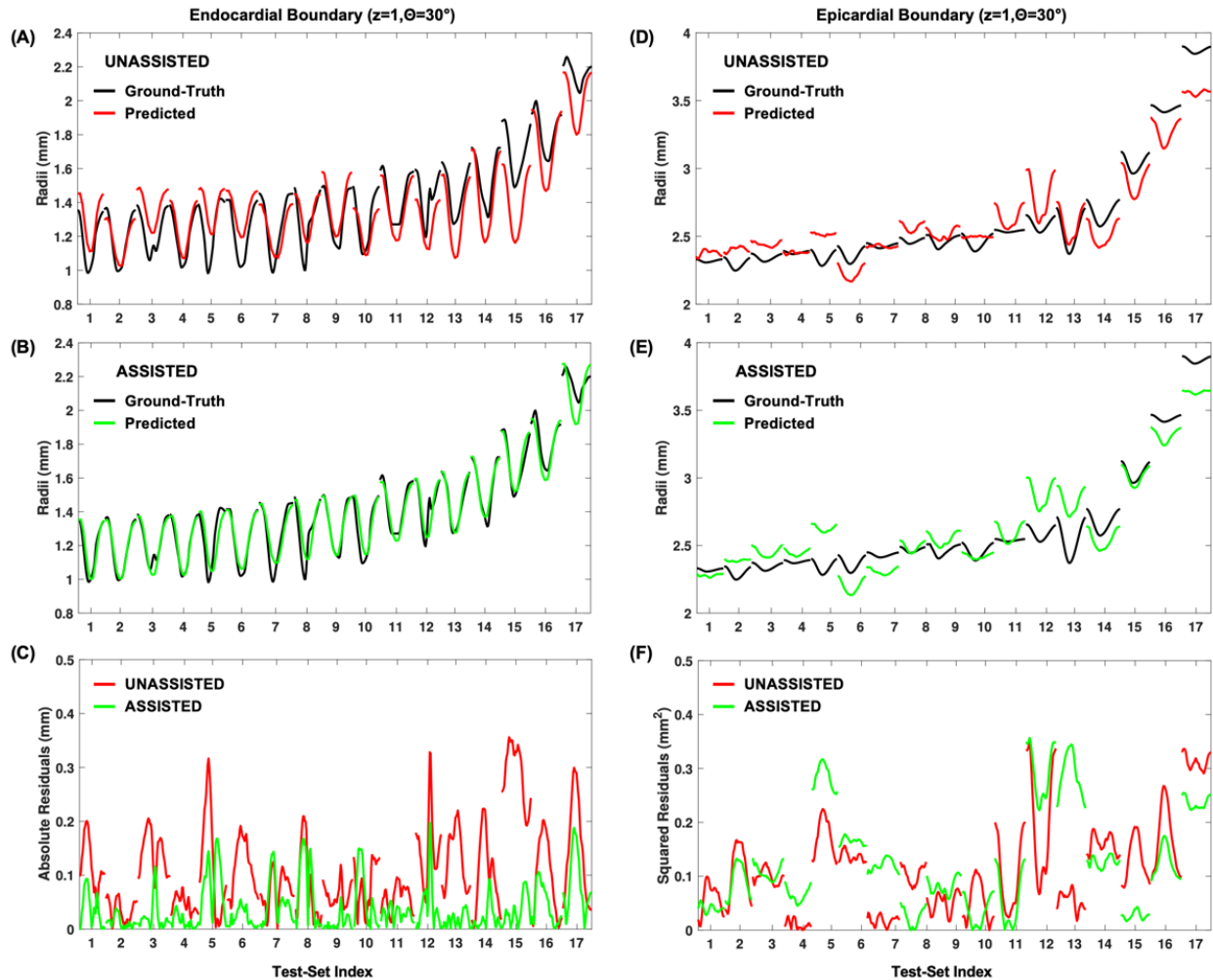


Figure 24. Example predictions on a series of anterior free-wall test set data, based on the implemented 6:1:1 Monte Carlo cross-validation. Raw predictions for 17 separate mice are shown overlaid onto the ground-truth data for unassisted (model 2) predictions at both the (A) endocardial and (D) epicardial borders, as well as for the (B/E) assisted (model 3) predictions. Squared error plots at each temporal sample for the (C) endocardial and (F) epicardial positions demonstrate the potential lower errors resulting from the assisted approach.

#### 5.4.2 Performance of Predication-Based Metrics

Aiming to assess the practicality of using the three proposed models to characterize cardiac function, we computed all metrics described in section 2.4 and compared results based on predicted and ground-truth boundaries. The results of paired t-tests on all 80 metrics, with Bonferroni-Dunn’s multiple comparisons corrections, are shown in Supplemental Table 3, stratified by model. Following trends observed in section 3.1, the number of metrics that were flagged as significantly different (i.e., adjusted  $p < 0.001$ ) from the ground-truth values were relatively low amongst

models 1 (8/80), 2 (7/80), and 3 (8/80). Interestingly, seven metrics showed significant differences regardless of model, suggesting further refinement of the modelling approach would be needed to trust those values if based on machine learning predictions alone. As shown in Supplemental Table 3, these metrics were all variants of early diastolic strain rate: 1) circumferential early diastolic strain rates at the mid-ventricle and apex; and 2) longitudinal strain at each of the six rotations around the z-axis, except at the posterior-septum. While it is not clear why early diastolic strain rate has trouble being properly inferred using our methods, it may be due to the incorporation of severely diseased mice with abnormal diastolic kinematic profiles adversely skewing the imposed temporal-smoothing.

It should be noted that no global function metrics (i.e., end-diastolic or peak-systolic volumes, ejection fraction, or stroke volume) or peak-strain values showed any statistically significant differences between the gold-standard and prediction-based analyses. These results appear promising as the errors are only observed with strain-rate values, specifically early diastolic strain rate, suggesting that the machine learning model predictions of left-ventricle boundaries can be used reliably to assess both global cardiac function and peak circumferential and longitudinal strain. Nevertheless, it is important to note that accurate measurements of early diastolic strain rate are critical to the assessment of diastolic dysfunction [182]. Future work increasing model complexity or implementing novel strategies is thus critical to providing more reliable assessments of cardiac kinematics and function for researchers and clinicians.

### **5.4.3 Limitations**

While we are able to measure model performance, more thorough assessment of inter-observer variability in creation of ground-truth could be used to give further confidence in the physiological accuracy of detected boundaries. For example, if model predictions were well within the range of different users' annotations, then this would give further support to the model's capability. Furthermore, as seen in Figure 23 and visualized in Figure 25, the septal and posterior walls at the base of the left ventricle are susceptible to prediction errors due to the presence of sternum shadow artifacts and the mitral valve and myocardium interface, respectively. The shadow artifacts can be mitigated by angling the ultrasound probe during acquisition; however, this must be traded-off with undesirable air-based artifacts from the left lung. Additionally, while the mitral valve

blending into the myocardium can reduce local contrast, carefully selecting a base location just inferior to the interface can help maintain a proper view of the endo- and epi-cardial borders.

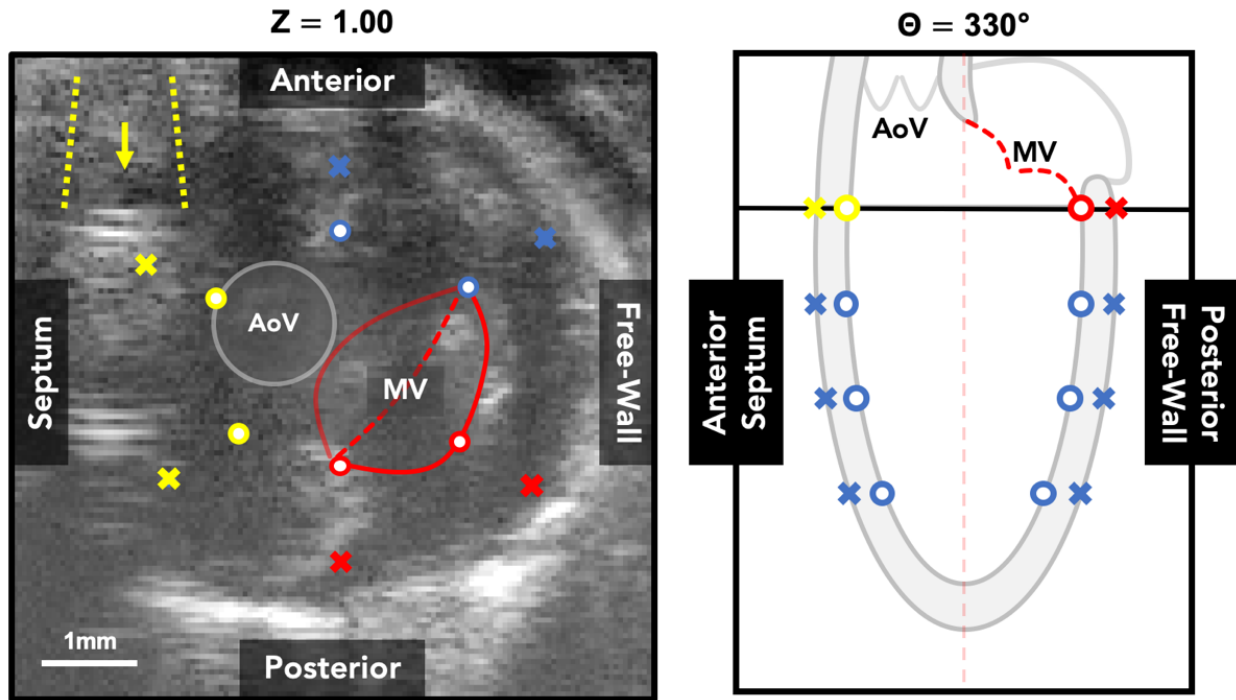


Figure 25. Example short-axis ultrasound image at the base of the heart demonstrating the location of sternum shadow artifacts (yellow) and mitral valve attachments to the left ventricular myocardium (red). Points most commonly affected are color-coded and displayed on a corresponding long-axis schematic.

Another natural limitation in working with medical image data is the tendency to have small sample sizes relative to the dimensionality of the data. While we did have a moderate number of videos to work with – 136 in total with 30-40 temporal samples – this is relatively few compared to several standard machine learning datasets (e.g. the ImageNet database containing 14 million plus images), but future work will be needed increase the number of training datasets used to build these models. Larger sample sizes not only improve the performance of a given model, but allow for more flexible (i.e., higher dimensional) models to be trained with less risk of overfitting.

#### 5.4.4 Future Applications

As more data is gathered, several avenues exist for extensions or alternatives of the methods proposed in this paper. Notably, with a larger number of images, the use of deep learning for image

segmentation, especially convolutional neural networks, would likely become a promising option to explore. Even with moderate sample sizes, the use of deep generative models such as *generative adversarial networks* (GANs) [183] may provide a mechanism to augment the true dataset with near-realistic images that would enhance model training. GANs have already shown promise in several areas of medical imaging [184-187], and thus would be a natural choice for generation of realistic-looking murine US images. Other data augmentation strategies that have been proposed for medical image generation specifically, such as ASNG [188], could be explored as well. *Transfer learning* [189] may be a viable option that could be applied even without additional real or generated data, incorporating a pre-trained network from another application domain. Finally, if a network were developed that could segment murine cardiac images with very high accuracy, it is likely that such a model would be useful in clinical applications, even if downstream transfer learning is only used to fine-tune models on human cardiac images.

Another aspect of this work that could have a more direct impact on clinical translation is the use of a structured grid to sample cardiac kinematics (i.e., four-slices across and six rotations around the LV). While recent studies into 3D speckle-tracking echocardiography have shown promise in characterizing clinical data [153], contours of the left-ventricular boundaries are often unstructured and tracking speckle-patterns is susceptible to error propagation if there is subpar image quality or notable image artifacts. Using an approach similar to the one presented here could allow for the problem of boundary predictions to be simplified and lead to more robust results when speckle-tracking is insufficient, which is a common obstacle associated with murine 4DUS data analysis.

## 5.5 Conclusions

We demonstrate here the first application of machine learning to the prediction of left-ventricular wall boundaries in murine 4DUS image data. Our results demonstrate notably better agreement between ground-truth and predicted locations when using a model based on a combination of parallel short-axis images compared to treating all images separately. This agreement of predicted locations can then be marginally improved further when incorporating a single boundary point starting location into the model. Furthermore, our results suggest that reliable assessments of global cardiac function and strain, except early diastolic strain-rates, can be derived from the machine learning predictions alone. While future work will aim to strengthen the model efficiency

and account for additional murine cardiac disease models, this study reveals that incorporation of machine learning can help vastly increase the reliability and speed of murine cardiac 4DUS data analysis.

## 6. CONTRIBUTIONS TO SCIENTIFIC KNOWLEDGE

### 6.1 Overview and Impact of Research Findings

We have demonstrated in this dissertation the development of high-frequency four-dimensional ultrasound (4DUS) and its application to two separate models of hypertrophic cardiomyopathy. Conventional use of high-frequency ultrasound to evaluate murine cardiac function has relied on either M-Mode or B-Mode imaging, which both require assumptions of ventricular geometry to estimate chamber volumes and extract global function metrics. Not only have we shown that these assumptions lead to a larger variability in measurements compared to volumetric imaging approaches, but they are also subject to errors based on proper positioning of the ultrasound probe to either the true short-axis or long-axis of the heart. The results of our validation study show that not only can 4DUS provide global cardiac function measurements on par with cine-MRI, but its inherent volumetric structure allows for it to be digitally reoriented to a standardized reference frame and thus can mitigate misalignment errors in the subsequent results.

As an extension of our 4DUS validation work, we also present here a standardized protocol from which a comprehensive set of regional kinematics can be measured. This can be of significant benefit to the cardiac research community, as a simultaneous measurement of global function, myocardial morphometry, and both regional circumferential and longitudinal strain can help streamline the cardiac assessment process. Additionally, the 4D mesh of endocardial and epicardial left-ventricular boundaries that are created from our analysis can serve as a foundation for more advanced explorations of myocardial tissue biomechanics. Our study of *Cpt2<sup>M-/-</sup>* mice provided insight that the circumferential strain at the base of the heart and longitudinal strain along the poster wall may be the most sensitive metrics to disease progression. Using a mathematical combination of these two metrics, which we named the Hybrid Strain Index (HSI), we were able to create a marker of pathological hypertrophy that was more sensitive to disease progression than ejection fraction. Our study of *Nkx2-5<sup>183P/+</sup>* mice similarly showed that the circumferential strain at the base of the heart is impacted early in the disease process (i.e., 8 weeks old), reinforcing our findings in the *Cpt2<sup>M-/-</sup>* work. This study also proposed the derivation of spatiotemporal strain maps, which provide a more comprehensive visualization of cardiac kinematics in both the circumferential and longitudinal reference frames. We demonstrate how these spatiotemporal maps can be used to

perform pixelwise analysis across cross-sectional and longitudinal data, and suggest how future research using these maps and associated analysis methods may further support their use as a novel way to characterize cardiac function.

Finally, as data science further integrates into biomedical engineering as a means to make sense of big data, we explored the application of machine learning to help accelerate the analysis of 4DUS data. Using the vast array of 4DUS data collected for the *Cpt2*<sup>M/-</sup> and *Nkx2-5*<sup>I83P/+</sup> studies, comprised of both healthy and diseased hearts, we developed and tested three different machine learning models to predict endocardial and epicardial boundaries based on images derived from 4DUS data. Our findings show that the best prediction performance is achieved using a combination of multiple parallel short-axis slices and a single ground-truth position, suggesting that leveraging the volumetric nature of 4DUS data produces more reliable results. Additionally, we have integrated the machine learning algorithms into the developed 4DUS analysis toolbox, which can predict boundaries in a new 4DUS dataset within seconds. Taken all together, the presented dissertation lays the foundation for a semi-automatic and comprehensive cardiac assessment toolbox that can help researchers both better understand cardiac disease mechanics and evaluate treatment efficacy using high frequency 4DUS technology.

## 6.2 Directions for Future Research

Future work in this area would look to further develop our 4DUS analysis methods through three specific avenues. First, and likely the most necessary next step, would be the incorporation of wall rotation into the characterization of left-ventricular kinematics. The twisting of the left ventricle through the cardiac cycle is a known phenomenon due to the varying transmural myocardial fiber directions, and literature suggests that that twisting motion can be impacted by disease processes [130, 190, 191]. Incorporating an additional step into the 4DUS analysis procedure to track the relative rotation of the endocardial and epicardial borders at each parallel short-axis slice might help to estimate torsion and more completely characterize left-ventricular kinematics. Second, applications of these methods to a more diverse array of cardiac disease models would help to both further demonstrate the utility of our analysis and identify disease-specific patterns of wall kinematics. Third, leveraging a growing pool of 4DUS data, further exploration of machine learning algorithms and artificial intelligence could help to turn the developed 4DUS toolbox into a reliable push-button software. Not only would this be of significant use to the researchers

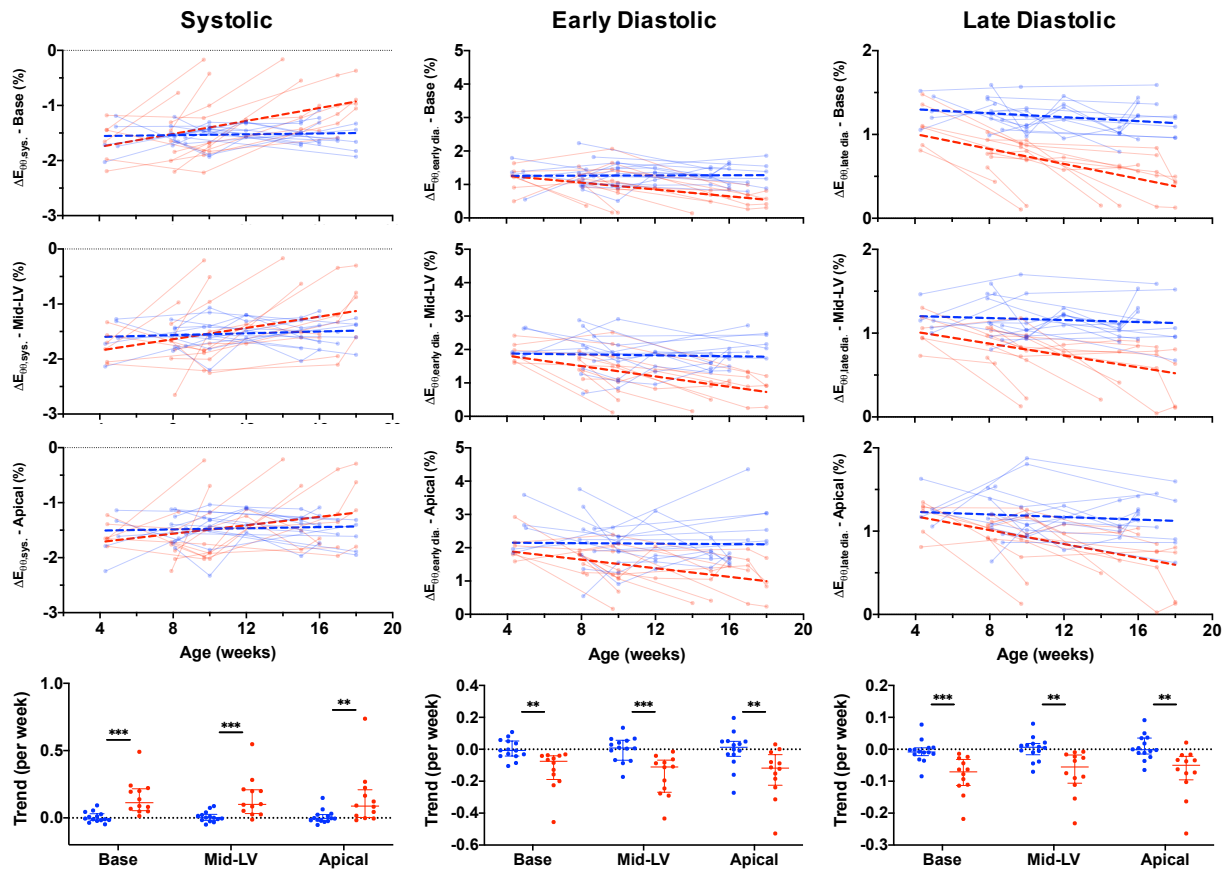
investigating small animal models of cardiac disease, but it could also help innovate on machine learning methods for analyzing clinical cardiac imaging data.

Complementary to the envisioned advancements for high-frequency 4DUS technology, we also envision this work to also translate for clinical applications. As the developed standardized procedure for characterizing regional left-ventricular kinematics only necessitates 4D imaging data as an input, we would look to obtain and analyze various human 4D cardiac disease data. Following additional validation studies, not only could our methods provide both novel function metrics and visualizations of cardiac kinematics, but it could also serve as a foundation for understanding the connection between the cardiac biomechanics we observe in small animal models and their clinical counterparts. This future work could then strengthen the ability for preclinical studies to make an impact on important clinical decisions and more directly improve patient care.

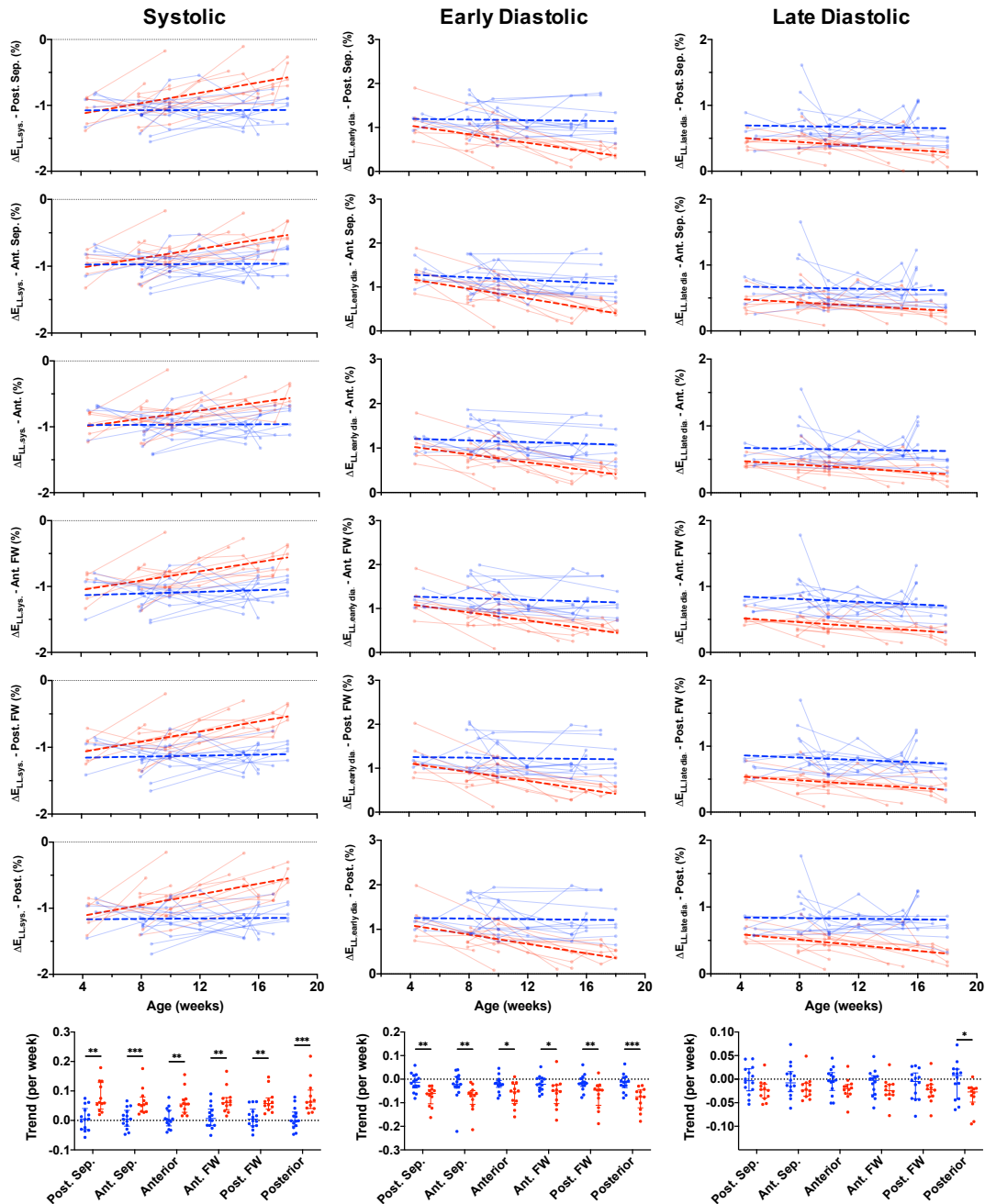
## APPENDIX A. SUPPLEMENTAL DATA TO CHAPTER 3

Supplemental Table 1. Measurements of strain rate trends through aging. For each cohort, medians [interquartile ranges] are provided for control and *Cpt2<sup>M/-</sup>* mice, along with *p*-values from Mann-Whitney tests, ratio of interquartile ranges (IQR) in *Cpt2<sup>M/-</sup>* and control trends, area under curve (AUC) values, and the 95% confidence interval (CI) intersection locations. Metrics where 95% confidence intervals overlapped for the entire age range of the study were noted with “---”, and metrics where 95% confidence intervals did not overlap are noted with “DNO”.

| Metric                             |                                     | Control (n=14)         | <i>Cpt2<sup>M/-</sup></i> (n=12) | <i>p</i> -value        | IQR Ratio | Trend AUC | 95% CI Int. | Metric AUC |
|------------------------------------|-------------------------------------|------------------------|----------------------------------|------------------------|-----------|-----------|-------------|------------|
| $\Delta E_{\theta\theta,sys}$      | Base                                | -0.007 [-0.017,0.027]  | 0.113 [0.058,0.211]              | 0.0002                 | 3.50      | 0.935     | 11.49       | 0.603      |
|                                    | Mid-LV                              | 0.001 [-0.016,0.022]   | 0.100 [0.039,0.206]              | 0.0009                 | 4.41      | 0.887     | ---         | 0.533      |
|                                    | Apical                              | -0.004 [-0.022,0.023]  | 0.088 [0.007,0.194]              | 0.0069                 | 4.13      | 0.815     | ---         | 0.558      |
| $\Delta E_{LL,svs}$                | Ant. FW                             | 0.007 [-0.017,0.034]   | 0.060 [0.041,0.076]              | 0.0026                 | 0.69      | 0.851     | 7.63        | 0.800      |
|                                    | Anterior                            | 0.002 [-0.014,0.032]   | 0.056 [0.031,0.071]              | 0.0013                 | 0.86      | 0.875     | 9.65        | 0.715      |
|                                    | Ant. Sep.                           | 0.004 [-0.016,0.030]   | 0.054 [0.030,0.075]              | 0.0009                 | 0.99      | 0.887     | 9.63        | 0.720      |
|                                    | Post. Sep.                          | 0.004 [-0.030,0.034]   | 0.060 [0.044,0.124]              | 0.0019                 | 1.24      | 0.863     | 9.45        | 0.732      |
|                                    | Posterior                           | -0.001 [-0.018,0.024]  | 0.062 [0.041,0.096]              | 0.0008                 | 1.32      | 0.893     | 7.61        | 0.813      |
|                                    | Post. FW                            | 0.005 [-0.017,0.030]   | 0.057 [0.041,0.074]              | 0.0019                 | 0.69      | 0.863     | 7.05        | 0.832      |
|                                    | $\Delta E_{\theta\theta,early dia}$ | Base                   | -0.008 [-0.042,0.050]            | -0.076 [-0.178,-0.041] | 0.0016    | 1.49      | 0.869       | 9.04       |
| Mid-LV                             |                                     | 0.008 [-0.068,0.054]   | -0.111 [-0.261,-0.073]           | 0.0006                 | 1.55      | 0.899     | 8.50        | 0.760      |
| Apical                             |                                     | 0.013 [-0.033,0.049]   | -0.118 [-0.212,-0.049]           | 0.0081                 | 1.98      | 0.810     | 8.11        | 0.766      |
| $\Delta E_{LL,early dia}$          | Ant. FW                             | -0.022 [-0.043,0.003]  | -0.050 [-0.099,-0.026]           | 0.0328                 | 1.60      | 0.750     | 6.89        | 0.831      |
|                                    | Anterior                            | -0.020 [-0.028,-0.007] | -0.054 [-0.100,-0.028]           | 0.0372                 | 3.36      | 0.744     | 6.99        | 0.820      |
|                                    | Ant. Sep.                           | -0.021 [-0.032,0.009]  | -0.065 [-0.100,-0.052]           | 0.0059                 | 1.17      | 0.821     | 7.78        | 0.776      |
|                                    | Post. Sep.                          | -0.013 [-0.030,0.016]  | -0.061 [-0.095,-0.046]           | 0.0031                 | 1.06      | 0.845     | 6.84        | 0.849      |
|                                    | Posterior                           | -0.013 [-0.029,0.007]  | -0.074 [-0.115,-0.048]           | 0.0009                 | 1.88      | 0.887     | 6.91        | 0.848      |
|                                    | Post. FW                            | -0.018 [-0.027,0.002]  | -0.046 [-0.101,-0.034]           | 0.0081                 | 2.29      | 0.810     | 7.19        | 0.839      |
| $\Delta E_{\theta\theta,late dia}$ | Base                                | -0.008 [-0.016,0.005]  | -0.071 [-0.113,-0.036]           | 0.0004                 | 3.79      | 0.911     | DNO         | 0.933      |
|                                    | Mid-LV                              | 0.006 [-0.010,0.017]   | -0.055 [-0.101,-0.020]           | 0.0011                 | 3.00      | 0.881     | 6.07        | 0.874      |
|                                    | Apical                              | -0.001 [-0.012,0.035]  | -0.050 [-0.089,-0.026]           | 0.0016                 | 1.36      | 0.869     | 8.51        | 0.747      |
| $\Delta E_{LL,late dia}$           | Ant. FW                             | -0.003 [-0.032,0.006]  | -0.024 [-0.033,-0.011]           | 0.1167                 | 0.59      | 0.685     | DNO         | 0.912      |
|                                    | Anterior                            | -0.003 [-0.020,0.012]  | -0.020 [-0.031,-0.013]           | 0.0849                 | 0.57      | 0.702     | 5.64        | 0.855      |
|                                    | Ant. Sep.                           | -0.008 [-0.024,0.012]  | -0.023 [-0.035,-0.010]           | 0.1897                 | 0.70      | 0.655     | 6.37        | 0.807      |
|                                    | Post. Sep.                          | -0.003 [-0.022,0.021]  | -0.023 [-0.039,-0.012]           | 0.0538                 | 0.63      | 0.726     | 5.96        | 0.839      |
|                                    | Posterior                           | 0.008 [-0.042,0.021]   | -0.027 [-0.045,-0.019]           | 0.0288                 | 0.41      | 0.756     | DNO         | 0.912      |
|                                    | Post. FW                            | -0.005 [-0.041,0.010]  | -0.022 [-0.037,-0.012]           | 0.2917                 | 0.48      | 0.625     | DNO         | 0.910      |



Supplemental Figure 1. Measurements of systolic (sys.; left column), early diastolic (early dia.; middle column), and late diastolic (late dia.; right column) circumferential strain rates, derived from the base, mid-ventricle (Mid-LV), and apical regions of the left ventricle. Data from control mice shown in blue and Cpt2M<sup>-/-</sup> mice shown in red. Points from the same mouse are shown connected, and linear regression performed on across each cohort are visualized with thick dashed lines. Comparison plots of strain rate trends from each mouse and region are shown (bottom), with horizontal lines designating median and interquartile ranges. Significance markers above each comparison plot indicate p-value level from non-parametric Mann-Whitney tests (\*\*\*p < 0.001; \*\*p < 0.01).

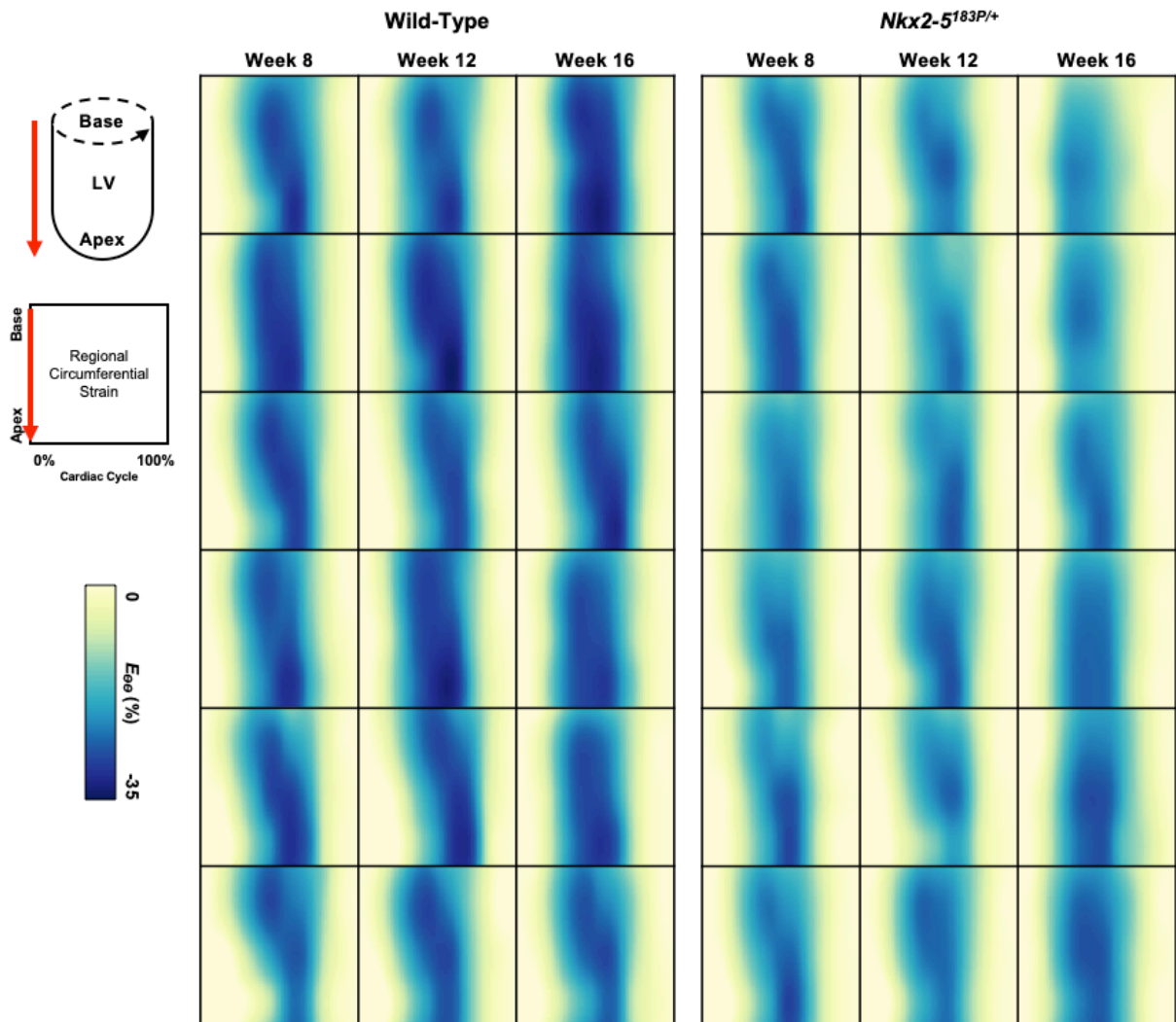


Supplemental Figure 2. Measurements of systolic (sys.; left column), early diastolic (early dia.; middle column), and late diastolic (late dia.; right column) longitudinal strain rates, derived from the posterior septum (Post. Sep.), posterior (Post.), posterior free-wall (Post. FW), anterior free-wall (Ant. FW), anterior (Ant.), and anterior septum (Ant. Sep.) regions of the heart. Data from control mice shown in blue and *Cpt2*<sup>M-/-</sup> mice shown in red. Points from the same mouse are shown connected, and linear regression performed on across each cohort are visualized with thick dashed lines. Comparison plots of strain rate trends from each mouse and region are shown (bottom), with horizontal lines designating median and interquartile ranges. Significance markers above each comparison plot indicate p-value level from non-parametric Mann-Whitney tests (\*\*\* $p < 0.001$ ; \*\* $p < 0.01$ ; \* $p < 0.05$ ).

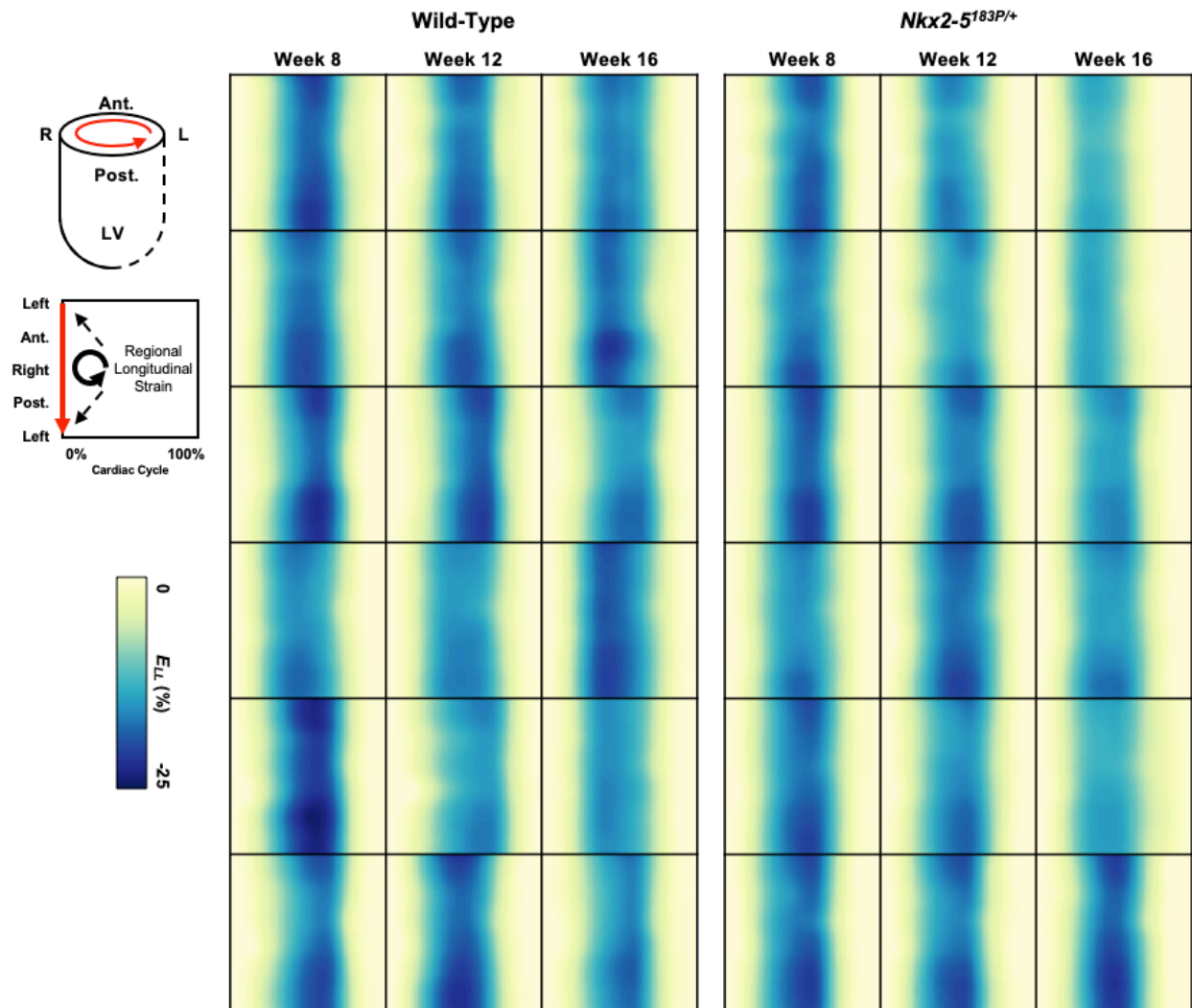
## APPENDIX B. SUPPLEMENTAL DATA TO CHAPTER 4

Supplemental Table 2. Global and regional cardiac function metrics derived from wild-type and *Nkx2-5<sup>fl83P/+</sup>* 4DUS data, compared at 8, 12, and 16 weeks old. Summary values for each cohort and imaging time-point are shown as mean (standard deviation). Comparisons were performed using a two-way repeated measures ANOVA with post-hoc Bonferroni's multiple comparisons test;  $p < 0.05$  was considered statistically significant and corresponding values were highlighted in red. For each region from which either circumferential or longitudinal strain information was analyzed, peak strain, systolic strain rate, early-diastolic strain rate, and late-diastolic strain rate was reported.

| Location and Metric    |                             | Week 8                   |                                 |               | Week 12       |                                 |               | Week 16       |                                 |               |         |
|------------------------|-----------------------------|--------------------------|---------------------------------|---------------|---------------|---------------------------------|---------------|---------------|---------------------------------|---------------|---------|
|                        |                             | Wild-Type                | <i>Nkx2-5<sup>fl83P/+</sup></i> | p-value       | Wild-Type     | <i>Nkx2-5<sup>fl83P/+</sup></i> | p-value       | Wild-Type     | <i>Nkx2-5<sup>fl83P/+</sup></i> | p-value       |         |
| Global                 | End-Diastolic Volume (uL)   | 36.33 (1.57)             | 40.63 (2.22)                    | 0.4434        | 39.32 (1.25)  | 45.03 (2.88)                    | 0.3397        | 37.06 (0.78)  | 38.31 (2.47)                    | >0.9999       |         |
|                        | Peak-Systolic Volume (uL)   | 13.95 (0.82)             | 18.01 (1.08)                    | 0.0433        | 14.85 (0.62)  | 21.09 (1.80)                    | 0.0482        | 13.81 (0.64)  | 17.54 (1.28)                    | 0.0997        |         |
|                        | Stroke Volume (uL)          | 22.38 (0.82)             | 22.62 (1.23)                    | >0.9999       | 24.47 (0.79)  | 23.94 (1.29)                    | >0.9999       | 23.26 (0.59)  | 20.77 (1.51)                    | 0.5126        |         |
|                        | Ejection Fraction (%)       | 61.72 (0.86)             | 55.70 (0.84)                    | 0.0015        | 62.26 (0.83)  | 53.44 (1.44)                    | 0.0022        | 62.79 (1.33)  | 54.15 (1.81)                    | 0.0115        |         |
|                        | Left-Ventricular Mass (mg)  | 85.29 (2.10)             | 102.35 (2.66)                   | 0.0018        | 99.80 (1.72)  | 114.14 (2.90)                   | 0.0081        | 105.33 (2.76) | 122.25 (1.61)                   | 0.0022        |         |
|                        | Average Wall Thickness (mm) | 0.86 (0.01)              | 0.95 (0.02)                     | 0.0151        | 0.93 (0.01)   | 0.99 (0.01)                     | 0.0094        | 0.97 (0.01)   | 1.07 (0.02)                     | 0.0039        |         |
| Circumferential Strain | Base                        | Peak Strain (%)          | -28.10 (0.29)                   | -23.16 (0.72) | 0.0015        | -28.50 (0.50)                   | -22.47 (0.95) | 0.0018        | -28.28 (0.51)                   | -22.78 (1.00) | 0.0045  |
|                        |                             | Systolic Rate (%/norm)   | -1.56 (0.05)                    | -1.54 (0.07)  | >0.9999       | -1.66 (0.06)                    | -1.39 (0.07)  | 0.0590        | -1.75 (0.05)                    | -1.69 (0.04)  | >0.9999 |
|                        |                             | Early Dia. Rate (%/norm) | 0.94 (0.17)                     | 1.06 (0.13)   | >0.9999       | 1.14 (0.12)                     | 1.16 (0.20)   | >0.9999       | 1.23 (0.20)                     | 1.06 (0.09)   | >0.9999 |
|                        |                             | Late Dia. Rate (%/norm)  | 1.41 (0.08)                     | 1.30 (0.04)   | 0.6901        | 1.45 (0.06)                     | 1.36 (0.06)   | >0.9999       | 1.34 (0.08)                     | 1.11 (0.09)   | 0.2191  |
|                        |                             | Peak Strain (%)          | -28.05 (0.55)                   | -25.31 (0.45) | 0.0105        | -28.53 (0.67)                   | -24.89 (0.56) | 0.0060        | -29.03 (0.55)                   | -25.22 (0.80) | 0.0104  |
|                        | Mid-LV                      | Systolic Rate (%/norm)   | -1.54 (0.05)                    | -1.41 (0.04)  | 0.2765        | -1.64 (0.09)                    | -1.36 (0.08)  | 0.1241        | -1.76 (0.08)                    | -1.77 (0.02)  | >0.9999 |
|                        |                             | Early Dia. Rate (%/norm) | 1.80 (0.11)                     | 1.80 (0.06)   | >0.9999       | 2.33 (0.12)                     | 1.85 (0.14)   | 0.0972        | 1.87 (0.08)                     | 1.45 (0.12)   | 0.0526  |
|                        |                             | Late Dia. Rate (%/norm)  | 1.36 (0.08)                     | 1.47 (0.02)   | 0.8459        | 1.37 (0.06)                     | 1.41 (0.05)   | >0.9999       | 1.46 (0.07)                     | 1.18 (0.06)   | 0.0364  |
|                        |                             | Peak Strain (%)          | -29.21 (0.83)                   | -26.99 (0.42) | 0.1387        | -30.25 (0.96)                   | -24.79 (0.79) | 0.0043        | -30.29 (0.95)                   | -25.02 (0.93) | 0.0083  |
|                        |                             | Systolic Rate (%/norm)   | -1.36 (0.11)                    | -1.32 (0.07)  | >0.9999       | -1.37 (0.05)                    | -1.21 (0.08)  | 0.3468        | -1.59 (0.12)                    | -1.67 (0.08)  | >0.9999 |
| Apical                 | Early Dia. Rate (%/norm)    | 2.23 (0.05)              | 2.16 (0.13)                     | >0.9999       | 2.73 (0.25)   | 2.02 (0.10)                     | 0.1150        | 2.24 (0.14)   | 1.49 (0.20)                     | 0.0386        |         |
|                        | Late Dia. Rate (%/norm)     | 1.05 (0.15)              | 1.49 (0.05)                     | 0.0968        | 1.04 (0.18)   | 1.25 (0.14)                     | >0.9999       | 1.50 (0.18)   | 1.19 (0.11)                     | 0.5236        |         |
|                        | Peak Strain (%)             | -19.87 (0.87)            | -18.82 (0.60)                   | >0.9999       | -18.21 (0.75) | -17.68 (0.55)                   | >0.9999       | -17.42 (0.52) | -15.59 (1.09)                   | 0.5164        |         |
| Longitudinal Strain    | Anterior Free-Wall          | Systolic Rate (%/norm)   | -0.98 (0.05)                    | -0.91 (0.02)  | 0.5807        | -0.94 (0.06)                    | -0.86 (0.06)  | >0.9999       | -1.00 (0.08)                    | -0.93 (0.04)  | >0.9999 |
|                        |                             | Early Dia. Rate (%/norm) | 1.41 (0.14)                     | 1.32 (0.14)   | >0.9999       | 1.35 (0.15)                     | 1.23 (0.15)   | >0.9999       | 0.98 (0.15)                     | 1.00 (0.14)   | >0.9999 |
|                        |                             | Late Dia. Rate (%/norm)  | 1.14 (0.14)                     | 1.13 (0.09)   | >0.9999       | 0.95 (0.09)                     | 0.98 (0.04)   | >0.9999       | 0.91 (0.06)                     | 0.77 (0.10)   | 0.8754  |
|                        | Anterior Septum             | Peak Strain (%)          | -18.02 (0.76)                   | -17.41 (0.51) | >0.9999       | -16.52 (0.63)                   | -15.70 (0.66) | >0.9999       | -16.73 (0.61)                   | -14.56 (0.86) | 0.2092  |
|                        |                             | Systolic Rate (%/norm)   | -0.89 (0.05)                    | -0.86 (0.03)  | >0.9999       | -0.84 (0.06)                    | -0.82 (0.04)  | >0.9999       | -0.95 (0.09)                    | -0.90 (0.06)  | >0.9999 |
|                        |                             | Early Dia. Rate (%/norm) | 1.27 (0.16)                     | 1.24 (0.12)   | >0.9999       | 1.32 (0.14)                     | 1.10 (0.15)   | 0.8797        | 1.00 (0.13)                     | 0.95 (0.13)   | >0.9999 |
| Posterior Free-Wall    | Anterior                    | Late Dia. Rate (%/norm)  | 1.01 (0.13)                     | 1.00 (0.05)   | >0.9999       | 0.84 (0.10)                     | 0.84 (0.03)   | >0.9999       | 0.87 (0.05)                     | 0.69 (0.08)   | 0.2789  |
|                        |                             | Peak Strain (%)          | -17.91 (0.75)                   | -16.98 (0.41) | 0.9386        | -16.61 (0.61)                   | -15.81 (0.43) | 0.9254        | -16.68 (0.64)                   | -14.36 (0.91) | 0.2008  |
|                        |                             | Systolic Rate (%/norm)   | -0.91 (0.06)                    | -0.92 (0.02)  | >0.9999       | -0.88 (0.05)                    | -0.87 (0.04)  | >0.9999       | -0.97 (0.08)                    | -0.93 (0.04)  | >0.9999 |
|                        | Septum                      | Early Dia. Rate (%/norm) | 1.44 (0.12)                     | 1.21 (0.11)   | 0.5872        | 1.43 (0.15)                     | 1.10 (0.09)   | 0.2647        | 1.05 (0.14)                     | 0.95 (0.12)   | >0.9999 |
|                        |                             | Late Dia. Rate (%/norm)  | 1.00 (0.15)                     | 0.91 (0.07)   | >0.9999       | 0.75 (0.08)                     | 0.77 (0.03)   | >0.9999       | 0.83 (0.05)                     | 0.67 (0.09)   | 0.5420  |
|                        |                             | Peak Strain (%)          | -18.75 (0.73)                   | -17.65 (0.63) | 0.8469        | -17.38 (0.71)                   | -16.34 (0.53) | 0.8142        | -17.29 (0.47)                   | -15.00 (1.03) | 0.2492  |
|                        | Posterior                   | Systolic Rate (%/norm)   | -0.98 (0.04)                    | -0.96 (0.01)  | >0.9999       | -0.96 (0.06)                    | -0.95 (0.05)  | >0.9999       | -1.03 (0.08)                    | -1.01 (0.04)  | >0.9999 |
|                        |                             | Early Dia. Rate (%/norm) | 1.49 (0.13)                     | 1.32 (0.11)   | >0.9999       | 1.56 (0.11)                     | 1.15 (0.13)   | 0.1198        | 1.09 (0.16)                     | 0.93 (0.11)   | >0.9999 |
|                        |                             | Late Dia. Rate (%/norm)  | 1.01 (0.14)                     | 1.03 (0.06)   | >0.9999       | 0.77 (0.10)                     | 0.89 (0.04)   | 0.8200        | 0.91 (0.04)                     | 0.70 (0.09)   | 0.2530  |
| Posterior Septum       | Peak Strain (%)             | -20.70 (0.95)            | -19.13 (0.70)                   | 0.6566        | -18.76 (0.77) | -18.06 (0.73)                   | >0.9999       | -18.68 (0.83) | -15.98 (1.22)                   | 0.3029        |         |
|                        | Systolic Rate (%/norm)      | -1.05 (0.04)             | -1.01 (0.02)                    | >0.9999       | -1.00 (0.06)  | -0.97 (0.06)                    | >0.9999       | -1.07 (0.07)  | -1.00 (0.05)                    | >0.9999       |         |
|                        | Early Dia. Rate (%/norm)    | 1.44 (0.14)              | 1.34 (0.15)                     | >0.9999       | 1.44 (0.13)   | 1.23 (0.16)                     | 0.9859        | 1.02 (0.16)   | 0.99 (0.14)                     | >0.9999       |         |
| Posterior Free-Wall    | Late Dia. Rate (%/norm)     | 1.19 (0.17)              | 1.14 (0.07)                     | >0.9999       | 1.01 (0.09)   | 1.01 (0.03)                     | >0.9999       | 0.98 (0.02)   | 0.75 (0.11)                     | 0.2633        |         |
|                        | Peak Strain (%)             | -20.90 (0.76)            | -20.10 (0.42)                   | >0.9999       | -19.34 (0.86) | -18.86 (0.60)                   | >0.9999       | -18.35 (0.65) | -16.50 (1.14)                   | 0.5852        |         |
|                        | Systolic Rate (%/norm)      | -1.03 (0.04)             | -1.00 (0.02)                    | >0.9999       | -0.98 (0.07)  | -0.94 (0.05)                    | >0.9999       | -1.07 (0.07)  | -1.01 (0.04)                    | >0.9999       |         |
| Posterior Free-Wall    | Early Dia. Rate (%/norm)    | 1.39 (0.12)              | 1.44 (0.13)                     | >0.9999       | 1.42 (0.15)   | 1.31 (0.13)                     | >0.9999       | 0.99 (0.16)   | 1.12 (0.15)                     | >0.9999       |         |
|                        | Late Dia. Rate (%/norm)     | 1.21 (0.15)              | 1.18 (0.07)                     | >0.9999       | 1.01 (0.10)   | 1.06 (0.05)                     | >0.9999       | 1.00 (0.07)   | 0.76 (0.10)                     | 0.2903        |         |



Supplemental Figure 3. Spatiotemporal circumferential strain maps derived from each 4DUS dataset, grouped by cohort (i.e., wild-type (left column) and *Nkx2-5*<sup>183P/+</sup> (right column)). Within each column, each row contains strain maps from the same mouse at 8, 12, and 16 weeks old, respectively.



Supplemental Figure 4. Spatiotemporal longitudinal strain maps derived from each 4DUS dataset, grouped by cohort (i.e., wild-type (left column) and *Nkx2-5*<sup>183P/+</sup> (right column)). Within each column, each row contains strain maps from the same mouse at 8, 12, and 16 weeks old, respectively.

## APPENDIX C. SUPPLEMENTAL DATA TO CHAPTER 5

Supplemental Table 3. Results of serial paired t-tests with Bonferroni-Dunn's multiple comparisons corrections on metrics derived using each of the three proposed machine learning models, compared to ground-truth values.

| METRIC                            | Mean of Ground Truth | Model 1 - Individual Z |            |         |                  | Model 2 - Combined Z |            |            |                  | Model 3 - Assisted |            |            |                  |
|-----------------------------------|----------------------|------------------------|------------|---------|------------------|----------------------|------------|------------|------------------|--------------------|------------|------------|------------------|
|                                   |                      | Model Mean             | Difference | Diff SE | Adjusted P Value | Model Mean           | Difference | Diff SE    | Adjusted P Value | Model Mean         | Difference | Diff SE    | Adjusted P Value |
| Total Volume - Max Value          | 45.19                | 44.64                  | 0.55       | 1.11    | >0.9999          | 44.80                | 0.39       | 1.14       | >0.9999          | 45.13              | 0.06       | 0.41       | >0.9999          |
| Total Volume - Min Value          | 22.52                | 21.17                  | 1.35       | 1.18    | >0.9999          | 21.47                | 1.05       | 1.15       | >0.9999          | 21.98              | 0.54       | 0.43       | >0.9999          |
| Total Volume - Abs Diff           | 22.67                | 23.47                  | -0.80      | 0.45    | >0.9999          | 23.32                | -0.65      | 0.43       | >0.9999          | 23.15              | -0.48      | 0.45       | >0.9999          |
| Total Volume - % Diff             | 56.21                | 55.42                  | 0.79       | 0.66    | >0.9999          | 55.64                | 0.56       | 0.62       | >0.9999          | 55.77              | 0.43       | 0.45       | >0.9999          |
| Total Volume - Sys1 Abs Rate      | -1.392               | -1.444                 | 0.052      | 0.032   | >0.9999          | -1.432               | 0.04012    | 0.03003    | >0.9999          | -1.413             | 0.02111    | 0.02872    | >0.9999          |
| Total Volume - Sys2 Abs Rate      | -1.207               | -1.251                 | 0.045      | 0.028   | >0.9999          | -1.238               | 0.03092    | 0.02632    | >0.9999          | -1.225             | 0.01786    | 0.02696    | >0.9999          |
| Total Volume - Dia1 Abs Rate      | 1.317                | 1.261                  | 0.057      | 0.040   | >0.9999          | 1.262                | 0.0556     | 0.03752    | >0.9999          | 1.248              | 0.06928    | 0.03633    | >0.9999          |
| Total Volume - Dia2 Abs Rate      | 0.9995               | 1.067                  | -0.068     | 0.024   | 0.4716           | 1.056                | -0.05687   | 0.02312    | >0.9999          | 1.047              | -0.04793   | 0.02249    | >0.9999          |
| Base Circ - Max Value             | 10.52                | 10.50                  | 0.02       | 0.08    | >0.9999          | 10.49                | 0.02       | 0.08       | >0.9999          | 10.48              | 0.04       | 0.05       | >0.9999          |
| Base Circ - Min Value             | 7.80                 | 7.78                   | 0.02       | 0.09    | >0.9999          | 7.79                 | 0.01       | 0.08       | >0.9999          | 7.79               | 0.01       | 0.05       | >0.9999          |
| Base Circ - Abs Diff              | 2.72                 | 2.72                   | 0.00       | 0.06    | >0.9999          | 2.70                 | 0.01       | 0.06       | >0.9999          | 2.69               | 0.03       | 0.05       | >0.9999          |
| Base Circ - Peak Strain: t=0      | -26.65               | -26.22                 | -0.44      | 0.57    | >0.9999          | -26.34               | -0.31      | 0.51       | >0.9999          | -26.35             | -0.31      | 0.39       | >0.9999          |
| Base Circ - Sys1 Strain Rate      | -0.01566             | -0.015                 | 0.000      | 0.000   | >0.9999          | -0.0157              | 0.00003753 | 0.0003756  | >0.9999          | -0.01568           | 0.00002078 | 0.0002656  | >0.9999          |
| Base Circ - Sys2 Strain Rate      | -0.01584             | -0.015                 | -0.001     | 0.000   | >0.9999          | -0.01533             | -0.0005063 | 0.0003668  | >0.9999          | -0.0153            | -0.0005422 | 0.0002836  | >0.9999          |
| Base Circ - Dia1 Strain Rate      | 0.01176              | 0.012                  | 0.000      | 0.000   | >0.9999          | 0.01144              | 0.000232   | 0.0004283  | >0.9999          | 0.01155            | 0.0002056  | 0.0003693  | >0.9999          |
| Base Circ - Dia2 Strain Rate      | 0.01143              | 0.011                  | 0.000      | 0.000   | >0.9999          | 0.01171              | -0.0002758 | 0.0002565  | >0.9999          | 0.01159            | -0.0001582 | 0.0002053  | >0.9999          |
| Mid-LV Circ - Max Value           | 9.99                 | 9.99                   | 0.00       | 0.09    | >0.9999          | 9.99                 | 0.00       | 0.08       | >0.9999          | 9.97               | 0.02       | 0.04       | >0.9999          |
| Mid-LV Circ - Min Value           | 6.99                 | 7.03                   | -0.04      | 0.10    | >0.9999          | 7.05                 | -0.06      | 0.09       | >0.9999          | 7.05               | -0.06      | 0.04       | >0.9999          |
| Mid-LV Circ - Abs Diff            | 3.00                 | 2.96                   | 0.04       | 0.06    | >0.9999          | 2.94                 | 0.06       | 0.05       | >0.9999          | 2.92               | 0.08       | 0.04       | >0.9999          |
| Mid-LV Circ - Peak Strain: t=0    | -31.02               | -29.98                 | -1.04      | 0.59    | >0.9999          | -30.07               | -0.95      | 0.51       | >0.9999          | -30.05             | -0.97      | 0.37       | 0.7887           |
| Mid-LV Circ - Sys1 Strain Rate    | -0.01777             | -0.017                 | 0.000      | 0.000   | >0.9999          | -0.01753             | -0.0001693 | 0.0003988  | >0.9999          | -0.01747           | -0.0002312 | 0.0002939  | >0.9999          |
| Mid-LV Circ - Sys2 Strain Rate    | -0.01712             | -0.016                 | -0.001     | 0.001   | >0.9999          | -0.01617             | -0.0009571 | 0.0004595  | >0.9999          | -0.01622           | -0.0008978 | 0.0003725  | >0.9999          |
| Mid-LV Circ - Dia1 Strain Rate    | 0.02073              | 0.018                  | 0.003      | 0.001   | 0.002            | 0.01808              | 0.002643   | 0.0006045  | 0.0019           | 0.01825            | 0.002479   | 0.0005224  | 0.0004           |
| Mid-LV Circ - Dia2 Strain Rate    | 0.01232              | 0.013                  | -0.001     | 0.000   | 0.2011           | 0.01317              | -0.0008534 | 0.000278   | 0.2072           | 0.01306            | -0.0007392 | 0.0002126  | 0.0545           |
| Apex Circ - Max Value             | 5.91                 | 5.84                   | 0.07       | 0.06    | >0.9999          | 5.83                 | 0.08       | 0.06       | >0.9999          | 5.82               | 0.09       | 0.03       | 0.1257           |
| Apex Circ - Min Value             | 3.96                 | 3.98                   | -0.02      | 0.07    | >0.9999          | 3.99                 | -0.03      | 0.07       | >0.9999          | 3.99               | -0.03      | 0.03       | >0.9999          |
| Apex Circ - Abs Diff              | 1.95                 | 1.86                   | 0.09       | 0.04    | 0.7581           | 1.84                 | 0.11       | 0.04       | 0.2639           | 1.83               | 0.12       | 0.03       | 0.0474           |
| Apex Circ - Peak Strain: t=0      | -33.59               | -31.94                 | -1.65      | 0.61    | 0.6168           | -32.12               | -1.47      | 0.59       | >0.9999          | -32.16             | -1.44      | 0.50       | 0.3831           |
| Apex Circ - Sys1 Strain Rate      | -0.01701             | -0.017                 | 0.000      | 0.000   | >0.9999          | -0.01733             | 0.0003111  | 0.0004488  | >0.9999          | -0.01734           | 0.0003203  | 0.0003562  | >0.9999          |
| Apex Circ - Sys2 Strain Rate      | -0.01601             | -0.014                 | -0.002     | 0.001   | 0.0278           | -0.01396             | -0.002047  | 0.0005216  | 0.011            | -0.01409           | -0.001912  | 0.0004501  | 0.0032           |
| Apex Circ - Dia1 Strain Rate      | 0.02501              | 0.021                  | 0.004      | 0.001   | 0.0009           | 0.02156              | 0.003456   | 0.00077    | 0.0012           | 0.02169            | 0.003322   | 0.0007418  | 0.0013           |
| Apex Circ - Dia2 Strain Rate      | 0.01289              | 0.013                  | 0.000      | 0.000   | >0.9999          | 0.01401              | -0.001112  | 0.0004093  | 0.5972           | 0.01386            | -0.0009657 | 0.0003371  | 0.3873           |
| Ant-FW Long - Max Value           | 7.15                 | 7.15                   | 0.00       | 0.01    | >0.9999          | 7.13                 | 0.01       | 0.01       | >0.9999          | 7.13               | 0.01       | 0.00       | 0.0281           |
| Ant-FW Long - Min Value           | 6.02                 | 6.04                   | -0.02      | 0.01    | >0.9999          | 6.02                 | 0.00       | 0.01       | >0.9999          | 6.02               | 0.00       | 0.00       | >0.9999          |
| Ant-FW Long - Abs Diff            | 1.13                 | 1.11                   | 0.01       | 0.01    | 0.9804           | 1.11                 | 0.01       | 0.00       | 0.687            | 1.11               | 0.01       | 0.00       | 0.4225           |
| Ant-FW Long - Peak Strain: t=0    | -16.07               | -15.82                 | -0.25      | 0.07    | 0.0851           | -15.86               | -0.2058    | 0.06895    | 0.269            | -15.89             | -0.1796    | 0.0701     | 0.1608           |
| Ant-FW Long - Sys1 Strain Rate    | -0.008878            | -0.009                 | 0.000      | 0.000   | >0.9999          | -0.008898            | 0.00001992 | 0.00005465 | >0.9999          | -0.008924          | 0.00004568 | 0.00004802 | >0.9999          |
| Ant-FW Long - Sys2 Strain Rate    | -0.008687            | -0.009                 | 0.000      | 0.000   | >0.9999          | -0.008814            | 0.0001268  | 0.00006996 | >0.9999          | -0.00877           | 0.00008353 | 0.00006649 | >0.9999          |
| Ant-FW Long - Dia1 Strain Rate    | 0.01053              | 0.010                  | 0.001      | 0.000   | <0.0001          | 0.009987             | 0.0005724  | 0.00009943 | <0.0001          | 0.01002            | 0.0005133  | 0.00008419 | <0.0001          |
| Ant-FW Long - Dia2 Strain Rate    | 0.006801             | 0.007                  | 0.000      | 0.000   | >0.9999          | 0.006865             | -6.372E-05 | 0.00006647 | >0.9999          | 0.006858           | -0.0000569 | 0.00004921 | >0.9999          |
| Anterior Long - Max Value         | 7.16                 | 7.17                   | 0.00       | 0.01    | >0.9999          | 7.15                 | 0.01       | 0.01       | >0.9999          | 7.15               | 0.01       | 0.00       | 0.5501           |
| Anterior Long - Min Value         | 6.09                 | 6.11                   | -0.01      | 0.01    | >0.9999          | 6.09                 | 0.00       | 0.01       | >0.9999          | 6.09               | 0.00       | 0.00       | >0.9999          |
| Anterior Long - Abs Diff          | 1.07                 | 1.06                   | 0.01       | 0.01    | >0.9999          | 1.06                 | 0.01       | 0.01       | >0.9999          | 1.06               | 0.01       | 0.00       | >0.9999          |
| Anterior Long - Peak Strain: t=0  | -15.20               | -15.03                 | -0.18      | 0.08    | >0.9999          | -15.08               | -0.12      | 0.08       | >0.9999          | -15.11             | -0.09      | 0.07       | >0.9999          |
| Anterior Long - Sys1 Strain Rate  | -0.008588            | -0.009                 | 0.000      | 0.000   | >0.9999          | -0.008653            | 0.00006477 | 0.00005413 | >0.9999          | -0.008668          | 0.00007981 | 0.00005002 | >0.9999          |
| Anterior Long - Sys2 Strain Rate  | -0.00834             | -0.008                 | 0.000      | 0.000   | >0.9999          | -0.008486            | 0.0001467  | 0.00006195 | >0.9999          | -0.008466          | 0.0001261  | 0.00005887 | >0.9999          |
| Anterior Long - Dia1 Strain Rate  | 0.01045              | 0.010                  | 0.001      | 0.000   | <0.0001          | 0.009875             | 0.0005724  | 0.00009943 | <0.0001          | 0.009883           | 0.0005638  | 0.00009728 | <0.0001          |
| Anterior Long - Dia2 Strain Rate  | 0.006197             | 0.006                  | 0.000      | 0.000   | 0.2489           | 0.006434             | -0.0002368 | 0.00007577 | 0.174            | 0.006445           | -0.0002473 | 0.00006836 | 0.0335           |
| Ant-Sep Long - Max Value          | 7.19                 | 7.19                   | 0.00       | 0.01    | >0.9999          | 7.17                 | 0.01       | 0.01       | >0.9999          | 7.17               | 0.01       | 0.00       | >0.9999          |
| Ant-Sep Long - Min Value          | 6.09                 | 6.10                   | -0.01      | 0.01    | >0.9999          | 6.08                 | 0.00       | 0.01       | >0.9999          | 6.08               | 0.00       | 0.01       | >0.9999          |
| Ant-Sep Long - Abs Diff           | 1.10                 | 1.09                   | 0.01       | 0.01    | >0.9999          | 1.09                 | 0.01       | 0.01       | >0.9999          | 1.09               | 0.01       | 0.01       | >0.9999          |
| Ant-Sep Long - Peak Strain: t=0   | -15.59               | -15.40                 | -0.20      | 0.08    | >0.9999          | -15.45               | -0.15      | 0.08       | >0.9999          | -15.47             | -0.12      | 0.07       | >0.9999          |
| Ant-Sep Long - Sys1 Strain Rate   | -0.009165            | -0.009                 | 0.000      | 0.000   | >0.9999          | -0.009191            | 0.00002607 | 0.00006611 | >0.9999          | -0.009193          | 0.00002278 | 0.00006109 | >0.9999          |
| Ant-Sep Long - Sys2 Strain Rate   | -0.008717            | -0.009                 | 0.000      | 0.000   | >0.9999          | -0.008763            | 0.00004583 | 0.00006165 | >0.9999          | -0.008739          | 0.00002237 | 0.00005606 | >0.9999          |
| Ant-Sep Long - Dia1 Strain Rate   | 0.0106               | 0.010                  | 0.001      | 0.000   | <0.0001          | 0.01003              | 0.0005769  | 0.0001104  | <0.0001          | 0.0101             | 0.0005027  | 0.0001051  | 0.0004           |
| Ant-Sep Long - Dia2 Strain Rate   | 0.006318             | 0.007                  | 0.000      | 0.000   | 0.0149           | 0.006587             | -0.0002699 | 0.00006849 | 0.0109           | 0.006525           | -0.0002065 | 0.00005517 | 0.0214           |
| Post-Sep Long - Max Value         | 7.22                 | 7.22                   | -0.01      | 0.01    | >0.9999          | 7.20                 | 0.01       | 0.01       | >0.9999          | 7.20               | 0.01       | 0.01       | >0.9999          |
| Post-Sep Long - Min Value         | 6.03                 | 6.04                   | -0.01      | 0.01    | >0.9999          | 6.02                 | 0.00       | 0.01       | >0.9999          | 6.02               | 0.00       | 0.01       | >0.9999          |
| Post-Sep Long - Abs Diff          | 1.19                 | 1.18                   | 0.01       | 0.01    | >0.9999          | 1.18                 | 0.01       | 0.01       | >0.9999          | 1.18               | 0.01       | 0.01       | >0.9999          |
| Post-Sep Long - Peak Strain: t=0  | -16.80               | -16.60                 | -0.20      | 0.08    | >0.9999          | -16.63               | -0.16      | 0.08       | >0.9999          | -16.65             | -0.15      | 0.07       | >0.9999          |
| Post-Sep Long - Sys1 Strain Rate  | -0.009803            | -0.010                 | 0.000      | 0.000   | >0.9999          | -0.009849            | 0.00004578 | 0.00006989 | >0.9999          | -0.009853          | 0.00005    | 0.00006349 | >0.9999          |
| Post-Sep Long - Sys2 Strain Rate  | -0.009404            | -0.009                 | 0.000      | 0.000   | >0.9999          | -0.009398            | -5.711E-06 | 0.0000758  | >0.9999          | -0.009367          | -3.693E-05 | 0.00007261 | >0.9999          |
| Post-Sep Long - Dia1 Strain Rate  | 0.01065              | 0.010                  | 0.000      | 0.000   | 0.0049           | 0.01032              | 0.0003271  | 0.0000912  | 0.0374           | 0.01034            | 0.0003051  | 0.00009028 | 0.076            |
| Post-Sep Long - Dia2 Strain Rate  | 0.00723              | 0.007                  | 0.000      | 0.000   | >0.9999          | 0.007339             | -0.0001091 | 0.00006446 | >0.9999          | 0.007346           | -0.0001158 | 0.00006007 | >0.9999          |
| Posterior Long - Max Value        | 7.17                 | 7.18                   | -0.01      | 0.01    | >0.9999          | 7.15                 | 0.01       | 0.01       | >0.9999          | 7.15               | 0.01       | 0.01       | >0.9999          |
| Posterior Long - Min Value        | 5.93                 | 5.95                   | -0.02      | 0.01    | >0.9999          | 5.93                 | 0.00       | 0.01       | >0.9999          | 5.93               | 0.00       | 0.01       | >0.9999          |
| Posterior Long - Abs Diff         | 1.24                 | 1.23                   | 0.01       | 0.01    | >0.9999          | 1.23                 | 0.01       | 0.01       | >0.9999          | 1.23               | 0.01       | 0.01       | >0.9999          |
| Posterior Long - Peak Strain: t=0 | -17.61               | -17.42                 | -0.19      | 0.08    | >0.9999          | -17.44               | -0.17      | 0.08       | >0.9999          | -17.45             | -0.16      | 0.08       | >0.9999          |
| Posterior Long - Sys1 Strain Rate | -0.009645            | -0.010                 | 0.000      | 0.000   | >0.9999          | -0.009707            | 0.00006124 | 0.00006495 | >0.9999          | -0.009694          | 0.0000489  | 0.00005749 | >0.9999          |
| Posterior Long - Sys2 Strain Rate | -0.009661            | -0.010                 | 0.000      | 0.000   | >0.9999          | -0.009676            | 0.00001559 | 0.0000696  | >0.9999          | -0.009674          | 0.00001333 | 0.00006549 | >0.9999          |
| Posterior Long - Dia1 Strain Rate | 0.01098              | 0.011                  | 0.000      | 0.000   | 0.0003           | 0.01061              | 0.0003676  | 0.00007653 | 0.0003           | 0.01062            | 0.0003548  | 0.00007554 | 0.0005           |
| Posterior Long - Dia2 Strain Rate | 0.007689             | 0.008                  | 0.000      | 0.000   | >0.9999          | 0.007726             | -3.673E-05 | 0.00006829 | >0.9999          | 0.00773            | -4.074E-05 | 0.00006655 | >0.9999          |
| Post-FW Long - Max Value          | 7.13                 | 7.13                   | -0.01      | 0.01    | >0.9999          | 7.11                 | 0.01       | 0.01       | >0.9999          | 7.11               | 0.01       | 0.01       | >0.9999          |
| Post-FW Long - Min Value          | 5.92                 | 5.94                   | -0.02      | 0.01    | >0.9999          | 5.92                 | 0.00       | 0.01       | >0.9999          | 5.92               | 0.00       | 0.01       | >0.9999          |
| Post-FW Long -                    |                      |                        |            |         |                  |                      |            |            |                  |                    |            |            |                  |

## REFERENCES

- [1] S. S. Virani *et al.*, "Heart Disease and Stroke Statistics-2021 Update: A Report From the American Heart Association," *Circulation*, vol. 143, no. 8, pp. e254-e743, Feb 23 2021, doi: 10.1161/CIR.0000000000000950.
- [2] P. A. Heidenreich *et al.*, "Forecasting the impact of heart failure in the United States: a policy statement from the American Heart Association," *Circ Heart Fail*, vol. 6, no. 3, pp. 606-19, May 2013, doi: 10.1161/HHF.0b013e318291329a.
- [3] W. D. Rosamond and A. Johnson, "Trends in Heart Failure Incidence in the Community: A Gathering Storm," *Circulation*, vol. 135, no. 13, pp. 1224-1226, Mar 28 2017, doi: 10.1161/CIRCULATIONAHA.117.027472.
- [4] M. P. St-Onge *et al.*, "Meal Timing and Frequency: Implications for Cardiovascular Disease Prevention: A Scientific Statement From the American Heart Association," *Circulation*, vol. 135, no. 9, pp. e96-e121, Feb 28 2017, doi: 10.1161/CIR.0000000000000476.
- [5] R. D. Patten and M. R. Hall-Porter, "Small animal models of heart failure: development of novel therapies, past and present," *Circ Heart Fail*, vol. 2, no. 2, pp. 138-44, Mar 2009, doi: 10.1161/CIRCHEARTFAILURE.108.839761.
- [6] B. K. McConnell *et al.*, "Comparison of two murine models of familial hypertrophic cardiomyopathy," *Circ Res*, vol. 88, no. 4, pp. 383-9, Mar 02 2001. [Online]. Available: <https://www.ncbi.nlm.nih.gov/pubmed/11230104>.
- [7] J. Chen, D. K. Ceholski, L. Liang, K. Fish, and R. J. Hajjar, "Variability in coronary artery anatomy affects consistency of cardiac damage after myocardial infarction in mice," *Am J Physiol Heart Circ Physiol*, vol. 313, no. 2, pp. H275-H282, Aug 1 2017, doi: 10.1152/ajpheart.00127.2017.
- [8] I. Muthuramu, M. Lox, F. Jacobs, and B. De Geest, "Permanent ligation of the left anterior descending coronary artery in mice: a model of post-myocardial infarction remodelling and heart failure," *J Vis Exp*, no. 94, Dec 2 2014, doi: 10.3791/52206.
- [9] J. F. James, T. E. Hewett, and J. Robbins, "Cardiac physiology in transgenic mice," *Circ Res*, vol. 82, no. 4, pp. 407-15, Mar 09 1998. [Online]. Available: <https://www.ncbi.nlm.nih.gov/pubmed/9506700>.
- [10] R. M. Lang *et al.*, "Recommendations for Cardiac Chamber Quantification by Echocardiography in Adults: An Update from the American Society of Echocardiography and the European Association of Cardiovascular Imaging," (in English), *J Am Soc Echocardiogr*, vol. 28, no. 1, pp. 1-U170, Jan 2015, doi: 10.1016/j.echo.2014.10.003.

- [11] R. M. Lang *et al.*, "Recommendations for chamber quantification: A report from the American Society of Echocardiography's guidelines and standards committee and the chamber quantification writing group, developed in conjunction with the European Association of Echocardiography, a branch of the European Society of Cardiology," (in English), *J Am Soc Echocardiog*, vol. 18, no. 12, pp. 1440-1463, Dec 2005, doi: 10.1016/j.echo.2005.10.005.
- [12] K. K. Shung, "High Frequency Ultrasonic Imaging," *J Med Ultrasound*, vol. 17, no. 1, pp. 25-30, 2009, doi: 10.1016/S0929-6441(09)60012-6.
- [13] P. A. Doevendans, M. J. Daemen, E. D. de Muinck, and J. F. Smits, "Cardiovascular phenotyping in mice," *Cardiovasc Res*, vol. 39, no. 1, pp. 34-49, Jul 1998. [Online]. Available: <https://www.ncbi.nlm.nih.gov/pubmed/9764188>.
- [14] C. J. Hartley, G. E. Taffet, A. K. Reddy, M. L. Entman, and L. H. Michael, "Noninvasive cardiovascular phenotyping in mice," *ILAR J*, vol. 43, no. 3, pp. 147-58, 2002. [Online]. Available: <https://www.ncbi.nlm.nih.gov/pubmed/12105382>.
- [15] M. Bauer *et al.*, "Echocardiographic speckle-tracking based strain imaging for rapid cardiovascular phenotyping in mice," *Circ Res*, vol. 108, no. 8, pp. 908-16, Apr 15 2011, doi: 10.1161/CIRCRESAHA.110.239574.
- [16] N. B. Schiller and E. Foster, "Analysis of left ventricular systolic function," *Heart*, vol. 75, no. 6 Suppl 2, pp. 17-26, Jun 1996. [Online]. Available: <https://www.ncbi.nlm.nih.gov/pubmed/8785699>.
- [17] J. M. Gardin, F. M. Siri, R. N. Kitsis, J. G. Edwards, and L. A. Leinwand, "Echocardiographic assessment of left ventricular mass and systolic function in mice," *Circ Res*, vol. 76, no. 5, pp. 907-14, May 1995. [Online]. Available: <https://www.ncbi.nlm.nih.gov/pubmed/7729009>.
- [18] A. Pistner, S. Belmonte, T. Coulthard, and B. Blaxall, "Murine echocardiography and ultrasound imaging," *J Vis Exp*, no. 42, Aug 08 2010, doi: 10.3791/2100.
- [19] T. Shiota, "3D echocardiography: the present and the future," *J Cardiol*, vol. 52, no. 3, pp. 169-85, Dec 2008, doi: 10.1016/j.jjcc.2008.09.004.
- [20] M. J. Monaghan, "Role of real time 3D echocardiography in evaluating the left ventricle," *Heart*, vol. 92, no. 1, pp. 131-6, Jan 2006, doi: 10.1136/hrt.2004.058388.
- [21] X. X. Luo, F. Fang, H. K. So, C. Liu, M. C. Yam, and A. P. Lee, "Automated left heart chamber volumetric assessment using three-dimensional echocardiography in Chinese adolescents," *Echo Res Pract*, vol. 4, no. 4, pp. 53-61, Dec 2017, doi: 10.1530/ERP-17-0028.

- [22] F. M. Abdel Aziz, S. M. Abdel Dayem, R. I. Ismail, H. Hassan, and A. M. Fattouh, "Assessment of Left Ventricular Volume and Function Using Real-Time 3D Echocardiography versus Angiocardiography in Children with Tetralogy of Fallot," *J Cardiovasc Ultrasound*, vol. 24, no. 2, pp. 123-7, Jun 2016, doi: 10.4250/jcu.2016.24.2.123.
- [23] A. Akki, A. Gupta, and R. G. Weiss, "Magnetic resonance imaging and spectroscopy of the murine cardiovascular system," *Am J Physiol-Heart C*, vol. 304, no. 5, pp. H633-48, Mar 01 2013, doi: 10.1152/ajpheart.00771.2011.
- [24] F. Franco, S. K. Dubois, R. M. Peshock, and R. V. Shohet, "Magnetic resonance imaging accurately estimates LV mass in a transgenic mouse model of cardiac hypertrophy," *Am J Physiol*, vol. 274, no. 2 Pt 2, pp. H679-83, Feb 1998. [Online]. Available: <https://www.ncbi.nlm.nih.gov/pubmed/9486274>.
- [25] F. Kober, I. Iltis, P. J. Cozzone, and M. Bernard, "Cine-MRI assessment of cardiac function in mice anesthetized with ketamine/xylazine and isoflurane," (in English), *Magn Reson Mater Phy*, vol. 17, no. 3-6, pp. 157-161, Dec 2004, doi: 10.1007/s10334-004-0086-0.
- [26] M. Nahrendorf *et al.*, "Cardiac remodelling in mice after myocardial infarction followed by serial Cine MRI," (in English), *Eur Heart J*, vol. 23, pp. 202-202, Aug-Sep 2002. [Online]. Available: <Go to ISI>://WOS:000179753300764.
- [27] S. E. Slawson, B. B. Roman, D. S. Williams, and A. P. Koretsky, "Cardiac MRI of the normal and hypertrophied mouse heart," (in English), *Magn Reson Med*, vol. 39, no. 6, pp. 980-987, Jun 1998, doi: DOI 10.1002/mrm.1910390616.
- [28] F. Wiesmann, J. Ruff, K. H. Hiller, E. Rommel, A. Haase, and S. Neubauer, "Developmental changes of cardiac function and mass assessed with MRI in neonatal, juvenile, and adult mice," *Am J Physiol Heart Circ Physiol*, vol. 278, no. 2, pp. H652-7, Feb 2000. [Online]. Available: <https://www.ncbi.nlm.nih.gov/pubmed/10666098>.
- [29] F. W. Damen *et al.*, "High-Frequency 4-Dimensional Ultrasound (4DUS): A Reliable Method for Assessing Murine Cardiac Function," *Tomography*, vol. 3, no. 4, pp. 180-187, Dec 2017, doi: 10.18383/j.tom.2017.00016.
- [30] A. H. Soepriatna, F. W. Damen, P. P. Vlachos, and C. J. Goergen, "Cardiac and respiratory-gated volumetric murine ultrasound," *Int J Cardiovasc Imaging*, vol. 34, no. 5, pp. 713-724, May 2018, doi: 10.1007/s10554-017-1283-z.
- [31] B. J. Maron *et al.*, "Contemporary definitions and classification of the cardiomyopathies: an American Heart Association Scientific Statement from the Council on Clinical Cardiology, Heart Failure and Transplantation Committee; Quality of Care and Outcomes Research and Functional Genomics and Translational Biology Interdisciplinary Working Groups; and Council on Epidemiology and Prevention," *Circulation*, vol. 113, no. 14, pp. 1807-16, Apr 11 2006, doi: 10.1161/CIRCULATIONAHA.106.174287.

- [32] J. A. Towbin *et al.*, "Incidence, causes, and outcomes of dilated cardiomyopathy in children," (in English), *Jama-J Am Med Assoc*, vol. 296, no. 15, pp. 1867-1876, Oct 18 2006, doi: DOI 10.1001/jama.296.15.1867.
- [33] E. J. Benjamin *et al.*, "Heart Disease and Stroke Statistics-2017 Update: A Report From the American Heart Association," *Circulation*, vol. 135, no. 10, pp. e146-e603, Mar 7 2017, doi: 10.1161/CIR.0000000000000485.
- [34] V. Kumar, A. K. Abbas, and J. C. Aster, *Robbins and Cotran pathologic basis of disease*, Ninth edition. ed. Philadelphia, PA: Elsevier/Saunders, 2015, pp. xvi, 1391 pages.
- [35] A. A. Wilde and E. R. Behr, "Genetic testing for inherited cardiac disease," *Nat Rev Cardiol*, vol. 10, no. 10, pp. 571-83, Oct 2013, doi: 10.1038/nrcardio.2013.108.
- [36] K. Thygesen *et al.*, "Third universal definition of myocardial infarction," *J Am Coll Cardiol*, vol. 60, no. 16, pp. 1581-98, Oct 16 2012, doi: 10.1016/j.jacc.2012.08.001.
- [37] C. Semsarian, J. Ingles, M. S. Maron, and B. J. Maron, "New perspectives on the prevalence of hypertrophic cardiomyopathy," *J Am Coll Cardiol*, vol. 65, no. 12, pp. 1249-54, Mar 31 2015, doi: 10.1016/j.jacc.2015.01.019.
- [38] T. Rowland, "Sudden unexpected death in young athletes: reconsidering "hypertrophic cardiomyopathy"," *Pediatrics*, vol. 123, no. 4, pp. 1217-22, Apr 2009, doi: 10.1542/peds.2008-0708.
- [39] A. Kumar *et al.*, "Rescue of cardiac alpha-actin deficient mice by enteric smooth muscle gamma-actin," (in English), *Mol Biol Cell*, vol. 7, pp. 2186-2186, Dec 1996. [Online]. Available: <Go to ISI>://WOS:A1996WB01802183.
- [40] P. Richardson *et al.*, "Report of the 1995 World Health Organization/International Society and Federation of Cardiology Task Force on the Definition and Classification of cardiomyopathies," *Circulation*, vol. 93, no. 5, pp. 841-2, Mar 01 1996. [Online]. Available: <https://www.ncbi.nlm.nih.gov/pubmed/8598070>.
- [41] J. Ross, Jr., "Dilated cardiomyopathy: concepts derived from gene deficient and transgenic animal models," *Circ J*, vol. 66, no. 3, pp. 219-24, Mar 2002. [Online]. Available: <https://www.ncbi.nlm.nih.gov/pubmed/11922267>.
- [42] F. Sheikh and J. Chen, "Mouse models for cardiomyopathy research," *Prog Pediatr Cardiol*, vol. 24, no. 1, pp. 27-34, 2007.
- [43] S. Arber *et al.*, "MLP-deficient mice exhibit a disruption of cardiac cytoarchitectural organization, dilated cardiomyopathy, and heart failure," *Cell*, vol. 88, no. 3, pp. 393-403, Feb 07 1997. [Online]. Available: <https://www.ncbi.nlm.nih.gov/pubmed/9039266>.

- [44] H. Cheng *et al.*, "Selective deletion of long but not short Cypher isoforms leads to late-onset dilated cardiomyopathy," *Hum Mol Genet*, vol. 20, no. 9, pp. 1751-1762, 2011, doi: 10.1093/hmg/ddr050.
- [45] M. Zheng *et al.*, "Cardiac-specific ablation of Cypher leads to a severe form of dilated cardiomyopathy with premature death," (in English), *Hum Mol Genet*, vol. 18, no. 4, pp. 701-713, Feb 15 2009, doi: 10.1093/hmg/ddn400.
- [46] G. Danialou *et al.*, "Dystrophin-deficient cardiomyocytes are abnormally vulnerable to mechanical stress-induced contractile failure and injury," (in English), *Faseb J*, vol. 15, no. 7, pp. 1655-+, May 29 2001, doi: 10.1096/fj.01-0030fje.
- [47] W. Li, W. Liu, J. Zhong, and X. Yu, "Early manifestation of alteration in cardiac function in dystrophin deficient mdx mouse using 3D CMR tagging," (in English), *J Cardiovasc Magn R*, vol. 11, Oct 22 2009, doi: 10.1186/1532-429x-11-40.
- [48] R. M. Grady, H. B. Teng, M. C. Nichol, J. C. Cunningham, R. S. Wilkinson, and J. R. Sanes, "Skeletal and cardiac myopathies in mice lacking utrophin and dystrophin: A model for Duchenne muscular dystrophy," (in English), *Cell*, vol. 90, no. 4, pp. 729-738, Aug 22 1997, doi: Doi 10.1016/S0092-8674(00)80533-4.
- [49] A. E. Deconinck *et al.*, "Utrophin-dystrophin-deficient mice as a model for Duchenne muscular dystrophy," (in English), *Cell*, vol. 90, no. 4, pp. 717-727, Aug 22 1997, doi: Doi 10.1016/S0092-8674(00)80532-2.
- [50] G. Bulfield, W. G. Siller, P. A. L. Wight, and K. J. Moore, "X-Chromosome-Linked Muscular-Dystrophy (Mdx) in the Mouse," (in English), *P Natl Acad Sci-Biol*, vol. 81, no. 4, pp. 1189-1192, 1984, doi: DOI 10.1073/pnas.81.4.1189.
- [51] H. Toko *et al.*, "Ca<sup>2+</sup>/Calmodulin-Dependent Kinase II delta Causes Heart Failure by Accumulation of p53 in Dilated Cardiomyopathy," (in English), *Circulation*, vol. 122, no. 9, pp. 891-899, Aug 31 2010, doi: 10.1161/Circulationaha.109.935296.
- [52] V. Nikolova *et al.*, "Defects in nuclear structure and function promote dilated cardiomyopathy in lamin A/C-deficient mice," (in English), *Journal of Clinical Investigation*, vol. 113, no. 3, pp. 357-369, Feb 2004, doi: 10.1172/Jci200419448.
- [53] R. Knoll *et al.*, "The cardiac mechanical stretch sensor machinery involves a Z disc complex that is defective in a subset of human dilated cardiomyopathy," (in English), *Cell*, vol. 111, no. 7, pp. 943-955, Dec 27 2002, doi: Doi 10.1016/S0092-8674(02)01226-6.
- [54] C. Muhl, W. R. Dassen, and H. Kuipers, "Cardiac remodelling: concentric versus eccentric hypertrophy in strength and endurance athletes," *Neth Heart J*, vol. 16, no. 4, pp. 129-33, Apr 2008. [Online]. Available: <https://www.ncbi.nlm.nih.gov/pubmed/18427637>.

- [55] V. Rai, P. Sharma, S. Agrawal, and D. K. Agrawal, "Relevance of mouse models of cardiac fibrosis and hypertrophy in cardiac research," *Mol Cell Biochem*, vol. 424, no. 1-2, pp. 123-145, Jan 2017, doi: 10.1007/s11010-016-2849-0.
- [56] A. Maass and L. A. Leinwand, "Animal models of hypertrophic cardiomyopathy," *Curr Opin Cardiol*, vol. 15, no. 3, pp. 189-96, May 2000. [Online]. Available: <https://www.ncbi.nlm.nih.gov/pubmed/10952427>.
- [57] C. Zaragoza *et al.*, "Animal models of cardiovascular diseases," *J Biomed Biotechnol*, vol. 2011, p. 497841, 2011, doi: 10.1155/2011/497841.
- [58] C. R. Bezzina, N. Lahrouchi, and S. G. Priori, "Genetics of sudden cardiac death," *Circ Res*, vol. 116, no. 12, pp. 1919-36, Jun 05 2015, doi: 10.1161/CIRCRESAHA.116.304030.
- [59] A. C. deAlmeida, R. J. van Oort, and X. H. Wehrens, "Transverse aortic constriction in mice," *J Vis Exp*, no. 38, Apr 21 2010, doi: 10.3791/1729.
- [60] A. M. Zaw, C. M. Williams, H. K. Law, and B. K. Chow, "Minimally Invasive Transverse Aortic Constriction in Mice," *J Vis Exp*, no. 121, Mar 14 2017, doi: 10.3791/55293.
- [61] P. Hu, D. Zhang, L. Swenson, G. Chakrabarti, E. D. Abel, and S. E. Litwin, "Minimally invasive aortic banding in mice: effects of altered cardiomyocyte insulin signaling during pressure overload," *Am J Physiol Heart Circ Physiol*, vol. 285, no. 3, pp. H1261-9, Sep 2003, doi: 10.1152/ajpheart.00108.2003.
- [62] A. Nakamura *et al.*, "LV systolic performance improves with development of hypertrophy after transverse aortic constriction in mice," *Am J Physiol Heart Circ Physiol*, vol. 281, no. 3, pp. H1104-12, Sep 2001. [Online]. Available: <https://www.ncbi.nlm.nih.gov/pubmed/11514276>.
- [63] T. Furihata *et al.*, "The experimental model of transition from compensated cardiac hypertrophy to failure created by transverse aortic constriction in mice," *Int J Cardiol Heart Vasc*, vol. 11, pp. 24-28, Jun 2016, doi: 10.1016/j.ijcha.2016.03.007.
- [64] R. J. van Oort *et al.*, "Accelerated development of pressure overload-induced cardiac hypertrophy and dysfunction in an RyR2-R176Q knockin mouse model," *Hypertension*, vol. 55, no. 4, pp. 932-8, Apr 2010, doi: 10.1161/HYPERTENSIONAHA.109.146449.
- [65] Z. Arany, M. Novikov, S. Chin, Y. Ma, A. Rosenzweig, and B. M. Spiegelman, "Transverse aortic constriction leads to accelerated heart failure in mice lacking PPAR-gamma coactivator 1alpha," *Proc Natl Acad Sci U S A*, vol. 103, no. 26, pp. 10086-91, Jun 27 2006, doi: 10.1073/pnas.0603615103.

- [66] H. A. Rockman, S. P. Wachhorst, L. Mao, and J. Ross, Jr., "ANG II receptor blockade prevents ventricular hypertrophy and ANF gene expression with pressure overload in mice," *Am J Physiol*, vol. 266, no. 6 Pt 2, pp. H2468-75, Jun 1994. [Online]. Available: <https://www.ncbi.nlm.nih.gov/pubmed/8024008>.
- [67] C. J. Barrick *et al.*, "Parent-of-origin effects on cardiac response to pressure overload in mice," *Am J Physiol Heart Circ Physiol*, vol. 297, no. 3, pp. H1003-9, Sep 2009, doi: 10.1152/ajpheart.00896.2008.
- [68] C. J. Barrick, M. Rojas, R. Schoonhoven, S. S. Smyth, and D. W. Threadgill, "Cardiac response to pressure overload in 129S1/SvImJ and C57BL/6J mice: temporal- and background-dependent development of concentric left ventricular hypertrophy," *Am J Physiol Heart Circ Physiol*, vol. 292, no. 5, pp. H2119-30, May 2007, doi: 10.1152/ajpheart.00816.2006.
- [69] C. F. Deschepper, J. L. Olson, M. Otis, and N. Gallo-Payet, "Characterization of blood pressure and morphological traits in cardiovascular-related organs in 13 different inbred mouse strains," *J Appl Physiol (1985)*, vol. 97, no. 1, pp. 369-76, Jul 2004, doi: 10.1152/jappphysiol.00073.2004.
- [70] C. A. Lygate *et al.*, "Serial high resolution 3D-MRI after aortic banding in mice: band internalization is a source of variability in the hypertrophic response," *Basic Res Cardiol*, vol. 101, no. 1, pp. 8-16, Jan 2006, doi: 10.1007/s00395-005-0546-3.
- [71] A. A. Geisterfer-Lowrance *et al.*, "A mouse model of familial hypertrophic cardiomyopathy," *Science*, vol. 272, no. 5262, pp. 731-4, May 03 1996. [Online]. Available: <https://www.ncbi.nlm.nih.gov/pubmed/8614836>.
- [72] W. Zhao *et al.*, "A Murine Hypertrophic Cardiomyopathy Model: The DBA/2J Strain," *PLoS One*, vol. 10, no. 8, p. e0133132, 2015, doi: 10.1371/journal.pone.0133132.
- [73] L. Carrier *et al.*, "Asymmetric septal hypertrophy in heterozygous cMyBP-C null mice," *Cardiovasc Res*, vol. 63, no. 2, pp. 293-304, Aug 01 2004, doi: 10.1016/j.cardiores.2004.04.009.
- [74] Q. Yang, A. Sanbe, H. Osinska, T. E. Hewett, R. Klevitsky, and J. Robbins, "A mouse model of myosin binding protein C human familial hypertrophic cardiomyopathy," *J Clin Invest*, vol. 102, no. 7, pp. 1292-300, Oct 01 1998, doi: 10.1172/JCI3880.
- [75] J. C. Tardiff *et al.*, "A truncated cardiac troponin T molecule in transgenic mice suggests multiple cellular mechanisms for familial hypertrophic cardiomyopathy," *J Clin Invest*, vol. 101, no. 12, pp. 2800-11, Jun 15 1998, doi: 10.1172/JCI2389.
- [76] L. Oberst *et al.*, "Dominant-negative effect of a mutant cardiac troponin T on cardiac structure and function in transgenic mice," *J Clin Invest*, vol. 102, no. 8, pp. 1498-505, Oct 15 1998, doi: 10.1172/JCI4088.

- [77] M. W. Costa *et al.*, "Functional characterization of a novel mutation in NKX2-5 associated with congenital heart disease and adult-onset cardiomyopathy," *Circ Cardiovasc Genet*, vol. 6, no. 3, pp. 238-47, Jun 2013, doi: 10.1161/CIRCGENETICS.113.000057.
- [78] M. B. Furtado *et al.*, "Point mutations in murine Nkx2-5 phenocopy human congenital heart disease and induce pathogenic Wnt signaling," *Jci Insight*, vol. 2, no. 6, p. e88271, Mar 23 2017, doi: 10.1172/jci.insight.88271.
- [79] J. Lee, J. M. Ellis, and M. J. Wolfgang, "Adipose Fatty Acid Oxidation Is Required for Thermogenesis and Potentiates Oxidative Stress-Induced Inflammation," (in English), *Cell Reports*, vol. 10, no. 2, pp. 266-279, Jan 13 2015, doi: 10.1016/j.celrep.2014.12.023.
- [80] A. S. Pereyra *et al.*, "Loss of cardiac carnitine palmitoyltransferase 2 results in rapamycin-resistant, acetylation-independent hypertrophy," *J Biol Chem*, 2017, doi: 10.1074/jbc.M117.800839.
- [81] Z. Xu, J. Alloush, E. Beck, and N. Weisleder, "A murine model of myocardial ischemia-reperfusion injury through ligation of the left anterior descending artery," *J Vis Exp*, no. 86, Apr 10 2014, doi: 10.3791/51329.
- [82] L. H. Michael *et al.*, "Myocardial ischemia and reperfusion: a murine model," *Am J Physiol*, vol. 269, no. 6 Pt 2, pp. H2147-54, Dec 1995. [Online]. Available: <https://www.ncbi.nlm.nih.gov/pubmed/8594926>.
- [83] S. C. Kim, O. Boehm, R. Meyer, A. Hoefft, P. Knufermann, and G. Baumgarten, "A murine closed-chest model of myocardial ischemia and reperfusion," *J Vis Exp*, no. 65, p. e3896, Jul 17 2012, doi: 10.3791/3896.
- [84] R. D. Patten *et al.*, "Ventricular remodeling in a mouse model of myocardial infarction," *Am J Physiol*, vol. 274, no. 5 Pt 2, pp. H1812-20, May 1998. [Online]. Available: <https://www.ncbi.nlm.nih.gov/pubmed/9612394>.
- [85] S. Kanno *et al.*, "Echocardiographic evaluation of ventricular remodeling in a mouse model of myocardial infarction," *J Am Soc Echocardiogr*, vol. 15, no. 6, pp. 601-9, Jun 2002. [Online]. Available: <https://www.ncbi.nlm.nih.gov/pubmed/12050601>.
- [86] S. Bialik *et al.*, "Myocyte apoptosis during acute myocardial infarction in the mouse localizes to hypoxic regions but occurs independently of p53," *J Clin Invest*, vol. 100, no. 6, pp. 1363-72, Sep 15 1997, doi: 10.1172/JCI119656.
- [87] X. M. Gao, Q. Xu, H. Kiriazis, A. M. Dart, and X. J. Du, "Mouse model of post-infarct ventricular rupture: time course, strain- and gender-dependency, tensile strength, and histopathology," *Cardiovasc Res*, vol. 65, no. 2, pp. 469-77, Feb 01 2005, doi: 10.1016/j.cardiores.2004.10.014.

- [88] X. M. Gao *et al.*, "Lower risk of postinfarct rupture in mouse heart overexpressing beta 2-adrenergic receptors: importance of collagen content," *J Cardiovasc Pharmacol*, vol. 40, no. 4, pp. 632-40, Oct 2002. [Online]. Available: <https://www.ncbi.nlm.nih.gov/pubmed/12352327>.
- [89] O. Dewald *et al.*, "A murine model of ischemic cardiomyopathy induced by repetitive ischemia and reperfusion," *Thorac Cardiovasc Surg*, vol. 52, no. 5, pp. 305-11, Oct 2004, doi: 10.1055/s-2004-821153.
- [90] O. Dewald *et al.*, "Development of murine ischemic cardiomyopathy is associated with a transient inflammatory reaction and depends on reactive oxygen species," *Proc Natl Acad Sci U S A*, vol. 100, no. 5, pp. 2700-5, Mar 04 2003, doi: 10.1073/pnas.0438035100.
- [91] Y. Guo, W. J. Wu, Y. Qiu, X. L. Tang, Z. Yang, and R. Bolli, "Demonstration of an early and a late phase of ischemic preconditioning in mice," *Am J Physiol*, vol. 275, no. 4 Pt 2, pp. H1375-87, Oct 1998. [Online]. Available: <https://www.ncbi.nlm.nih.gov/pubmed/9746488>.
- [92] W. E. Stansfield, N. C. Moss, M. S. Willis, R. Tang, and C. H. Selzman, "Proteasome inhibition attenuates infarct size and preserves cardiac function in a murine model of myocardial ischemia-reperfusion injury," *Ann Thorac Surg*, vol. 84, no. 1, pp. 120-5, Jul 2007, doi: 10.1016/j.athoracsur.2007.02.049.
- [93] M. Yada *et al.*, "FR167653 diminishes infarct size in a murine model of myocardial ischemia-reperfusion injury," *J Thorac Cardiovasc Surg*, vol. 128, no. 4, pp. 588-94, Oct 2004, doi: 10.1016/j.jtcvs.2004.02.007.
- [94] G. X. Zhang *et al.*, "Role of AT1 receptor in isoproterenol-induced cardiac hypertrophy and oxidative stress in mice," *J Mol Cell Cardiol*, vol. 42, no. 4, pp. 804-11, Apr 2007, doi: 10.1016/j.yjmcc.2007.01.012.
- [95] L. Liu *et al.*, "miR-208a as a biomarker of isoproterenol-induced cardiac injury in Sod2<sup>+/-</sup> and C57BL/6J wild-type mice," *Toxicol Pathol*, vol. 42, no. 7, pp. 1117-29, Oct 2014, doi: 10.1177/0192623314525684.
- [96] W. Zhu, W. Shou, R. M. Payne, R. Caldwell, and L. J. Field, "A mouse model for juvenile doxorubicin-induced cardiac dysfunction," *Pediatr Res*, vol. 64, no. 5, pp. 488-94, Nov 2008, doi: 10.1203/PDR.0b013e318184d732.
- [97] Y. Shizukuda, S. Matoba, O. Y. Mian, T. Nguyen, and P. M. Hwang, "Targeted disruption of p53 attenuates doxorubicin-induced cardiac toxicity in mice," *Mol Cell Biochem*, vol. 273, no. 1-2, pp. 25-32, May 2005. [Online]. Available: <https://www.ncbi.nlm.nih.gov/pubmed/16013437>.

- [98] H. Nakaoka *et al.*, "Establishment of a novel murine model of ischemic cardiomyopathy with multiple diffuse coronary lesions," *PLoS One*, vol. 8, no. 8, p. e70755, 2013, doi: 10.1371/journal.pone.0070755.
- [99] A. Braun *et al.*, "Loss of SR-BI expression leads to the early onset of occlusive atherosclerotic coronary artery disease, spontaneous myocardial infarctions, severe cardiac dysfunction, and premature death in apolipoprotein E-deficient mice," *Circ Res*, vol. 90, no. 3, pp. 270-6, Feb 22 2002. [Online]. Available: <https://www.ncbi.nlm.nih.gov/pubmed/11861414>.
- [100] S. Zhang *et al.*, "Diet-induced occlusive coronary atherosclerosis, myocardial infarction, cardiac dysfunction, and premature death in scavenger receptor class B type I-deficient, hypomorphic apolipoprotein ER61 mice," *Circulation*, vol. 111, no. 25, pp. 3457-64, Jun 28 2005, doi: 10.1161/CIRCULATIONAHA.104.523563.
- [101] C. Mitchell *et al.*, "Guidelines for Performing a Comprehensive Transthoracic Echocardiographic Examination in Adults: Recommendations from the American Society of Echocardiography," *J Am Soc Echocardiogr*, vol. 32, no. 1, pp. 1-64, Jan 2019, doi: 10.1016/j.echo.2018.06.004.
- [102] C. T. Badea, B. Fubara, L. W. Hedlund, and G. A. Johnson, "4-D micro-CT of the mouse heart," *Mol Imaging*, vol. 4, no. 2, pp. 110-6, Apr-Jun 2005. [Online]. Available: <https://www.ncbi.nlm.nih.gov/pubmed/16105509>.
- [103] P. J. Dunmore-Buyze *et al.*, "Three-dimensional imaging of the mouse heart and vasculature using micro-CT and whole-body perfusion of iodine or phosphotungstic acid," *Contrast Media Mol Imaging*, vol. 9, no. 5, pp. 383-90, Sep-Oct 2014, doi: 10.1002/cmmi.1588.
- [104] S. Schroeder *et al.*, "Cardiac computed tomography: indications, applications, limitations, and training requirements: report of a Writing Group deployed by the Working Group Nuclear Cardiology and Cardiac CT of the European Society of Cardiology and the European Council of Nuclear Cardiology," *Eur Heart J*, vol. 29, no. 4, pp. 531-56, Feb 2008, doi: 10.1093/eurheartj/ehm544.
- [105] M. C. Ku, T. Huelnhagen, T. Niendorf, and A. Pohlmann, "Cardiac MRI in Small Animals," *Methods Mol Biol*, vol. 1718, pp. 269-284, 2018, doi: 10.1007/978-1-4939-7531-0\_16.
- [106] E. Heijman *et al.*, "Comparison between prospective and retrospective triggering for mouse cardiac MRI," *NMR in Biomedicine*, vol. 20, no. 4, pp. 439-447, 2007, doi: <https://doi.org/10.1002/nbm.1110>.
- [107] L. Vanhoutte *et al.*, "MRI Assessment of Cardiomyopathy Induced by beta 1-Adrenoreceptor Autoantibodies and Protection Through beta 3-Adrenoreceptor Overexpression," (in English), *Sci Rep-Uk*, vol. 7, Mar 9 2017, doi: 10.1038/srep43951.

- [108] I. E. Verhaart *et al.*, "Assessment of cardiac function in three mouse dystrophinopathies by magnetic resonance imaging," *Neuromuscul Disord*, vol. 22, no. 5, pp. 418-26, May 2012, doi: 10.1016/j.nmd.2011.10.025.
- [109] J. E. Schneider *et al.*, "Fast, high-resolution in vivo cine magnetic resonance imaging in normal and failing mouse hearts on a vertical 11.7 T system," (in English), *Journal of Magnetic Resonance Imaging*, vol. 18, no. 6, pp. 691-701, Dec 2003, doi: 10.1002/jmri.10411.
- [110] M. Nahrendorf, K. H. Hiller, K. Hu, G. Ertl, A. Haase, and W. R. Bauer, "Cardiac magnetic resonance imaging in small animal models of human heart failure," (in English), *Med Image Anal*, vol. 7, no. 3, pp. 369-375, Sep 2003, doi: 10.1016/S1361-8415(03)00011-2.
- [111] F. Wiesmann *et al.*, "Analysis of right ventricular function in healthy mice and a murine model of heart failure by in vivo MRI," *Am J Physiol Heart Circ Physiol*, vol. 283, no. 3, pp. H1065-71, Sep 2002, doi: 10.1152/ajpheart.00802.2001.
- [112] F. Wiesmann *et al.*, "Dobutamine-stress magnetic resonance microimaging in mice - Acute changes of cardiac geometry and function in normal and failing murine hearts," (in English), *Circulation Research*, vol. 88, no. 6, pp. 563-569, Mar 30 2001. [Online]. Available: <Go to ISI>://WOS:000167821400006.
- [113] S. M. Bovens *et al.*, "Evaluation of infarcted murine heart function: comparison of prospectively triggered with self-gated MRI," (in English), *Nmr in Biomedicine*, vol. 24, no. 3, pp. 307-315, Apr 2011, doi: 10.1002/nbm.1593.
- [114] S. P. Williams *et al.*, "Dobutamine stress cine-MRI of cardiac function in the hearts of adult cardiomyocyte-specific VEGF knockout mice," *J Magn Reson Imaging*, vol. 14, no. 4, pp. 374-82, Oct 2001. [Online]. Available: <https://www.ncbi.nlm.nih.gov/pubmed/11599061>.
- [115] T. J. Mosher and M. B. Smith, "A DANTE tagging sequence for the evaluation of translational sample motion," *Magn Reson Med*, vol. 15, no. 2, pp. 334-9, Aug 1990. [Online]. Available: <https://www.ncbi.nlm.nih.gov/pubmed/2392056>.
- [116] L. Axel and L. Dougherty, "MR imaging of motion with spatial modulation of magnetization," *Radiology*, vol. 171, no. 3, pp. 841-5, Jun 1989, doi: 10.1148/radiology.171.3.2717762.
- [117] H. Li *et al.*, "Quantification of Biventricular Myocardial Strain Using CMR Feature Tracking: Reproducibility in Small Animals," *Biomed Res Int*, vol. 2021, p. 8492705, 2021, doi: 10.1155/2021/8492705.
- [118] Y. L. Wu, "Cardiac MRI Assessment of Mouse Myocardial Infarction and Regeneration," *Methods Mol Biol*, vol. 2158, pp. 81-106, 2021, doi: 10.1007/978-1-0716-0668-1\_8.

- [119] J. H. Hankiewicz and E. D. Lewandowski, "Improved cardiac tagging resolution at ultra-high magnetic field elucidates transmural differences in principal strain in the mouse heart and reduced stretch in dilated cardiomyopathy," (in English), *J Cardiovasc Magn R*, vol. 9, no. 6, pp. 883-890, 2007, doi: 10.1080/10976640701693683.
- [120] J. S. Chuang, A. Zemljic-Harpf, R. S. Ross, L. R. Frank, A. D. McCulloch, and J. H. Omens, "Determination of three-dimensional ventricular strain distributions in gene-targeted mice using tagged MRI," *Magn Reson Med*, vol. 64, no. 5, pp. 1281-8, Nov 2010, doi: 10.1002/mrm.22547.
- [121] J. H. Hankiewicz, P. H. Goldspink, P. M. Buttrick, and E. D. Lewandowski, "Principal strain changes precede ventricular wall thinning during transition to heart failure in a mouse model of dilated cardiomyopathy," (in English), *Am J Physiol-Heart C*, vol. 294, no. 1, pp. H330-H336, Jan 2008, doi: 10.1152/ajpheart.01109.2007.
- [122] K. Hammouda *et al.*, "A New Framework for Performing Cardiac Strain Analysis from Cine MRI Imaging in Mice," *Sci Rep*, vol. 10, no. 1, p. 7725, May 7 2020, doi: 10.1038/s41598-020-64206-x.
- [123] W. D. Gilson, Z. Q. Yang, B. A. French, and F. H. Epstein, "Complementary displacement-encoded MRI for contrast-enhanced infarct detection and quantification of myocardial function in mice," (in English), *Magn Reson Med*, vol. 51, no. 4, pp. 744-752, Apr 2004, doi: 10.1002/mrm.20003.
- [124] V. Herold, P. Morchel, C. Faber, E. Rommel, A. Haase, and P. M. Jakob, "In vivo quantitative three-dimensional motion mapping of the murine myocardium with PC-MRI at 17.6 T," (in English), *Magn Reson Med*, vol. 55, no. 5, pp. 1058-1064, May 2006, doi: 10.1002/mrm.20866.
- [125] A. H. Aletras, S. Ding, R. S. Balaban, and H. Wen, "DENSE: displacement encoding with stimulated echoes in cardiac functional MRI," *J Magn Reson*, vol. 137, no. 1, pp. 247-52, Mar 1999, doi: 10.1006/jmre.1998.1676.
- [126] S. Azam *et al.*, "Comparison of Velocity Vector Imaging Echocardiography With Magnetic Resonance Imaging in Mouse Models of Cardiomyopathy," (in English), *Circ-Cardiovasc Imag*, vol. 5, no. 6, pp. 776-781, Nov 2012, doi: 10.1161/Circimaging.111.972406.
- [127] N. K. Naresh *et al.*, "Cardiac MRI Myocardial Functional and Tissue Characterization Detects Early Cardiac Dysfunction in a Mouse Model of Chemotherapy-Induced Cardiotoxicity," *NMR Biomed*, vol. 33, no. 9, p. e4327, Sep 2020, doi: 10.1002/nbm.4327.
- [128] W. D. Gilson, Z. Q. Yang, B. A. French, and F. H. Epstein, "Measurement of myocardial mechanics in mice before and after infarction using multislice displacement-encoded MRI with 3D motion encoding," (in English), *Am J Physiol-Heart C*, vol. 288, no. 3, pp. H1491-H1497, Mar 2005, doi: 10.1152/ajpheart.00632.2004.

- [129] Z. Q. Liu, X. Zhang, and J. F. Wenk, "Quantification of regional right ventricular strain in healthy rats using 3D spiral cine dense MRI," *J Biomech*, vol. 94, pp. 219-223, Sep 20 2019, doi: 10.1016/j.jbiomech.2019.07.026.
- [130] J. Zhong and X. Yu, "Strain and Torsion Quantification in Mouse Hearts Under Dobutamine Stimulation Using 2D Multiphase MR DENSE," (in English), *Magn Reson Med*, vol. 64, no. 5, pp. 1315-1322, Nov 2010, doi: 10.1002/mrm.22530.
- [131] E. Dall'Armellina, B. A. Jung, C. A. Lygate, S. Neubauer, M. Markl, and J. E. Schneider, "Improved method for quantification of regional cardiac function in mice using phase-contrast MRI," (in English), *Magn Reson Med*, vol. 67, no. 2, pp. 541-551, Feb 2012, doi: 10.1002/mrm.23022.
- [132] B. Jung *et al.*, "A quantitative comparison of regional myocardial motion in mice, rabbits and humans using in-vivo phase contrast CMR," (in English), *J Cardiovasc Magn R*, vol. 14, Dec 27 2012, doi: 10.1186/1532-429x-14-87.
- [133] J. U. G. Streif *et al.*, "In vivo time-resolved quantitative motion mapping of the murine myocardium with phase contrast MRI," (in English), *Magn Reson Med*, vol. 49, no. 2, pp. 315-321, Feb 2003, doi: 10.1002/mrm.10342.
- [134] G. McGinley *et al.*, "Accelerated magnetic resonance imaging tissue phase mapping of the rat myocardium using compressed sensing with iterative soft-thresholding," *PLoS One*, vol. 14, no. 7, p. e0218874, 2019, doi: 10.1371/journal.pone.0218874.
- [135] M. Kramer *et al.*, "Cardiac 4D phase-contrast CMR at 9.4 T using self-gated ultra-short echo time (UTE) imaging," (in English), *J Cardiovasc Magn R*, vol. 19, Mar 31 2017, doi: 10.1186/s12968-017-0351-9.
- [136] G. S. Sangha, E. H. Phillips, and C. J. Goergen, "In vivo photoacoustic lipid imaging in mice using the second near-infrared window," *Biomed Opt Express*, vol. 8, no. 2, pp. 736-742, Feb 01 2017, doi: 10.1364/BOE.8.000736.
- [137] J. J. Boyle *et al.*, "Regularization-Free Strain Mapping in Three Dimensions, With Application to Cardiac Ultrasound," *J Biomech Eng*, vol. 141, no. 1, Jan 1 2019, doi: 10.1115/1.4041576.
- [138] E. D. Folland, A. F. Parisi, P. F. Moynihan, D. R. Jones, C. L. Feldman, and D. E. Tow, "Assessment of left ventricular ejection fraction and volumes by real-time, two-dimensional echocardiography. A comparison of cineangiographic and radionuclide techniques," *Circulation*, vol. 60, no. 4, pp. 760-6, Oct 1979. [Online]. Available: <https://www.ncbi.nlm.nih.gov/pubmed/476879>.

- [139] F. W. Damen, A. R. Adelsperger, K. E. Wilson, and C. J. Goergen, "Comparison of Traditional and Integrated Digital Anesthetic Vaporizers," *J Am Assoc Lab Anim Sci*, vol. 54, no. 6, pp. 756-62, Nov 2015. [Online]. Available: <https://www.ncbi.nlm.nih.gov/pubmed/26632785/>
- [140] K. C. Vinnakota and J. B. Bassingthwaight, "Myocardial density and composition: a basis for calculating intracellular metabolite concentrations," *Am J Physiol Heart Circ Physiol*, vol. 286, no. 5, pp. H1742-9, May 2004, doi: 10.1152/ajpheart.00478.2003.
- [141] S. Gao, D. Ho, D. E. Vatner, and S. F. Vatner, "Echocardiography in Mice," *Curr Protoc Mouse Biol*, vol. 1, pp. 71-83, Mar 01 2011, doi: 10.1002/9780470942390.mo100130.
- [142] L. E. Teichholz, T. Kreulen, M. V. Herman, and R. Gorlin, "Problems in echocardiographic volume determinations: echocardiographic-angiographic correlations in the presence of absence of asynergy," *Am J Cardiol*, vol. 37, no. 1, pp. 7-11, Jan 1976. [Online]. Available: <https://www.ncbi.nlm.nih.gov/pubmed/1244736>.
- [143] G. Murdolo *et al.*, "Left ventricular hypertrophy and obesity: only a matter of fat?," *High Blood Press Cardiovasc Prev*, vol. 22, no. 1, pp. 29-41, Mar 2015, doi: 10.1007/s40292-014-0068-x.
- [144] E. Levelt *et al.*, "Relationship Between Left Ventricular Structural and Metabolic Remodeling in Type 2 Diabetes," *Diabetes*, vol. 65, no. 1, pp. 44-52, Jan 2016, doi: 10.2337/db15-0627.
- [145] S. M. Houten, S. Violante, F. V. Ventura, and R. J. Wanders, "The Biochemistry and Physiology of Mitochondrial Fatty Acid beta-Oxidation and Its Genetic Disorders," *Annu Rev Physiol*, vol. 78, pp. 23-44, 2016, doi: 10.1146/annurev-physiol-021115-105045.
- [146] J. M. Ellis *et al.*, "Mouse cardiac acyl coenzyme a synthetase 1 deficiency impairs Fatty Acid oxidation and induces cardiac hypertrophy," *Mol Cell Biol*, vol. 31, no. 6, pp. 1252-62, Mar 2011, doi: 10.1128/MCB.01085-10.
- [147] K. R. Haynie, B. Vandanmagsar, S. E. Wicks, J. Zhang, and R. L. Mynatt, "Inhibition of carnitine palmitoyltransferase1b induces cardiac hypertrophy and mortality in mice," *Diabetes Obes Metab*, vol. 16, no. 8, pp. 757-60, Aug 2014, doi: 10.1111/dom.12248.
- [148] K. B. Cox, J. Liu, L. Tian, S. Barnes, Q. Yang, and P. A. Wood, "Cardiac hypertrophy in mice with long-chain acyl-CoA dehydrogenase or very long-chain acyl-CoA dehydrogenase deficiency," *Lab Invest*, vol. 89, no. 12, pp. 1348-54, Dec 2009, doi: 10.1038/labinvest.2009.86.
- [149] S. J. G. Knottnerus *et al.*, "Subclinical effects of long-chain fatty acid beta-oxidation deficiency on the adult heart: A case-control magnetic resonance study," *J Inherit Metab Dis*, vol. 43, no. 5, pp. 969-980, Sep 2020, doi: 10.1002/jimd.12266.

- [150] M. L. Lindsey, Z. Kassiri, J. A. I. Virag, L. E. de Castro Bras, and M. Scherrer-Crosbie, "Guidelines for measuring cardiac physiology in mice," *Am J Physiol Heart Circ Physiol*, vol. 314, no. 4, pp. H733-H752, Apr 1 2018, doi: 10.1152/ajpheart.00339.2017.
- [151] T. M. Stokke *et al.*, "Geometry as a Confounder When Assessing Ventricular Systolic Function: Comparison Between Ejection Fraction and Strain," *J Am Coll Cardiol*, vol. 70, no. 8, pp. 942-954, Aug 22 2017, doi: 10.1016/j.jacc.2017.06.046.
- [152] A. H. Soepriatna, A. K. Yeh, A. D. Clifford, S. E. Bezci, G. D. O'Connell, and C. J. Goergen, "Three-dimensional myocardial strain correlates with murine left ventricular remodelling severity post-infarction," *J R Soc Interface*, vol. 16, no. 160, p. 20190570, Nov 29 2019, doi: 10.1098/rsif.2019.0570.
- [153] D. Muraru, A. Niero, H. Rodriguez-Zanella, D. Cherata, and L. Badano, "Three-dimensional speckle-tracking echocardiography: benefits and limitations of integrating myocardial mechanics with three-dimensional imaging," *Cardiovasc Diagn Ther*, vol. 8, no. 1, pp. 101-117, Feb 2018, doi: 10.21037/cdt.2017.06.01.
- [154] M. C. Abduch, A. M. Alencar, W. Mathias, Jr., and M. L. Vieira, "Cardiac mechanics evaluated by speckle tracking echocardiography," *Arq Bras Cardiol*, vol. 102, no. 4, pp. 403-12, Apr 2014. [Online]. Available: <https://www.ncbi.nlm.nih.gov/pubmed/24844877>.
- [155] T. M. Morrison, G. Choi, C. K. Zarins, and C. A. Taylor, "Circumferential and longitudinal cyclic strain of the human thoracic aorta: age-related changes," *J Vasc Surg*, vol. 49, no. 4, pp. 1029-36, Apr 2009, doi: 10.1016/j.jvs.2008.11.056.
- [156] C. M. Moran and A. J. W. Thomson, "Preclinical Ultrasound Imaging—A Review of Techniques and Imaging Applications," (in English), *Frontiers in Physics*, Review vol. 8, no. 124, 2020-May-05 2020, doi: 10.3389/fphy.2020.00124.
- [157] C. Rutledge *et al.*, "Commercial 4-dimensional echocardiography for murine heart volumetric evaluation after myocardial infarction," *Cardiovasc Ultrasound*, vol. 18, no. 1, p. 9, Mar 12 2020, doi: 10.1186/s12947-020-00191-5.
- [158] J. Grune *et al.*, "Evaluation of a commercial multi-dimensional echocardiography technique for ventricular volumetry in small animals," *Cardiovasc Ultrasound*, vol. 16, no. 1, p. 10, Jul 3 2018, doi: 10.1186/s12947-018-0128-9.
- [159] M. Obokata, Y. N. V. Reddy, and B. A. Borlaug, "Diastolic Dysfunction and Heart Failure With Preserved Ejection Fraction: Understanding Mechanisms by Using Noninvasive Methods," *JACC Cardiovasc Imaging*, vol. 13, no. 1 Pt 2, pp. 245-257, Jan 2020, doi: 10.1016/j.jcmg.2018.12.034.
- [160] J. B. Hiebert, J. Vacek, Z. Shah, F. Rahman, and J. D. Pierce, "Use of speckle tracking to assess heart failure with preserved ejection fraction," *J Cardiol*, vol. 74, no. 5, pp. 397-402, Nov 2019, doi: 10.1016/j.jjcc.2019.06.004.

- [161] J. J. Hsu, B. Ziaieian, and G. C. Fonarow, "Heart Failure With Mid-Range (Borderline) Ejection Fraction: Clinical Implications and Future Directions," *JACC Heart Fail*, vol. 5, no. 11, pp. 763-771, Nov 2017, doi: 10.1016/j.jchf.2017.06.013.
- [162] C. L. Lekavich, D. J. Barksdale, V. Neelon, and J. R. Wu, "Heart failure preserved ejection fraction (HFpEF): an integrated and strategic review," *Heart Fail Rev*, vol. 20, no. 6, pp. 643-53, Nov 2015, doi: 10.1007/s10741-015-9506-7.
- [163] M. S. Amzulescu *et al.*, "Myocardial strain imaging: review of general principles, validation, and sources of discrepancies," *Eur Heart J Cardiovasc Imaging*, vol. 20, no. 6, pp. 605-619, Jun 1 2019, doi: 10.1093/ehjci/jez041.
- [164] W. M. Torres *et al.*, "Regional and temporal changes in left ventricular strain and stiffness in a porcine model of myocardial infarction," *Am J Physiol Heart Circ Physiol*, vol. 315, no. 4, pp. H958-H967, Oct 1 2018, doi: 10.1152/ajpheart.00279.2018.
- [165] M. B. Furtado *et al.*, "A novel conditional mouse model for Nkx2-5 reveals transcriptional regulation of cardiac ion channels," *Differentiation*, vol. 91, no. 1-3, pp. 29-41, Jan-Mar 2016, doi: 10.1016/j.diff.2015.12.003.
- [166] J. C. Wilmanns *et al.*, "Metformin intervention prevents cardiac dysfunction in a murine model of adult congenital heart disease," *Mol Metab*, Nov 15 2018, doi: 10.1016/j.molmet.2018.11.002.
- [167] C. Chen *et al.*, "Deep Learning for Cardiac Image Segmentation: A Review," *Front Cardiovasc Med*, vol. 7, p. 25, 2020, doi: 10.3389/fcvm.2020.00025.
- [168] S. Leclerc *et al.*, "Deep Learning for Segmentation Using an Open Large-Scale Dataset in 2D Echocardiography," *Ieee T Med Imaging*, vol. 38, no. 9, pp. 2198-2210, 2019, doi: 10.1109/TMI.2019.2900516.
- [169] S. Liu *et al.*, "Deep Learning in Medical Ultrasound Analysis: A Review," *Engineering*, vol. 5, no. 2, pp. 261-275, 2019, doi: 10.1016/j.eng.2018.11.020.
- [170] Z. Wang, Z. Zhang, J. Zheng, B. Huang, I. Voiculescu, and G.-Z. Yang, "Deep Learning in Medical Ultrasound Image Segmentation: a Review."
- [171] L. J. Brattain, B. A. Telfer, M. Dhyani, J. R. Grajo, and A. E. Samir, "Machine learning for medical ultrasound: status, methods, and future opportunities," *Abdom Radiol (NY)*, vol. 43, no. 4, pp. 786-799, Apr 2018, doi: 10.1007/s00261-018-1517-0.
- [172] Z. Akkus *et al.*, "A Survey of Deep-Learning Applications in Ultrasound: Artificial Intelligence-Powered Ultrasound for Improving Clinical Workflow," *J Am Coll Radiol*, vol. 16, no. 9 Pt B, pp. 1318-1328, Sep 2019, doi: 10.1016/j.jacr.2019.06.004.

- [173] D. JD, G. R, S. M, J. R, W. MB, and F. B, "Ultrasound Segmentation of Rat Hearts Using Convolution Neural Networks," *Proc SPIE Int Soc Opt Eng*, vol. 10580, no. 105801A, 2018, doi: 10.1117/12.2293558.
- [174] D. Dey *et al.*, "Artificial Intelligence in Cardiovascular Imaging: JACC State-of-the-Art Review," *J Am Coll Cardiol*, vol. 73, no. 11, pp. 1317-1335, Mar 26 2019, doi: 10.1016/j.jacc.2018.12.054.
- [175] Y. Wang *et al.*, "Fully automatic segmentation of 4D MRI for cardiac functional measurements," *Med Phys*, vol. 46, no. 1, pp. 180-189, Jan 2019, doi: 10.1002/mp.13245.
- [176] H. Berhane *et al.*, "Fully automated 3D aortic segmentation of 4D flow MRI for hemodynamic analysis using deep learning," *Magn Reson Med*, vol. 84, no. 4, pp. 2204-2218, Oct 2020, doi: 10.1002/mrm.28257.
- [177] P. V. Tran, "A Fully Convolutional Neural Network for Cardiac Segmentation in Short-Axis MRI," p. arXiv:1604.00494. [Online]. Available: <https://ui.adsabs.harvard.edu/abs/2016arXiv160400494T>
- [178] F. Commandeur *et al.*, "Fully Automated CT Quantification of Epicardial Adipose Tissue by Deep Learning: A Multicenter Study," *Radiol Artif Intell*, vol. 1, no. 6, p. e190045, Nov 27 2019, doi: 10.1148/ryai.2019190045.
- [179] C. Militello *et al.*, "A semi-automatic approach for epicardial adipose tissue segmentation and quantification on cardiac CT scans," *Comput Biol Med*, vol. 114, p. 103424, Nov 2019, doi: 10.1016/j.combiomed.2019.103424.
- [180] G. Wang *et al.*, "Speckle tracking echocardiography assessment of global and regional contraction dysfunction in the mice model of pressure overload," *J Huazhong Univ Sci Technolog Med Sci*, vol. 35, no. 2, pp. 271-277, Apr 2015, doi: 10.1007/s11596-015-1423-4.
- [181] D. S. Moore, G. P. McCabe, and B. A. Craig, *Introduction to the practice of statistics*, 7th ed. New York: W.H. Freeman & Co, 2012, p. 1 v (various pagings).
- [182] J. Zhu, F. Shi, T. You, C. Tang, and J. Chen, "Global diastolic strain rate for the assessment of left ventricular diastolic dysfunction in young peritoneal dialysis patients: a case control study," *BMC Nephrol*, vol. 21, no. 1, p. 89, Mar 10 2020, doi: 10.1186/s12882-020-01742-8.
- [183] I. J. Goodfellow *et al.*, "Generative Adversarial Networks," p. arXiv:1406.2661. [Online]. Available: <https://ui.adsabs.harvard.edu/abs/2014arXiv1406.2661G>

- [184] Q. Zhang, H. Wang, H. Lu, D. Won, and S. W. Yoon, "Medical Image Synthesis with Generative Adversarial Networks for Tissue Recognition," in *2018 IEEE International Conference on Healthcare Informatics (ICHI)*, 4-7 June 2018 2018, pp. 199-207, doi: 10.1109/ICHI.2018.00030. [Online]. Available: <https://ieeexplore.ieee.org/document/8419363/>
- [185] N. K. Singh and K. Raza, "Medical Image Generation using Generative Adversarial Networks," p. arXiv:2005.10687. [Online]. Available: <https://ui.adsabs.harvard.edu/abs/2020arXiv200510687S>
- [186] C. Han *et al.*, "Infinite Brain MR Images: PGGAN-Based Data Augmentation for Tumor Detection," in *Neural Approaches to Dynamics of Signal Exchanges*, A. Esposito, M. Faundez-Zanuy, F. C. Morabito, and E. Pasero Eds. Singapore: Springer Singapore, 2020, pp. 291-303.
- [187] X. Yi, E. Walia, and P. Babyn, "Generative adversarial network in medical imaging: A review," *Med Image Anal*, vol. 58, p. 101552, Dec 2019, doi: 10.1016/j.media.2019.101552.
- [188] J. Xu, M. Li, and Z. Zhu, "Automatic Data Augmentation for 3D Medical Image Segmentation," Cham, 2020: Springer International Publishing, in *Medical Image Computing and Computer Assisted Intervention – MICCAI 2020*, pp. 378-387.
- [189] S. Chen, K. Ma, and Y. Zheng, "Med3D: Transfer Learning for 3D Medical Image Analysis," p. arXiv:1904.00625. [Online]. Available: <https://ui.adsabs.harvard.edu/abs/2019arXiv190400625C>
- [190] K. Kaku *et al.*, "Age-related normal range of left ventricular strain and torsion using three-dimensional speckle-tracking echocardiography," *J Am Soc Echocardiogr*, vol. 27, no. 1, pp. 55-64, Jan 2014, doi: 10.1016/j.echo.2013.10.002.
- [191] H. Awadalla, M. A. Saleh, M. Abdel Kader, and A. Mansour, "Left ventricular torsion assessed by two-dimensional echocardiography speckle tracking as a predictor of left ventricular remodeling and short-term outcome following primary percutaneous coronary intervention for acute myocardial infarction: A single-center experience," *Echocardiography*, Jul 28 2017, doi: 10.1111/echo.13611.

## PUBLICATIONS

The following list provides a comprehensive view of all published manuscripts and their scientific Impact as quantified by the number of citations:

1. **Frederick W. Damen**, David T. Newton, Guang Lin, and Craig J. Goergen. (2021) Machine Learning Driven Contouring of High-Frequency Four-Dimensional Cardiac Ultrasound Data. Applied Sciences. DOI: 10.3390/app11041690 (*Original Contribution*) – [Citations: 0](#)
2. Frederick C. Damen, Alessandro Scotti, **Frederick W. Damen**, Nitu Saran, Tibor Valyi-Nagy, Mirko Vukelicha, and Kejia Cai. (2020) Multimodal Apparent Diffusion (MAD) Weighted Magnetic Resonance Imaging. Magnetic Resonance Imaging. DOI: 10.1016/j.mri.2020.12.007. (*Original Contribution*) – [Citations: 0](#)
3. Kyoungrae Kim, Bohyun Ro, **Frederick W. Damen**, Daniel P. Gramling, Trevor D. Lehr, Qifan Song, Craig J. Goergen, and Bruno T. Roseguini. (2020) Heat therapy improves body composition and muscle function, but does not affect capillary or collateral growth in a model of obesity and hindlimb ischemia. Journal of Applied Physiology. DOI: 10.1152/jappphysiol.00535.2020. (*Original Contribution*) – [Citations: 0](#)
4. John J. Boyle, Arvin H. Soepriatna, **Frederick W. Damen**, Roger A. Rowe, Robert B. Pless, Attila Kovacs, Craig J. Goergen, Stavros Thomopoulos, and Guy M. Genin. (2019). Regularization-Free Strain Mapping in Three Dimensions, With Application to Cardiac Ultrasound. Journal of Biomechanical Engineering, **141**(1). DOI: 10.1115/1.4041576. (*Original Contribution*) – [Citations: 5](#)
5. Andrea Acuna, Alycia G. Berman, **Frederick W. Damen**, et al. (2018). Computational Fluid Dynamics of Vascular Disease in Animal Models. Journal of Biomechanical Engineering. **140**(8). DOI: 10.1115/1.4039678. (*Review Article*) – [Citations: 1](#)
6. Arvin H. Soepriatna\*, **Frederick W. Damen\***, Pavlos P. Vlachos, Craig J. Goergen. (2017). Cardiac and Respiratory-Gated Volumetric Murine Ultrasound. International Journal of Cardiovascular Imaging. **34**(5):713-724. DOI: 10.1007/s10554-017-1283-z. \*Equal contribution. (*Original Contribution*) – [Citations: 6](#)

7. **Frederick W. Damen**, Alycia G. Berman, Arvin H. Soepriatna, Jessica M. Ellis, Stephen Buttars, Kristiina Aasa, Craig J. Goergen. (2017). High Frequency Four-Dimensional Ultrasound (4DUS): A Reliable Method for Assessing Murine Cardiac Function. Tomography. **3**(4):180-187. DOI: 10.18383/j.tom.2017.00016. (*Original Contribution*) – [Citations: 6](#)
8. Andrea S. Pereyra, Like Y. Hasek, Kate L. Harris, Alycia G. Berman, **Frederick W. Damen**, Craig J. Goergen, Jessica M. Ellis. (2017). Loss of Cardiac Carnitine Palmitoyltransferase 2 Results in Rapamycin-Resistant, Acetylation-Independent Hypertrophy. Journal of Biological Chemistry. DOI: 10.1074/jbc.M117.800839. (*Original Contribution*) – [Citations: 14](#)
9. Soham Ghosh, James G. Cimino, Adrienne K. Scott, **Frederick W. Damen**, Evan H. Phillips, Alexander I. Veress, Corey P. Neu, Craig J. Goergen. (2017). In Vivo Multiscale and Spatially-Dependent Biomechanics Reveals Differential Strain Transfer Hierarchy in Skeletal Muscle. ACS Biomaterials Science & Engineering. DOI: 10.1021/acsbiomaterials.6b00772. (*Original Contribution*) – [Citations: 5](#)
10. **Frederick W. Damen**, Amelia R. Adelsperger, Katherine E. Wilson, Craig J. Goergen. (2015). Comparison of Traditional and Integrated Digital Anesthetic Vaporizers. American Association for Laboratory Animal Science. **54**(6): 756-762. (*Original Contribution*) – [Citations: 11](#)
11. Yi Sui, He Wang, Guanzhong Liu, **Frederick W. Damen**, Christian Wanamaker, Yuhua Li, Xiaohong Joe Zhou. (2015). Differentiation of Low- and High-Grade Pediatric Brain Tumors with High b-Value Diffusion-weighted MR Imaging and a Fractional Order Calculus Model. Radiology. **277**(2): 489-496. (*Original Contribution*) – [Citations: 41](#)
12. Longchuan Li, Xiaoping Hu, Todd M. Preuss, Matthew F. Glasser, **Frederick W. Damen**, Yuxuan Qiu, James K. Rilling. (2013). Mapping putative hubs in human, chimpanzee and rhesus macaque connectomes via diffusion tractography. Neuroimage. **80**: 462-474. (*Original Contribution*) – [Citations: 70](#)
13. Longchuan Li, James K. Rilling, Todd M. Preuss, Matthew F. Glasser, **Frederick W. Damen**, Xiaoping Hu. (2012). Quantitative assessment of a framework for creating anatomical brain networks via global tractography. Neuroimage. **61**(4): 1017-1030. (*Original Contribution*) – [Citations: 28](#)